Doctoral Dissertation

Prediction of Vertical Bending Moment Using Measured and Computed Wave-Induced Pressure Distribution on Ship Hull

Kurniawan Teguh Waskito

June 2020

Dept. of Naval Architecture & Ocean Engineering
Division of Global Architecture
Graduate School of Engineering
Osaka University

“In the creation of the heavens and earth; in the alteration of day and night; in the ships that sail the seas with goods for people: in the water which God sends down from the sky to give life to the Earth when it has been barren; scattering all kinds of creatures over it; in the changing of the winds and clouds that run their appointed courses between the sky and Earth; there are signs in all these for those who use their minds.”

QS 2:164

Abstract

Precise prediction of wave loads on ships and floating structures is paramount in the structural design stage. The use of a segmented ship model is a common method to quantify the wave loads. Nonetheless, the value could be measured only at few segmented sections. To obtain the wave loads at any longitudinal position and to clarify nonlinear features in the wave loads more precisely, local quantities of the pressure on the whole ship-hull surface need to be measured along with ship motions in waves.

In the present study, a novel experiment using a bulk carrier model has been carried out to measure the spatial distribution of wave-induced unsteady pressure by means of a large number of Fiber Bragg Gratings (FBG) pressure sensors affixed on the whole ship-hull surface, and at the same time, the wave-induced ship motions and ship-side wave profile have been measured. A straightforward case for a ship with zero forward speed is firstly elucidated to present the linear responses. Afterward, to see hydrodynamic characteristics in nonlinear and forward-speed effects on measured and analyzed results, some computations with the linear frequency-domain Rankine Panel Method (RPM) and the nonlinear Computational Fluid Dynamics (CFD) method solving the Reynolds-Averaged Navier-Stokes (RANS) equations are made. A parametric study is made and favorable agreement is attained for the pressure distribution and resulting vertical bending moment between the results of the experiment and corresponding numerical computations. Validation of the measured pressure distribution has also been made through a comparison with the wave-exciting force and moment between the two independent results obtained by integration of the measured pressure over the entire wetted surface of a ship and by direct measurement using a dynamometer. A very promising agreement is confirmed in this case as well. As another crucial validation for this proposed method, a comparative study is made with the benchmark test data of a 6750-TEU container ship used for the ITTC-ISSC joint workshop in 2014; which also demonstrates remarkable agreement.

Conclusively, the present study may provide a new research technique, particularly in the experiment and computation model for predicting the vertical bending moment distribution and for studying local hydrodynamic features in wave-related unsteady phenomena.

Keywords: Wave loads, Vertical bending moment, Nonlinearity, Pressure distribution, Fiber bragg grating, Rankine panel method, CFD

Acknowledgements

This Doctoral program is accomplished in the International Program of Maritime and Urban Engineering of Osaka University, which is fully supported by the Japan International Cooperation Agency (JICA) Innovative Asia program.

First and foremost, it is an honor to express my heartfelt gratitude to my supervisor, Professor Masashi Kashiwagi, whose expertise, perseverance, and vision made the completion of this dissertation possible in the end. I am indebted too much for his generosity and kindness during my study. His prodigious thought and continuous encouragement are inspiringly a lot to my study.

I would also like to give thanks to some faculty members in our laboratory, Professor Munehiko Minoura as Associate Professor and Professor Takahito Iida as Assistant professor, who kindly gave constructive advice during laboratory meetings. Also Ms. Tamae Miyabe as the laboratory secretary who helped in the administrative things.

I am also indebted to all parties involved in the experiment for measuring the spatial pressure distribution on the ship-hull surface. This research is in the collaborative work between Osaka University and Hiroshima University. I am grateful to Professor Hidetsugu Iwashita at Hiroshima University and several students from both universities have been participated over a couple of years in this experiment and contributed to accurate measurement and analysis of a huge amount of data. This experimental work was supported in part by the Collaborative Research Program of Research Institute for Applied Mechanics (RIAM), Kyushu University, and in fact the measurement was carried out in the towing tank of RIAM. The authors are thankful to this support and help provided by Prof. Changhong Hu of RIAM and his colleagues. The present work was also partially supported with JSPS Grant-in-Aid for Scientific Research (A), Grant Number 17H01357 at Osaka University and also Grant-in-Aid for Scientific Research (B), Grant Number 18H01639 at Hiroshima University.

Further, to Professor Munehiko Hinatsu in our laboratory who has helped a lot in providing the simulation using the commercial software ISIS-CFD FINE/Marine during this research. The validation of our experiment would be incomplete without his support.

Besides, Professor Yonghwan Kim at Seoul National University (SNU), South Korea for the fruitful discussion and providing the experimental data of the 6750-TEU container ship which conducted at Korea Research Institute of Ship & Ocean Engineering (KRISO). Using this segmented wave-load data on a ship-hull enabled us to discuss the notable validation of our proposed method, for which I am thankful.

Recognition to Professor Hidetaka Houtani currently at the University of Tokyo who was being a researcher in the Seakeeping Performance Research Group, Fluids Engineering & Ship Performance Evaluation Department of the National Maritime Research Institute (NMRI) of Japan and also his fellow Dr. Yasushi Kitagawa. Being the person-in-charge for my summer internship, their kindness, and experiences in his research field helped me a lot in learning the towing tank experiment of the ship seakeeping and structural problems. Also for all their helps during my stay for which I am grateful.

I am delighted to belong to a fantastic laboratory with enjoyment and supporting members. I should appreciate considerably the positive atmosphere of pursuing a graduate study. For all lab members and university colleagues, I would like to thank for the lively friendship.

At the end of the foremost important, I am always indebted to my dearest parents, my beloved wife Ayu, and my precious one Zahra whose all the time prayers have been the most powerful support and reason for my life.

After all, I should acknowledge every single individual whose contribution is worth to mention. I sincerely thank everyone without exception.

Sincerely yours.

Osaka, August 2020

Kurniawan Teguh Waskito

Contents

List of Figures

List of Tables

Chapter 1

Introduction

1.1 Background

Prediction of wave-induced shearing force and bending moment as the wave loads on a ship is of vital importance for evaluating the ships structural strength in waves, and hence accurate prediction of wave loads on ships is required. In the analysis of fluid-structure interactions especially for large ships, the so-called two-way coupling in the analysis is prerequisite to account for the influence of flexible deformation of a ship. In fact, much work has been made on ship hydroelasticity problems so far, thereby various methods have been developed for both frequency- and time-domain problems [3–6]. However, the quasi-static response analysis is still deemed as the practical method particularly in the early stage of structural design rather than the direct calculation method involving the dynamic response analysis which is more time-consuming. For that reason, evaluation of the bending moment taking account of primarily rigid-body motions is a dominant part in the study on the wave loads.

Comprehensive reviews on the progress in the assessment of wave loads for ships and offshore structures have been presented by the Loads Committee in the ISSC [7, 8] and also by the Seakeeping Committee in the ITTC [9]. For instance, Hirdaris *et al.* [7] summarized related papers published basically in the past three years up to 2011, and Temarel *et al.* [8] reviewed the progress made in the next three years up to 2014 in the area of wave-induced loads; in which the advantages and disadvantages of various computation methods including relatively simpler potential-flow approaches and time-consuming CFD methods are discussed with reference to accuracy, modeling nonlinear effects, ease of modeling and coupling with structural assessment procedures, and so on. In particular, CFD methods making use of RANS equations are promising for solving complicated seakeeping problems which include various nonlinearities related to large-amplitude waves, resultant ship motions and ships actual wetted surface, and also forward-speed effects on wave loads and other motion-related hydrodynamic quantities. A

good survey of the history in the application of CFD methods to seakeeping problems at least up to 2012 is provided by Guo *et al.* [10]. Not only survey but also computation was made of the wave-induced ship motions of and added resistance on KVLCC2 tanker model especially in short waves by using the ISIS-CFD flow solver, FINE/Marine V 2.2, and they also did careful grid convergence and uncertainty analyses for numerical results. Thanks to dramatic advances of computer technology and science, the number of papers on seakeeping nonlinear problems with CFD methods is increasing over the last decade. Among them, we can see recent work in Niklas *et al.* [11] computing the added resistance using STAR-CCM+ and in Judge *et al.* [12] computing the slamming pressure using CFDShip-Iowa V 4.5. Use of OpenFOAM for seakeeping problems is also increasing recently, such as Wang *et al.* [13] and Xu *et al.* [14] to name a few. However, most of them are concerned with pressure-integrated global quantities like wave-induced ship motions and added resistance, and few papers treat the unsteady spatial pressure distribution and resultant wave loads.

Looking back at the work on the wave loads done in the 1980s in Japan [15–18], it was already noted principally with experimental work that the nonlinearity in the sagging and hogging moments must be taken into account for sufficiently accurate prediction of the vertical bending moment. However, in order to assess this kind of nonlinear effects on the wave loads by numerical computations, the time-domain analysis methods must be used [19–21]. Recently some of the methods using nonlinear potential-flow approaches [22] or CFD methods employing RANS or even URANS models [23, 24] have been investigated. Nevertheless, the examples of studies using CFD methods on the wave loads or local pressure histories are fewer in number, e.g. [25–27]. Among them, it should be noted that Hänninen *et al.* [28] computed local pressure histories at ten locations around the still water line in the bow area of a passenger ship using an interface-capturing CFD method ISIS-CFD. Then as a validation, computed results were compared with measured results in the experiment conducted by themselves. Notwithstanding advancement of computer performance, computation efficiency is still needed to consider from the practical viewpoint [29, 30] in the study of wave loads and seakeeping problems.

On the other hand, to date, the wave loads computed by the potential-flow approaches or CFD methods have been validated through comparisons with experiments featuring various ship hulls with different level of nonlinearities at extreme seas [31–35]. Nonetheless, most of the work focused only on integrated values such as hydrodynamic forces acting on the entire ship hull and ship motions in waves. To attain more thorough understanding of hydrodynamic features, local hydrodynamic quantities like spatial distribution of the pressure on the hull surface of a ship should be checked. From a viewpoint of wave-load measurement conducted so far in a towing tank, segmented ship models have been commonly used [36, 37] in which the wave loads could be measured only at segmented sections with load cell installed. However, we need to obtain the distribution of wave loads at any longitudinal position of a ship with higher accuracy and to account for the nonlinearity in the wave loads; which could be realized by measuring the spatial

distribution of unsteady pressure on the whole ship-hull surface and by properly integrating it in conjunction with the measurement of ship motions and time-variant wetted surface of a ship in waves.

For that purpose, we have conducted an unprecedented experiment at Research Institute for Applied Mechanics (RIAM), Kyushu University in 2018 using a bulk carrier ship model. Measured in that experiment were the unsteady pressure distribution by means of a large number of Fiber Bragg Gratings (FBG) pressure sensors [38, 39], [1]) and simultaneously the wave-induced ship motions and ship-side wave profile. As a matter off fact, the experiment for measuring the unsteady pressure on a ship in head waves started in 2015, and the measurement has been repeated with FBG pressure sensor improved year by year through collaboration with the company manufacturing this sensor, CMIWS Co., Ltd, and then repeatability and reliability in measured results have been confirmed [40–42]. Although the number of FBG sensors used in 2015 was 28, the total number of sensors affixed to the ship model has been increased year by year to enhance the density of measurement and to resolve the nonlinearity in the pressure above still waterline. In the experiment in 2018, we used version 6.0 of the FBG sensor and 333 FBG pressure sensors were affixed only on the port side of a ship considering the symmetrical pressure field in head waves, among which 70 sensors were placed above the still waterline to see nonlinearities. Using these measured data, a study is made in this paper on the waveload distribution. To figure out nonlinear effects on the pressure distribution and resultant wave loads in a precise manner, the analysis is commenced from the zero-speed case in which the responses of the pressure and ship motions can be regarded as linear. Meanwhile, nonlinear responses of wave loads are studied for a forward-speed case, where an asymmetric and hence nonlinear feature in sagging and hogging moments is demonstrated by using the pressure distribution and wave-induced ship motions measured at synchronized time instants. Some comparisons are made by means of the linear potential theory of RPM developed by Iwashita *et al.* [43] as well as a commercial CFD software FINE/Marine V 8.2 [2] solving the RANS equations to see nonlinear effects and features in the vertical bending moment. A comparative study with the benchmark data on wave-induced motions and loads of a 6750-TEU container ship adopted for the ITTC-ISSC joint workshop in 2014 [44] is also made for further validation.

1.2 Objective

Although comparisons are made between measured and computed results, the main objective of the present study is not the validation of the computation methods used but the acquisition of the spatial distribution of wave-induced unsteady pressure only with experimental measurement. The obtained data can be used for hydrodynamic study on the local quantities like the distribution of wave loads and added resistance, particularly the longitudinal distribution of the vertical

bending moment in this paper. The obtained data can also be used as the validation data for CFD methods, but more importantly, with CFD methods used as a guide in the analysis of measured data, we can establish a new experimental technique to see the details in the wave-load distribution and consequently enhance the level of our understanding of nonlinear and forward-speed effects on wave loads in terms of the experimental data obtained.

In **Chapter 2**, describes the experiment in 2018 using the RIOS (Research Initiative on Ocean-going Ships) bulk carrier which conducted in the towing tank of RIAM, Kyushu University [43, 45, 46]. The measurement of ship-side wave and spatial pressure distribution using Fiber Bragg Grating (FBG) sensors was conducted to obtain precise information of the coincide time histories of ship-side wave profiles, hydrodynamic pressures as well as wave-induced ship motion. Ship-side wave elevation was measured by capacitive wave gauge installed on 30 ordinates throughout the ship's length. On the other hand, the spatial pressure distribution was measured by 333 FBG pressure sensors affixed on the port side on the same ordinate as the ship-side wave measurement and 19 strain-type pressure sensors embedded on the starboard side only at ordinate number 5.0, 9.0 and 9.5. The same experimental condition was conducted at $Fn = 0.18$ at the wavelength range of $0.3 \sim 2.0$ in regular head-wave. The motion-free test was conducted with the amplitude of incident wave within the range of linear theory. Eventually, ship-side wave, spatial pressure distribution, wave-induced ship motion, wave height, and hydrodynamic forces acting longitudinal direction for the added resistance could be measured. Furthermore, for a fundamental check of whether the linear superposition is satisfied, the measurement of pressure distribution has been performed for the diffraction and radiation problems simultaneously with direct measurement of the total force by a dynamometer. The analysis of motion-free and linear superposition test (diffraction and radiation problems) is then elucidated subsequently.

In **Chapter 3**, formulation and computational methods used in the present study are elucidated. First, for comparison with measured results in the experiment, numerical computations based on the linear potential-flow theory are implemented using the 3D frequency-domain Rankine panel method (RPM) [43, 46, 47]. Despite the RPM was developed for the forward-speed problems, we have applied RPM for the zero-speed case in the present study by modifying a numerical method to satisfy the radiation condition. To discuss nonlinear and forward-speed effects to be obvious in the wave-induced unsteady pressure on the ship-hull surface, we used a commercial CFD software, FINE/Marine V 8.2. [2], which is based on the ISIS-CFD flow solver developed at Ecole Centrale de Nantes (ECN). The simulation set-up refers to the recommended value in the user manual of FINE/Marine for the computation in the present study. For analysis of ship-side wave, to synchronize the time histories of unsteady physical quantities measured in the experiment i.e. wave-induced ship motions and hydrodynamic pressure on the ship hull, the origin of time should be taken equal to the time instant when the crest of incident wave measured at the origin of the coordinate system. For analysis of pressure, the static pressure when the ship does not move in still water was taken as the zero-base. Thus the time histories of measured

pressure fluctuate around zero. However, the data obtained by pressure sensors affixed around the still waterline must be of rectified pulse-type signals, because the sensor positions repeat coming out and plunging into water. The procedure for rectifying physically unreasonable time histories was elucidated. Once the time history of the pressure has been rectified, the Fourier-series analysis incorporating higher-order terms is made for the pressure time histories.

In **Chapter 4**, formulation of the vertical bending moment is described as the prominent component of wave loads. There are two components in VBM owing to the integration of unsteady pressure and the inertia force [48]. These components are time-variant and nonlinear. Then, the integration of unsteady pressure and the inertia force throughout the ship's length to obtain the vertical bending moment acting on the transverse section as well as the transformation from body-fixed to space-fixed coordinates are explained. In the last part, the weight distribution used in the present study which is under the assumption of uniform structural density is depicted.

In **Chapter 5**, the results of experiment and its comparisons with the computation are outlined. First, the measured ship-side wave is presented and the shifting coefficient for each ship-side wave is obtained. Afterward, the same transformation is applied to synchronize the time histories of other quantities such as wave-induced ship motions and hydrodynamic pressure on the ship hull in the subsequent analysis. After that, the validation of measured unsteady pressure distribution is presented. The previous validation has been made by Iwashita *et al.* [39, 40, 42, 43] and Kashiwagi *et al.* [1, 41] compared the measured results with computed value based on the linear potential-flow theory in addition in the present study another validation is discussed which the first-harmonic wave-exciting forces from the integration of unsteady pressure distribution measured for the diffraction problem is compared with the corresponding forces measured directly with a dynamometer. Following that, the easier case of vertical bending moment at zero-speed in head waves is discussed. Vertical bending moment is computed using the unsteady pressure and the motions RAOs for which the comparison is made for the measured results and the computation by the linear potential theory Rankine panel method (RPM). Taking into account the nonlinear case at the resonant frequency $\lambda/L = 1.25$ of forward-speed $Fn = 0.18$ in head waves more discussion is made for the vertical bending moment between the measured results and the computation by CFD concerning the nonlinearity of hogging and sagging as well as the effect of forward-speed. Another crucial comparison is then made for the vertical bending moment measured directly at a specified transverse section by a segmented ship model for a wide range of wavelengths. Therefore, the analysis method is further validated through comparison with the benchmark data of a 6750-TEU container ship which used segmented hulls.

In **Chapter 6**, obtained results and discussion in the present study are summarized.

Chapter 2

Experiment

In chapter 2, describes the detailed experiment. The experiment was conducted in the towing tank (its length, breadth, and depth are 65 m, 5 m, and 7 m, respectively) of RIAM, Kyushu University. The tank has a plunger-type wave maker with wedge inclination angle of 40 deg at one end and a wave-absorbing beach at the other end. The wave maker can be activated remotely with the signal from a computer specifying the amplitude and frequency of the driving motor. In the experiment in 2018, we used the RIOS (Research Initiative on Oceangoing Ships) bulk carrier made of urethane [43], [45], [46] whose principal particulars are shown in Table 2.1. To obtain the accurate information of the time instant of ship-side wave profiles coinciding with the spatial pressure distribution on ship hull We conducted the measurement of ship-side wave and spatial pressure distribution using Fiber Bragg Grating (FBG) sensors. The motion-free test was conducted mainly in the ship-side wave and spatial pressure distribution. However, the diffraction and forced-oscillation tests were conducted as well to validate the reliability of FBG sensors. The same principal particulars of RIOS bulk carriers were used in the experiment and will be presented in the following sections.

TABLE 2.1: Principal particulars of RIOS bulk carrier model

Item	Value
Length: L_{pp} (m)	2.400
Breadth: B (m)	0.400
Draft: d (m)	0.128
Block coefficient: C_b	0.800
Waterline coefficient: C_w	0.870
Horizontal center of gravity: x_G (m)	0.0510
Vertical center of gravity: z_G (m)	−0.0200
Vertical center of buoyancy: z_B (m)	−0.0618
Gyrational radius in pitch: κ_{yy}/L	0.250

2.1 Ship-Side Wave

2.1.1 Ship Model & Test Condition

Fig. 2.1 shows the RIOS bulk carrier model used in the ship-side wave experiment. Ship-side waves were measured in several conditions as shown in table 2.2. Once ship-side waves could be measured, the instant wetted ship hull surface could be identified. This information is important when considering hydrodynamic force, wave exciting force, and added resistance calculating by pressure integration.

FIGURE 2.1: RIOS bulk carrier model for ship-side wave measurement

TABLE 2.2: Ship-side wave experimental conditions

Froude number	Incident wave [deg]	λ/L
Fn=0.18	180	0.3, 0.4, 0.5, 0.8, 1.0, 1.25, 1.5, 2.0

2.1.2 Wave Gauge

For measuring wave elevation on the ship-side, a capacitive wave gauge is used. Fig. 2.2 presents the capacitive type installed on the ship hull surface. Wave gauges are installed on 30 sections ordinate in total (Ord. 0.25~ Ord. 10.00) and the wave gauge positions on the body plan are shown in Fig. 2.3.

Calibration was conducted before measuring the ship-side wave. The static force was given on the ship, and the calibration coefficient was calculated from the obtained capacitance and the actual wave elevation. By multiplying the obtained coefficient to experimental data, the actual ship-side wave on each ordinate position can be measured.

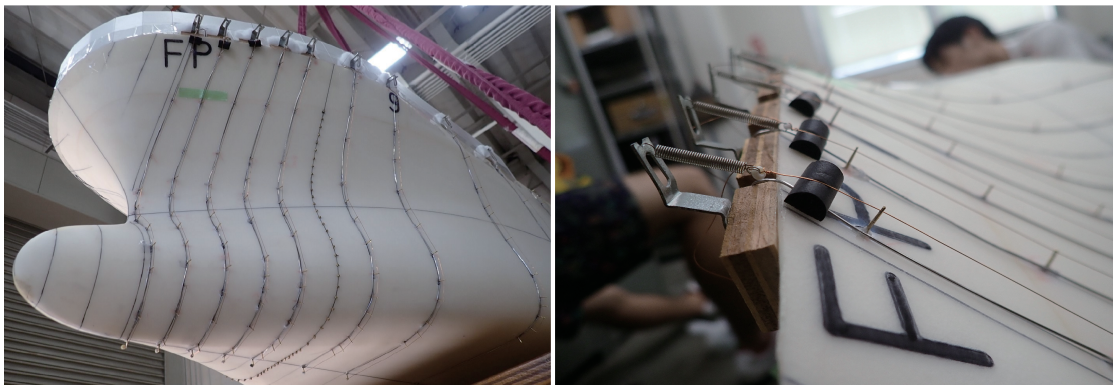

FIGURE 2.2: Photo of ship model and position of wave gauge

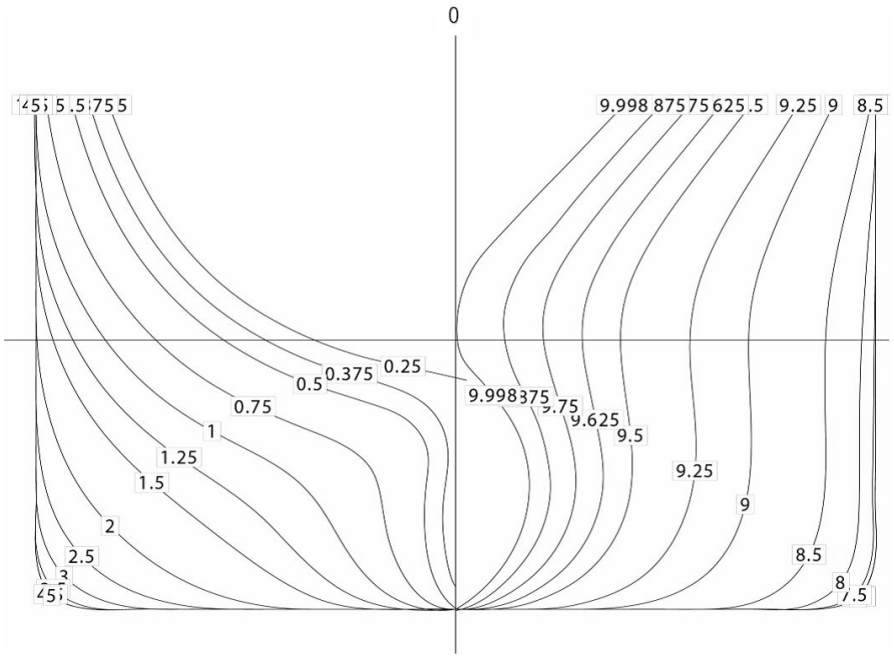

FIGURE 2.3: Body plan and positions of wave gauges

2.1.3 Wave Measurement System

Fig. 2.4 shows a schematic system for measuring the wave elevation on ship hull surface. Table 2.3 shows the channel number of each equipment. The ship-side wave was measured simultaneously by all capacitive wave gauges connected to BNC connect box. Data logged on universal

recorder were synchronized with a trigger signal that came up when the fore perpendicular went through the position of space-fixed wave probe. The analysis interval is determined two periods before and after the trigger point. Logged data were A/D converted and Fourier-analyzed.

The experiment was conducted at $Fn = 0.18$ in regular head-wave with motion-free condition. Whilst the $Fn = 0.18$ at the wavelength range of 0.3~2.0 will be used in connection with the experiment of spatial pressure distribution. The amplitude of incident wave in the motion-free test was set within the range of linear theory ($2\zeta_a/\lambda \leq 1/30$). In this experiment, we measured not only ship-side waves but also other data like wave height, wave-induced ship motions (surge, heave, and pitch), and hydrodynamic forces acting longitudinal direction for the added resistance. The motion-free test condition was conducted in which the ship model was free to surge, heave, and pitch. In this condition ship-side wave, wave-induced ship motions, and hydrodynamic forces are measured simultaneously and also independently corresponding to the schematic diagram without any interference from each other.

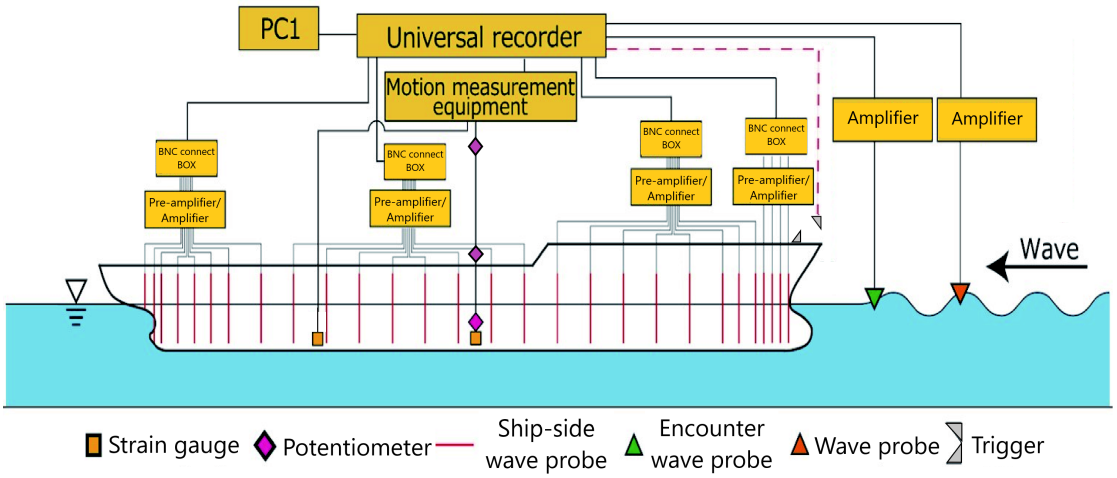

FIGURE 2.4: Data Acquisition system for measuring the ship-side wave

TABLE 2.3: Measurement channels of the ship-side wave experiment

Channel	Item
Ch. 1	Trigger
Ch. 2	Wave-0 (carriage-fixed wave probe)
Ch. 3	Surge
Ch. 4	Heave
Ch. 5	Pitch
Ch. 6	Longitudinal force, $F_{x(f)}$ (fore)
Ch. 7	Longitudinal force, $F_{x(a)}$ (after)
Ch. 8	Wave-1 (space-fixed wave probe)
Ch. 9-36	Ship-side wave measurement

2.2 Spatial Pressure Distribution

2.2.1 Ship Model & Test Condition

In the spatial pressure distribution experiment the principal particulars of the ship model of RIOS bulk carrier are the same as in 2.2. The experimental condition is shown in Tables (2.4). Fig. 2.5

Table 2.4: Experimental condition at forward speed case in head waves

Item	Condition
Incident wave angle: β	180 degrees
Incident wavelength: λ/L	$0.3 \leq \lambda/L \leq 3.0$
Incident wave height: $H = 2\zeta_a$	$2\zeta_a/\lambda \leq 1/30$ or $\zeta_a \leq 2.4$ cm
Froude Number: F_n	0.18

shows the body plan and also the position of pressure sensors, in which 333 FBG pressure sensors in total (including 70 sensors above the still waterline) were affixed on the port side (see Fig. 2.5) and 19 strain-type pressure sensors were embedded in the starboard side (only at ordinate numbers 5.0, 9.0 and 9.5, indicated by green-color square symbol in Fig. 2.5) to check the measurement accuracy of the FBG pressure sensors. Since the experiment was performed in regular head waves, the pressures at the same symmetric points on both sides of a ship must take the same value; with this principle, measured values by the FBG and strain-type pressure sensors can be compared and the accuracy can be confirmed. The FBG pressure sensor used is ps 1000A-V6 manufactured by CMIWS Co., Ltd and the strain-type pressure sensor used is P306V-05S manufactured by SSK Co., Ltd.

The ship model was free to surge, heave, and pitch. When the model was towed by the carriage at a constant speed, the mean position of the model was controlled by pulling the model (in fact the fore heaving rod mentioned later) with an adjusted force induced by a servo motor, which was realized by adjusting manually the electric current to a servo motor while monitoring the mean position of the model even in a wave that the ship model would be oscillating in surge. Then the wave-induced ship motions in surge, heave, and picth were measured by potentiometers and the resistance was measured by strain gauges installed at the bottom of fore and rear heaving rods (see Figs. 2.7 and 2.9). These measurements can be done at the same time with measurement of the pressure (which will be explained below) but these are independent and there is no interference with each other.

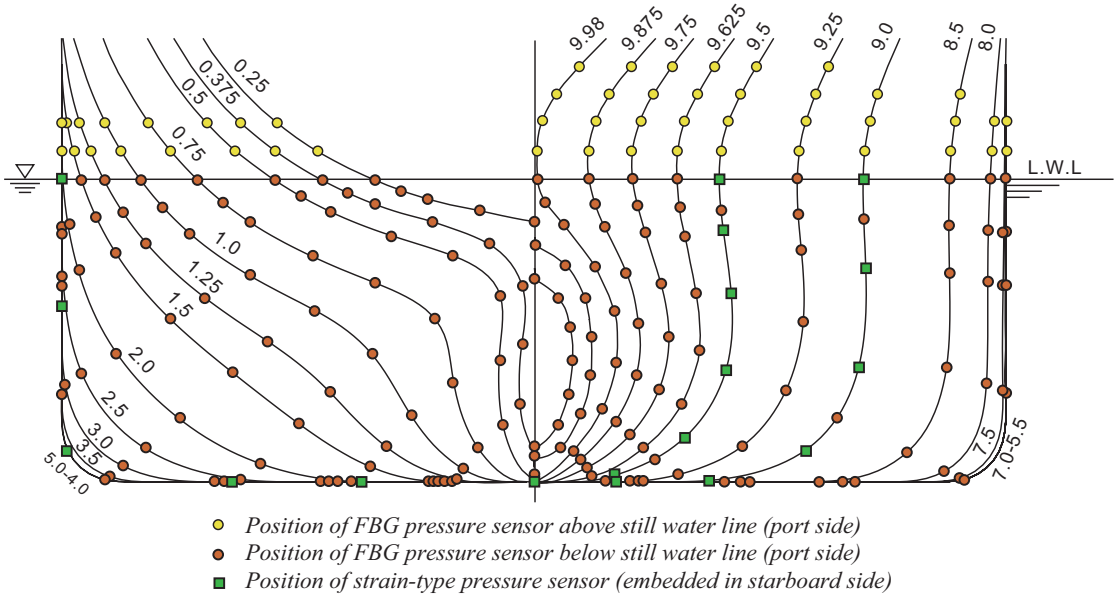

(a) Body plan and position of pressure sensors

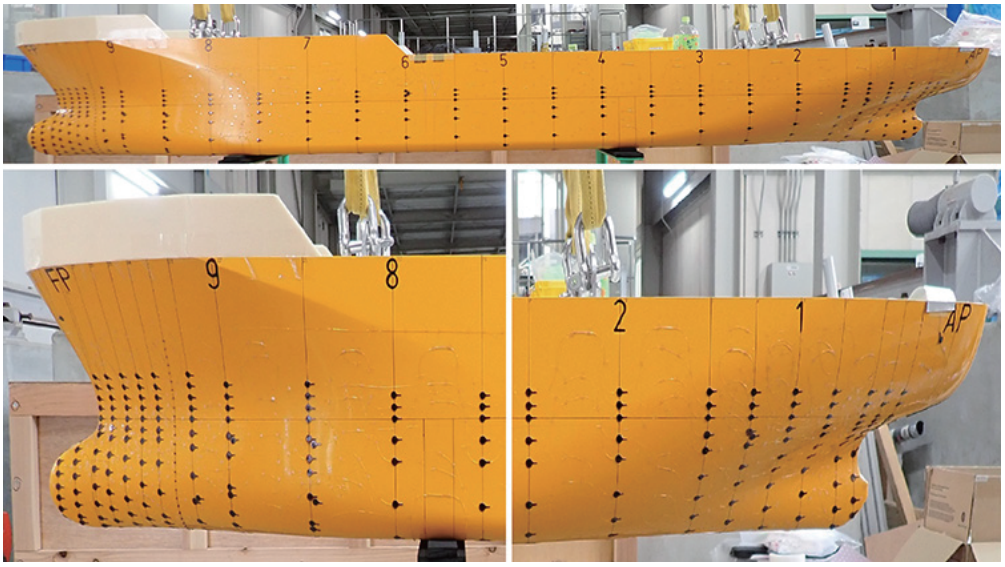

(b) Photo of ship model and position of pressure sensors

FIGURE 2.5: RIOS bulk carrier model; (a) Body plan, (b) Position of pressurre sensors

2.2.2 FBG Pressure Sensors

The mechanism and measurement principle of the FBG pressure sensor are explained by Wakahara *et al.* [38] and Iwashita *et al.* [39]. The FBG is a type of distributed diffraction grating etched into the optical fiber core that reflects a particular wavelength of light, called Bragg wavelength, and transmits the remainder. If the spacing between reflectors changes due to variation of pressure load or temperature, the Bragg wavelength also changes. Thus by identifying a

change in the Bragg wavelength in terms of the calibration coefficient obtained beforehand, the pressure can be measured.

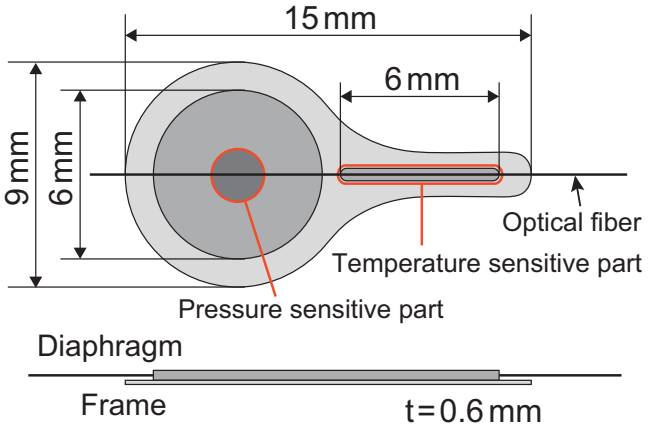

FIGURE 2.6: FBG sensor used in the experiment [1]

Reliability of the sensor has been improved year by year since 2015 by minimizing the effect of temperature variation on the pressure to be measured and the size of the sensor itself. Fig. 2.6 shows a schematic diagram of the FBG sensor Version 6.0 [1] used in the experiment in 2018, with 9 mm in diameter, 15 mm in length, and 0.6 mm in thickness. One sensor can measure the pressure and temperature at the same time, because two FBGs with different spacings of Bragg grating are contained in one sensor and fixed in order not to interfere with each other. Therefore, the effect of temperature variation on the pressure measurement can be compensated in principle. It is also possible to arrange many (in the order of 10–15) FBG sensors with different spacing of Bragg grating along one optical fiber, so that the simultaneous multipoint measurement can be made.

2.2.3 Calibration Test

The calibration curve for FBG sensors can be written as

$$P(x, y, z; t) = C_p(\Delta\lambda_p - S_t\Delta\lambda_t)\, C_f \tag{2.1}$$

where $\Delta\lambda_p$ and $\Delta\lambda_t$ denote the amount of change in the Bragg wavelength due to variation of the pressure and temperature, respectively. S_t is the compensation factor to account for the effect of temperature variation and its value is around 0.6 and less than 1.0. C_p denotes the calibration coefficient proportional to a change in the Bragg wavelength. The calibrated values of C_p and S_t are provided for each FBG sensor by CMIWS Co., Ltd based on a laboratory test, but they tend to change and differ in actual measurement. Thus the correction coefficient C_f must be obtained from the calibration measurement in situ, which was done by providing several

different hydrostatic pressures on the pressure sensors. In order to alter the hydrostatic pressure, the vertical position of the ship model was changed with the adjustable lifting and lowering rig attached to the ship model (see Fig. 2.7). Before a calibration measurement, the ship model was pressed downward so that all the sensors were in water. Then the ship model was lifted up and stopped step by step with 2.0 mm each and up to 2 cm in the end. The measurement in the inverse direction was also performed by pressing down the model with 2.0 mm each to confirm linearity and no hysteresis.

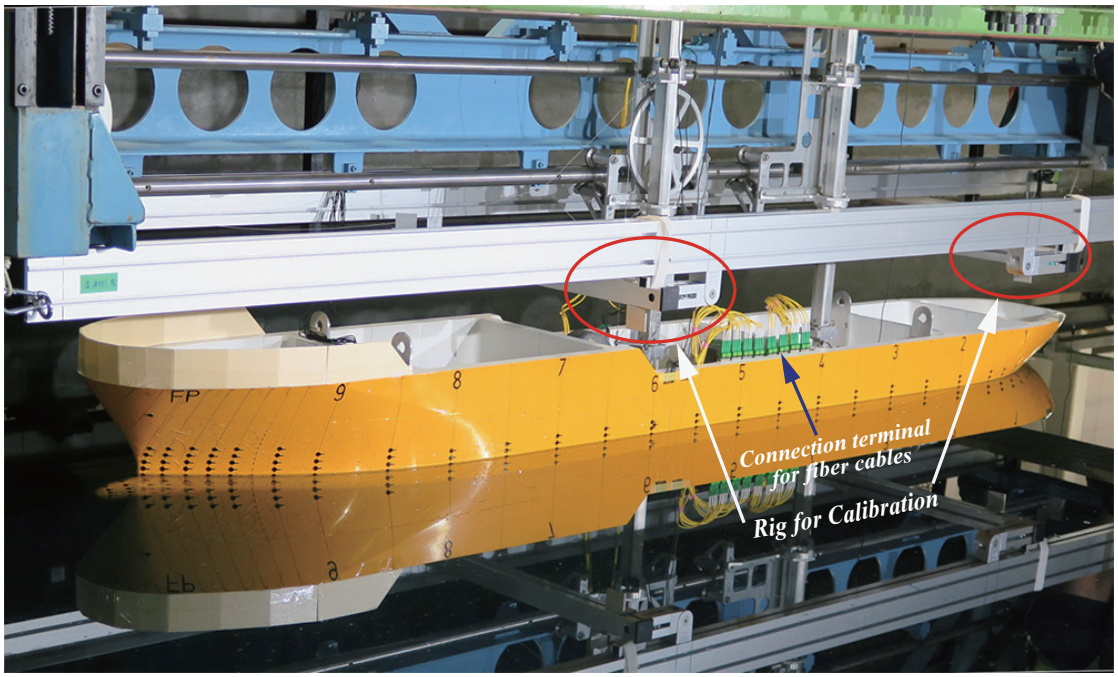

FIGURE 2.7: Overview of ship model set to the towing carriage and measurement system, showing connection terminal of optical fiber cables

Figure 2.8 shows some samples of the calibration response at 4 typical positions taken among 333 sensors. We could see a linear response at all positions and the values are virtually the same both when pressing down and lifting up the model (i.e. no hysteresis). However, a difference from the theoretical value of hydrostatic pressure can be observed at some positions, from which the correction coefficient C_f in Eq. (3.1) was determined in terms of a least-squares method for all 333 sensors automatically with a personal computer (PC) used in the in-situ analysis. This calibration measurement has been carried out, whenever necessary, without removing any instrument in the experimental set-up.

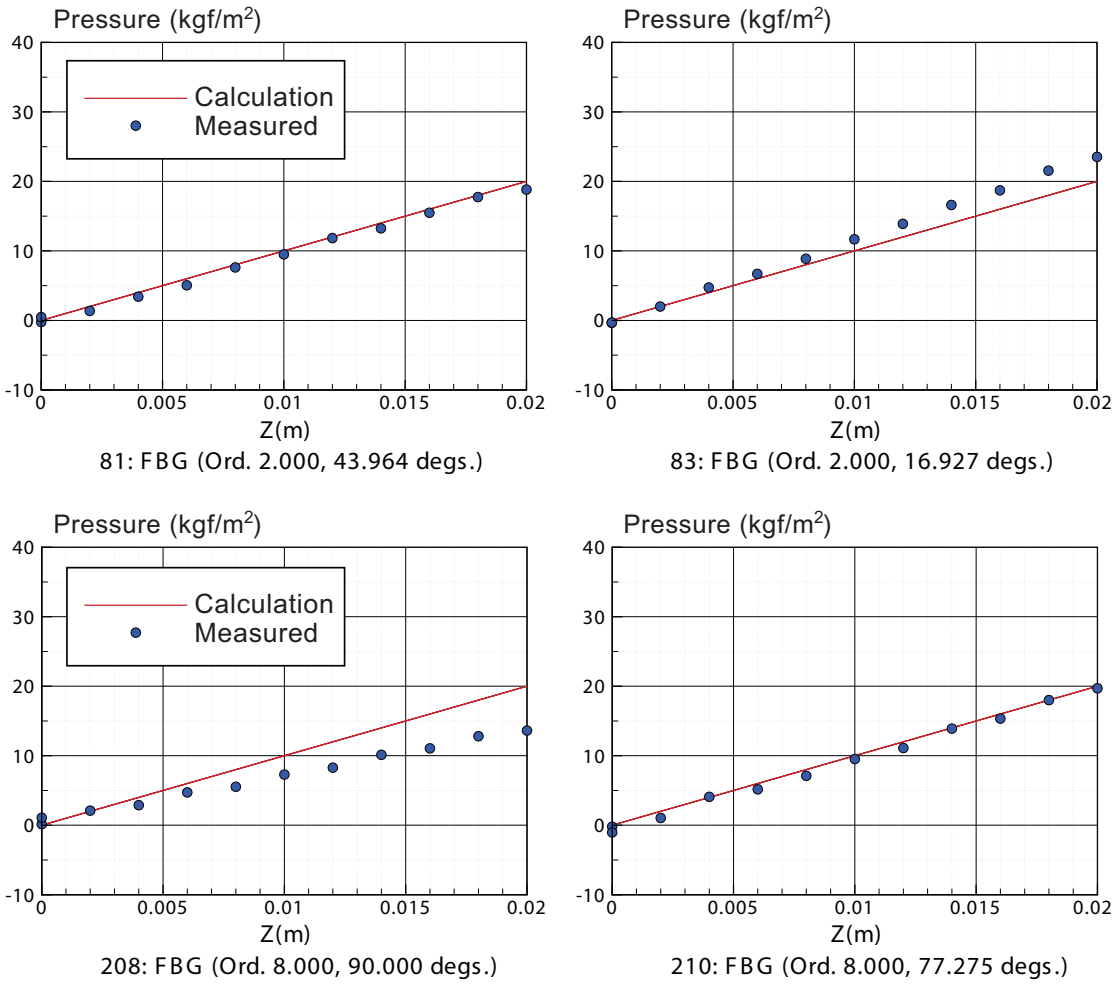

FIGURE 2.8: Samples of calibration results for FBG pressure sensor

2.2.4 Spatial Pressure Measurement System

The schematic arrangement of the data measurement and acquisition system is depicted in Fig. 2.9 and the cannel number of each item is presented in Table 2.5. The pressure was measured simultaneously by all FBG sensors connected to the optical interrogators. The green-color part is the recording system for FBG pressure sensors and the orange-color part for other electric equipments like wave probes, potentiometers, strain-type sensors and so on. Data recorded on different computers (indicated as PC1 and PC2 in Fig. 2.9) were synchronized with a trigger signal which came up when the fore perpendicular of the ship went through the position of space-fixed wave probe. Because of large amount of data, the data sampling frequency was set to 200 Hz, which implies that 133,200 data of the pressure and temperature were transferred to a PC per second. Recorded data were A/D converted and Fourier-analyzed. More details for the Fourier analysis will be described in the subsequent section.

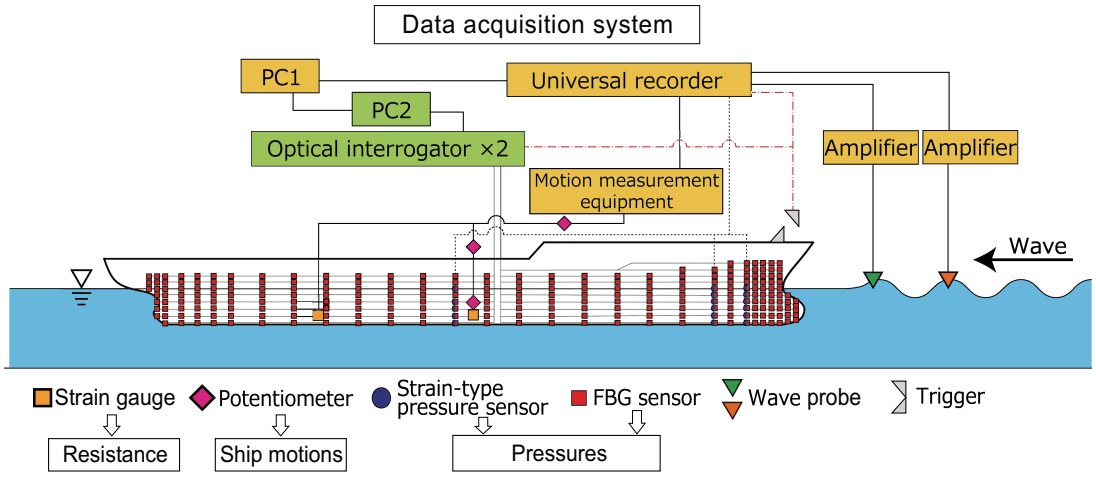

FIGURE 2.9: Data acquisition system for measuring the spatial pressure distribution

TABLE 2.5: Measurement channels of the spatial pressure experiment

Channel	Item
Ch. 1	Trigger
Ch. 2	Wave-0 (carriage-fixed wave probe)
Ch. 3	Surge
Ch. 4	Heave
Ch. 5	Pitch
Ch. 6	Longitudinal force, $F_{x(f)}$ (fore)
Ch. 7	Longitudinal force, $F_{x(a)}$ (aft)
Ch. 8	Wave-1 (space-fixed wave probe)
Ch. 9-27	Strain-type pressure sensors
Ch. 28-360	FBG pressure sensors

The experiment was conducted at $Fn = 0.0$ and 0.18 in regular head waves at the wavelength range of 0.3~3.0 with motion-free condition, measuring not only the pressure distribution but also hydrodynamic forces and wave-induced ship motions (surge, heave, and pitch). In addition, the ship-side wave, i.e. the wave profile on the ship-hull surface, was measured in advance using capacitance-type wave gauges which were installed on another ship model made of urethane with the same geometry and dimensions. Since these wave gauges were set along the girth with small separation gap from the hull surface and at the same transverse sections as those for measuring the pressure, we can detect the correct wetted surface of ship hull at each time instant, which is of critical importance for the pressure integration over the ship-hull surface and for computing resultant hydrodynamic forces.

The amplitude of incident wave in the motion-free test was set within the range of linear theory ($2\zeta_a/\lambda \leq 1/30$). Furthermore, for a fundamental check whether the linear superposition is

satisfied, the measurement of pressure distribution has been performed for the diffraction (with motion fixed in waves) and radiation (with prescribed motions in calm water) problems, together with direct measurement of the total force by a dynamometer. The experiments for the diffraction and radiation problems were carried out by setting the ship model to another equipment for the forced oscillation test.

One serious problem we realized during the experiment conducted in September of 2018 was that the repeatability in measured results tends to be influenced by the temperature difference between water and air, especially when its value of the difference becomes larger than 1.0 °C. Therefore we decided to perform the measurement during the midnight while confirming the temperature difference, Δt, satisfies an experience-based condition of $\Delta t < 1.0$°C. This issue on the effect of temperature variation on the accuracy of measured results is now being improved by the sensor company and will be provided as version 7.0 of the FBG pressure sensor.

2.3 Motion-free Test

The schematic diagram of motion-free test is shown in Fig.2.10. The ship model is towed by the carriage at a constant speed and free to surge, heave, and pitch motions (the symmetric mode of motions). The wave-induced ship motions of surge, heave, and pitch are measured by the potentiometer installed at the heaving rods, and resistances are measured by strain gauges installed at the bottom of fore and rear heaving rods. Besides, the incident wave is measured by the servo type wave probe installed at the carriage-fixed also at the space-fixed system. Furthermore, as explained in the Section 2.1 and 2.2, the ship-side wave and spatial pressure distribution are also measured accordingly. Measured items on the motion-free test are presented in Table (2.6)

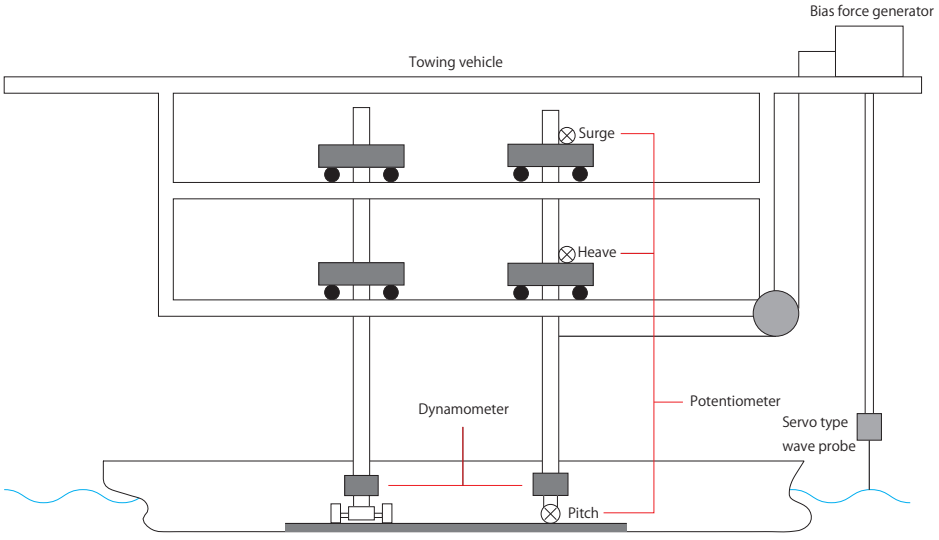

FIGURE 2.10: Outline of motion-free test

Table 2.6: Measured items on the motion-free test

Measured Item	Measuring Equipment
Incident wave amplitude: ζ_a	Wave height meter -Capacitance type-
Incident wave phase: ϵ_ω	Wave height meter -Servo type-
Resistance in x direction: R_{total}	Dynamometer
Surge motion: ξ_1	Potentiometer
Heave motion: ξ_3	Potentiometer
Pitch motion: ξ_5	Potentiometer
Unsteady pressure: Pt	Pressure gauge

Added wave resistance R_{AW} can be obtained from steady components in waves are subtracted by the steady resistance in calm sea as follows:

$$R_{AW} = \overline{R_{\text{unsteady}}} - \overline{R_{\text{steady}}} \tag{2.2}$$

where the overbar means taking time-average.
Nondimensional of ship motions are expressed as follows:

$$\xi_j^{\text{nondim}} = \frac{\xi_j}{\zeta_a} \quad (j = 1, 2, 3) \tag{2.3}$$

$$\xi_j^{\text{nondim}} = \frac{\xi_j}{k_0 \zeta_a} \quad (j = 4, 5, 6). \tag{2.4}$$

Nondimensional added wave resistance can be expressed as

$$R_{AW}^{\text{nondim}} = \frac{R_{AW}}{\rho g \zeta_a^2 (B^2/L)} \tag{2.5}$$

2.4 Diffraction Test

The linear superposition experiment of diffraction and radiation tests for the forward speed case in head wave was conducted to validate the motion-free test. Hence, the experimental condition is the same as the motion-free problem. In diffraction test, wave-exciting forces are measured acting on a ship advancing in waves under the condition that ship motions are fixed. The schematic diagram of the diffraction test is shown in Fig.2.11 and the measured items are shown in Table (2.7). In the case of validation, the spatial pressure distribution by FBG sensors was validated by integrating all the pressure over the ship hull and compare with the wave-exciting forces of surge, heave and pitch measured by the dynamometer in ship-fixed (diffraction test) condition. Measured incident waves are discretized by Fourier-expansion based on the en-

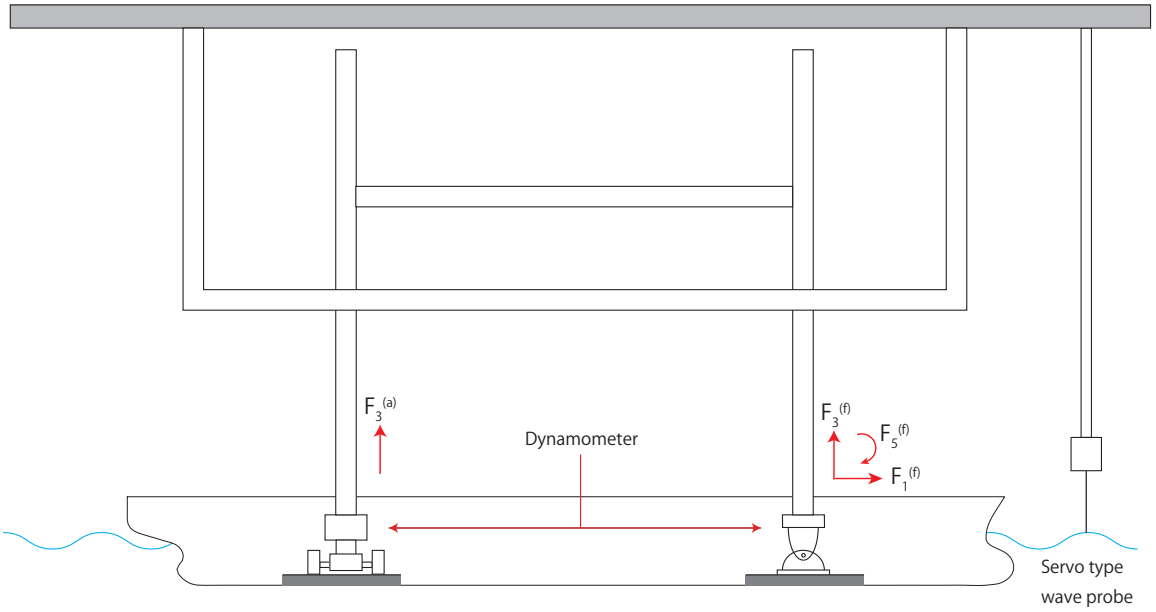

FIGURE 2.11: Outline of wave-exciting force test

TABLE 2.7: Measured items on the diffraction test

Measured Item	Measuring Equipment
Incident wave amplitude: A	Wave height meter -Capacitance type-
Incident wave phase: ϵ_ω	Wave height meter -Servo type-
Resistance in x direction: R_{total}	Dynamometer
Wave exciting force in x direction: F_x	Dynamometer
Wave exciting force in z direction: F_z	Dynamometer
Wave exciting moment around y direction: M_y	Dynamometer

counter frequency ω and following equation can be obtained by neglecting higher-order terms.

$$\zeta == \frac{\zeta_0}{2} + a_1 \cos \omega t + b_1 \sin \omega t \tag{2.6}$$

Then, phase of incident wave δ_w is given as

$$\delta_w = \tan^{-1} \frac{b_1}{a_1}. \tag{2.7}$$

Obtained forces by the dynamometer are deformed as

$$F_j^{(f,a)} \cong \frac{a_0^{(f,a)}}{2} + a_1^{(f,a)} \cos \omega t + b_1^{(f,a)} \sin \omega t \quad (j = 1,\ 3,\ 5). \tag{2.8}$$

Complex forces are presented as

$$f_j^{(f,a)} = a_1^{(f,a)} - i b_1^{(f,a)} \quad (j = 1,\ 3,\ 5). \tag{2.9}$$

By using forces expressed as Eq.(2.9), each force is coupled as

$$\begin{aligned} E_1 &= f_1^{(f)} = X_0 + \overline{F_x}\cos(\omega t - \delta_x) \\ E_3 &= f_3^{(f)} + f_3^{(a)} = \overline{F_z}\cos(\omega t - \delta_z) \\ E_5 &= f_5^{(f)} + (f_3^{(a)} - f_3^{(f)})\ell + (\ell_m + OP)f_1^{(f)} = \overline{M_y}\cos(\omega t - \delta_y). \end{aligned} \tag{2.10}$$

where ℓ is lever from midship to load cell, ℓ_m height from center-of-rotation P to center of load cell, and OP length from O to center-of-rotation P. Nondimensional wave-exciting forces can be expressed as follows:

$$E_1^{\text{nondim}} = \frac{\overline{F_x}}{\rho g \zeta_a A_w}, \quad \epsilon_x = \delta_x - \delta_w \tag{2.11}$$

$$E_3^{\text{nondim}} = \frac{\overline{F_z}}{\rho g \zeta_a A_w}, \quad \epsilon_z = \delta_z - \delta_w \tag{2.12}$$

$$E_5^{\text{nondim}} = \frac{\overline{M_y}}{\rho g \zeta_a A_w L}, \quad \epsilon_y = \delta_y - \delta_w \tag{2.13}$$

Added resistance ΔR_{AW} can be obtained by the comparison between steady component of resistance in waves $\overline{X_0}$ and steady resistance in calm sea, R_s. In this case, $\overline{X_0}$ takes forward as positive direction.

$$\Delta R_{AW} = (-\overline{X_0}) - R_s \tag{2.14}$$

$$R_{AW}^{\text{nondim}} = \frac{\Delta R_{AW}}{\rho g \zeta_a^2 (B^2/L)} \tag{2.15}$$

2.5 Forced-oscillation Test

In radiation test, the added mass and damping coefficients are obtained by measuring hydrodynamic forces and moment acting on a ship with the oscillation advancing in calm sea. Schematic diagram of measurement system is shown in Fig.2.12 and the measured items are shown in Table (2.8).

Table 2.8: Measured items on the radiation problem

Measured Item	Measuring Equipment
Incident wave phase: $\epsilon_j (j = 3, 5)$	Potentiometer
Resistance in x direction: R_{total}	Dynamometer
Wave exciting force in x direction: F_x	Dynamometer
Wave exciting force in z direction: F_z	Dynamometer
Wave exciting moment around y direction: M_y	Dynamometer

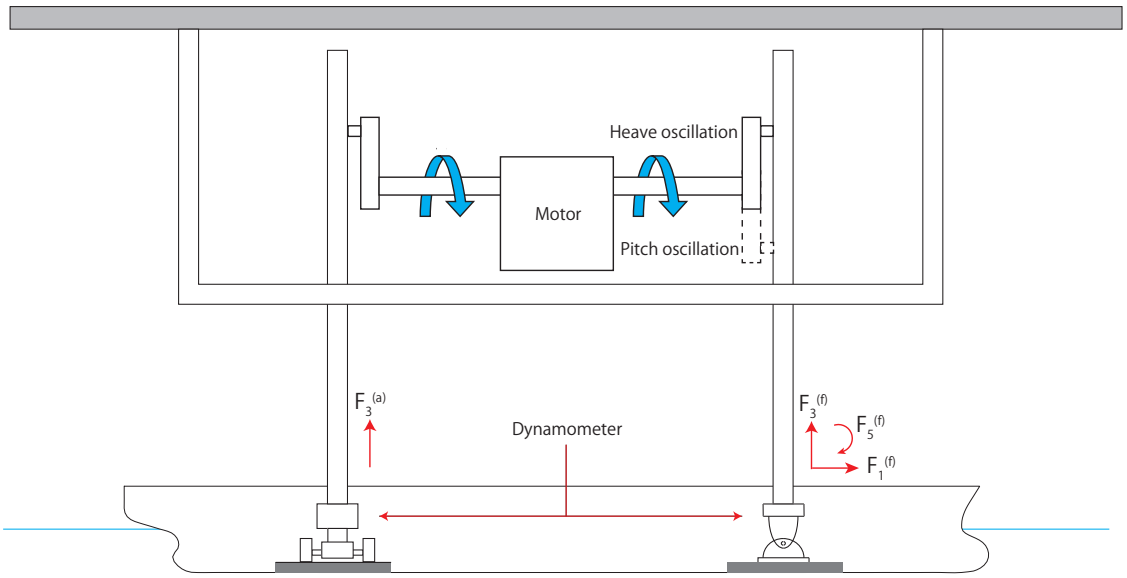

FIGURE 2.12: Outline of forced-oscillation test

In forced-heave oscillation test, the following motion is given.

$$\begin{aligned} &\Xi_1 = 0, \quad \Xi_5 = 0 \\ &\Xi_3 = \mathrm{Re}[\xi_3 e^{i\omega t}], \quad \xi_3 = \overline{\xi_3} e^{i\varphi_3} \end{aligned} \tag{2.16}$$

Measured Ξ_3 are discretized by Fourier-analysis based on the frequency of obtained motion ω. Following equation can be obtained by neglecting higher-order terms.

$$\Xi_3 = \frac{a_0}{2} + a_1 \cos \omega t + b_1 \sin \omega t \tag{2.17}$$

From Eq.(2.17), the complex amplitude can be obtained as follows:

$$\xi_3 = a_1 - ib_1 = \overline{\xi_3} e^{i\varphi_3}, \quad \overline{\xi_3} = \sqrt{a_1^2 + b_1^2}, \quad \varphi_3 = \tan^{-1} \frac{-b_1}{a_1}. \tag{2.18}$$

Obtained foeces are deformed by Fourier-analysis as

$$F_j^{(f,a)} \cong \frac{a_0^{(f,a)}}{2} + a_1^{(f,a)} \cos \omega t + b_1^{(f,a)} \sin \omega t \quad (j = 1,\ 3,\ 5). \tag{2.19}$$

Complex forces $f_j^{(f,a)}$ can be presented as

$$f_j^{(f,a)} = a_1^{(f,a)} - ib_1^{(f,a)} \quad (j = 1,\ 3,\ 5). \tag{2.20}$$

By using forces expressed as Eq.(2.20), each force is coupled as

$$\begin{aligned} f_1 &= f_1^{(f)} \\ f_3 &= f_3^{(f)} + f_3^{(a)} \\ f_5 &= f_5^{(f)} + (f_3^{(a)} - f_3^{(f)})\ell + (\ell_m + OP)f_1^{(f)}. \end{aligned} \tag{2.21}$$

By using Eq.(2.21), the added mass and damping coefficients are obtained as follows:

$$\frac{A_{13}}{\rho\nabla} = -\frac{\mathrm{Re}(-f_1/\xi_3)}{\omega^2\rho\nabla} \tag{2.22}$$

$$\frac{B_{13}}{\rho\nabla\omega} = \frac{\mathrm{Im}(-f_1/\xi_3)}{\omega^2\rho\nabla} \tag{2.23}$$

$$\frac{A_{33}}{\rho\nabla} = -\frac{\mathrm{Re}(-f_1/\xi_3) - \omega^2(\rho\nabla + \Delta m_1 + \Delta m_2) + C_{33}}{\omega^2\rho\nabla} \tag{2.24}$$

$$\frac{B_{33}}{\rho\nabla\omega} = \frac{\mathrm{Im}(-f_3/\xi_3)}{\omega^2\rho\nabla} \tag{2.25}$$

$$\frac{A_{53}}{\rho\nabla L} = -\frac{C_{53} - \mathrm{Re}(-f_5/\xi_3)}{\omega^2\rho\nabla L} + \frac{x_G}{L} \tag{2.26}$$

$$\frac{B_{53}}{\rho\nabla\omega L} = \frac{\mathrm{Im}(-f_5/\xi_3)}{\omega^2\rho\nabla L} \tag{2.27}$$

where Δm_1 and Δm_2 the mass under the dynamometers, C_{33} and C_{53} are restoring forces and x_G means the length of the center of gravity in x-direction.

In forced-pitch oscillation test, the following motion is given.

$$\begin{aligned} &\Xi_1 = 0, \quad \Xi_3 = 0 \\ &\Xi_5 = \mathrm{Re}[\xi_5 e^{i\omega t}], \quad \xi_5 = \overline{\xi_5} e^{i\varphi_5}, \quad \overline{\xi_5} = \tan^{-1}(\overline{\xi_3}/\ell) \end{aligned} \tag{2.28}$$

Measured Ξ_5 are discretized by Fourier-analysis based on the frequency of obtained motion ω. Following equation can be obtained by neglecting higher-order terms.

$$\Xi_5 = -\tan^{-1}\frac{\Xi_3}{\ell} = \frac{a_0}{2} + a_1\cos\omega t + b_1\sin\omega t \tag{2.29}$$

From Eq.(2.29), the complex amplitude can be obtained as follows:

$$\xi_5 = a_1 - ib_1 = \overline{\xi_5} e^{i\varphi_5}, \quad \overline{\xi_5} = \sqrt{a_1^2 + b_1^2}, \quad \varphi_5 = \tan^{-1}\frac{-b_1}{a_1}. \tag{2.30}$$

Obtained foeces are deformed by Fourier-analysis as

$$F_j^{(f,a)} \cong \frac{a_0^{(f,a)}}{2} + a_1^{(f,a)}\cos\omega t + b_1^{(f,a)}\sin\omega t \quad (j = 1,\ 3,\ 5). \tag{2.31}$$

Complex forces $f_j^{(f,a)}$ can be presented as

$$f_j^{(f,a)} = a_1^{(f,a)} - ib_1^{(f,a)} \quad (j = 1,\ 3,\ 5). \tag{2.32}$$

By using forces expressed as Eq.(2.32), each force is coupled as

$$\begin{aligned} f_1 &= f_1^{(f)} \\ f_3 &= f_3^{(f)} + f_3^{(a)} \\ f_5 &= f_5^{(f)} + (f_3^{(a)} - f_3^{(f)})\ell + (\ell_m + OP)f_1^{(f)}. \end{aligned} \tag{2.33}$$

By using Eq.(2.33), the added mass and damping coefficients are obtained as follows:

$$\frac{A_{15}}{\rho\nabla L} = -\frac{\mathrm{Re}(-f_1/\xi_5)}{\omega^2\rho\nabla L} - \frac{z_G}{L} \tag{2.34}$$

$$\frac{B_{15}}{\rho\nabla\omega L} = \frac{\mathrm{Im}(-f_1/\xi_5)}{\omega^2\rho\nabla L} \tag{2.35}$$

$$\frac{A_{55}}{\rho\nabla L^2} = -\frac{\mathrm{Re}(-f_5/\xi_5) - \omega^2(\rho\nabla\kappa_{yy}^2 + \Delta I_1 + \Delta I_2) + C_{55}}{\omega^2\rho\nabla L^2} \tag{2.36}$$

$$\frac{B_{55}}{\rho\nabla\omega L^2} = \frac{\mathrm{Im}(-f_5/\xi_5)}{\omega^2\rho\nabla L^2} \tag{2.37}$$

$$\frac{A_{35}}{\rho\nabla L} = -\frac{C_{35} - \mathrm{Re}(-f_3/\xi_5)}{\omega^2\rho\nabla L} + \frac{x_G}{L} \tag{2.38}$$

$$\frac{B_{35}}{\rho\nabla\omega L} = \frac{\mathrm{Im}(-f_3/\xi_5)}{\omega^2\rho\nabla L} \tag{2.39}$$

where ΔI_1 and ΔI_2 are the inertia moments due to the mass under the dynamometer, κyy is the gyrational radius with respect to y axis, C_{35} and C_{55} are restoring forces and z_G means the length of the center of gravity in z-direction.

Chapter 3

Formulation & Computational Method

In Chapter 3, elucidates the formulation and computational methods used in the present study. In the first section, describes numerical computations based on the linear potential-flow theory. The following section describes the computational fluid dynamics method to discuss nonlinear and forward-speed effects in the wave-induced unsteady pressure on the ship-hull surface. The subsequent section explains the analysis of the ship-side wave to synchronize the time histories of unsteady physical quantities measured in the experiment. The last section describes the analysis of pressure in connection with the analysis of the ship-side wave.

3.1 Potential Flow Theory

For a comparison with measured results in the experiment, numerical computations based on the linear potential-flow theory were implemented using the 3D frequency-domain Rankine panel method (RPM) with the formulation as described in [43], [46] and [47]. Although this RPM was basically developed for the forward-speed problems, we have applied RPM for the zero-speed case in the present study by modifying a numerical method to satisfy the radiation condition, as will be described below.

Because of zero forward speed, the velocity potential for harmonic oscillation problems can be written as

$$\Phi(x, y, z; t) = \mathrm{Re}[\, \phi(x, y, z) e^{i\omega t} \,] \tag{3.1}$$

where the time-dependent part is written with circular frequency ω, and $\phi(x, y, z)$ is the spatial part of the velocity potential which is given in a form of linear superposition as

$$\phi(x, y, z) = \frac{ig\zeta_a}{\omega}(\,\phi_0 + \phi_7\,) + i\omega \sum_{j=1}^{6} X_j \phi_j \tag{3.2}$$

where ζ_a denotes the amplitude of incident wave, g the gravitational acceleration, X_j the complex amplitude in j-th mode of six degree-of-freedom ship motions. Re in Eq. (3.1) means only the real part of the expression must be taken. The velocity potential of incident wave is denoted as ϕ_0 which is given explicitly as

$$\phi_0 = e^{Kz - iK(x\cos\chi + y\sin\chi)} \tag{3.3}$$

Here the coordinate system in the present analysis is taken such that the positive x- and y-axes are in the bow and port directions of a ship, respectively, and the z-axis is positive vertically upward with the origin taken on the undisturbed free surface $z = 0$ and at the midship. The wavenumber of incident wave is given as $K = \omega^2/g$, and χ denotes the incident angle of an incoming regular wave relative to the x-axis and hence $\chi = \pi$ means the head wave.

The unsteady velocity potential ϕ_j in Eq. (3.2) denotes the radiation ($j = 1 \sim 6$) and scattering ($j = 7$) velocity potentials; which is governed by the Laplace equation and expressed by a source distribution over the body surface S_H and the free surface S_F, with Rankine source used as the kernel function. Namely

$$\phi_j(\mathrm{P}) = \iint_{S_H + S_F} \sigma_j(\mathrm{Q})\, G(\mathrm{P}, \mathrm{Q})\, dS(\mathrm{Q}) \tag{3.4}$$

where $\mathrm{P} = (x, y, z)$ denotes a field point in the fluid and $\mathrm{Q} = (x', y', z')$ the integration point on the boundary surface, and

$$G(\mathrm{P}, \mathrm{Q}) = \begin{cases} G_0(\mathrm{P}, \mathrm{Q}) + G_0\text{`}(\mathrm{P}, \mathrm{Q}) & \text{when Q on } S_H \\ G_0(\mathrm{P}, \mathrm{Q}) & \text{when Q on } S_F \end{cases} \tag{3.5}$$

$$G_0(\mathrm{P}, \mathrm{Q}) = -\frac{1}{4\pi\, r} \qquad G_0'(\mathrm{P}, \mathrm{Q}) = -\frac{1}{4\pi\, r'} \tag{3.6}$$

$$\left.\begin{matrix} r \\ r' \end{matrix}\right\} = \sqrt{(x - x')^2 + (y - y')^2 + (z \mp z')^2} \tag{3.7}$$

Here $\sigma_j(\mathrm{Q})$ in Eq. (3.4) denotes the strength of sources which is unknown. $G_0'(\mathrm{P}, \mathrm{Q})$ is the mirror image of $G_0(\mathrm{P}, \mathrm{Q})$ reflected in the undisturbed free surface ($z = 0$) and hence $G_0(\mathrm{P}, \mathrm{Q}) + G_0'(\mathrm{P}, \mathrm{Q})$

satisfies the rigid-wall boundary condition on $z = 0$.

In case of zero forward speed, the linearized free-surface boundary condition is given in the form

$$\frac{\partial \phi_j}{\partial z} - K\phi_j = 0 \quad \text{on } z = 0 \tag{3.8}$$

and the linearized body boundary condition on the wetted hull surface of a ship can be expressed in the form

$$\left.\begin{aligned} \frac{\partial \phi_j}{\partial n} &= n_j \qquad (j = 1 \sim 6) \\ \frac{\partial \phi_7}{\partial n} &= -\frac{\partial \phi_0}{\partial n} \quad (j = 7) \end{aligned}\right\} \text{ on } S_H \tag{3.9}$$

where $(n_1, n_2, n_3) = \boldsymbol{n}$ denotes the normal vector pointing into the fluid from the boundary surface and $(n_4, n_5, n_6) = \boldsymbol{r} \times \boldsymbol{n}$, with $\boldsymbol{r} = (x, y, z)$ the position vector. The unknown source strength $\sigma_j(\mathrm{Q})$ must be determined such that the boundary conditions, Eqs. (3.8) and (3.9), are satisfied. The procedure for obtaining an integral equation for the source strength is as follows.

When the field point P is located on the boundary (S_H or S_F), the normal derivative of Eq. (3.4) can be written in the form

$$\frac{1}{2}\,\sigma_j(\mathrm{P}) + \iint_{S_H+S_F} \sigma_j(\mathrm{Q})\,\frac{\partial\, G(\mathrm{P},\mathrm{Q})}{\partial\, n_P}\,dS\,(\mathrm{Q}) = \frac{\partial \phi_j(\mathrm{P})}{\partial\, n_P} \tag{3.10}$$

Specifically when P is on S_H, the body boundary condition Eq. (3.9) must be specified as the forcing term on the right-hand side, and when P is on S_F (note that $z = 0$), the free-surface boundary condition can be satisfied by substituting the following equation into the right-hand of Eq. (3.10)

$$\frac{\partial \phi_j(\mathrm{P})}{\partial\, n} = -\frac{\partial \phi_j(\mathrm{P})}{\partial\, z} = -K\,\phi_j(\mathrm{P}) \tag{3.11}$$

This free-surface boundary condition gives the following homogeneous form of integral equation:

$$\frac{1}{2}\,\sigma_j(\mathrm{P}) + \iint_{S_H+S_F} \sigma_j(\mathrm{Q})\left\{\frac{\partial\, G(\mathrm{P},\mathrm{Q})}{\partial\, z} - K\,G(\mathrm{P},\mathrm{Q})\right\} dS\,(\mathrm{Q}) = 0 \tag{3.12}$$

The resulting equations on S_H and S_F can be expressed as a series of algebraic equations by discretizing the boundary surfaces with appropriate smaller panels and assuming the source strength $\sigma_j(\mathrm{Q})$ to be constant on each panel. Integrations of the Rankine source and its normal dipole over each panel are necessary, which are performed with analytical formulae established by Newman [49]. Then we can obtain a solution by solving a linear system of simultaneous

equations for the source strength on S_H and S_F. Once the source strength is determined, the velocity potential can be computed from Eq. (3.4), then the hydrodynamic forces in the radiation and diffraction problems can be computed.

The wave radiation condition is satisfied numerically by the so-called panel shift technique [43], shifting the collocation points by one panel upstream on the free surface. In order to avoid wave reflection from the outward boundary which can disturb the flow around a ship, we use Rayleigh's artificial friction which is equivalent to introducing a numerical damping beach on the free surface. In this case, we can transform the wavenumber K in Eq. (3.8) into a complex quantity with small negative imaginary part. Namely Eq. (3.8) is transformed as

$$\frac{\partial \phi_J}{\partial z} - (K - i\epsilon)\phi_j = 0 \quad \text{on } z = 0 \tag{3.13}$$

Here ϵ is a function of (x, y) on the free surface that may be specified as [33]

$$\epsilon = \frac{\omega}{g}\alpha \left\{ 1 - e^{-\beta(R-1)} \right\} \quad \text{for } R \geq 1 \tag{3.14}$$

where $R = \sqrt{x^2 + y^2}$ is the distance from the origin of the coordinate system and all length dimensions are normalized with half length of a ship $L/2$. The values of α and β must be tuned and are taken as $\alpha = 0.5$ and $\beta = 1.5$ in the present study.

A computation mesh with quadrilateral-type panels of total number 5,032 on the ship hull and 5,320 on the free surface is shown in Fig. 3.1. The number of panels on the free surface was set with longitudinal and lateral lengths equal to $-2L \leq x \leq 0.5L$ and $2L$, respectively, which was confirmed to be sufficient to prevent disturbance waves from the outward boundary and to provide reasonable and converged results of hydrodynamic forces.

3.2 Computational Fluid Dynamics Method

In order to discuss nonlinear and forward-speed effects to be seen in the wave-induced unsteady pressure on the ship-hull surface, we have used a commercial CFD software, FINE/Marine V 8.2 [2], which is based on the ISIS-CFD flow solver developed at Ecole Centrale de Nantes (ECN), solving the incompressible RANS equations with an unstructured finite volume method and Volume-of-Fluid (VOF) type interface capturing method for detecting the free surface between air and water. Mathematical details in the development of ISIS-CFD are described by Queutey and Visonneau [50].

For simulating free-surface flows and their interactions with an advancing ship, the use of interface capturing methods is effective. In order to enhance the sharpness of the interface, many

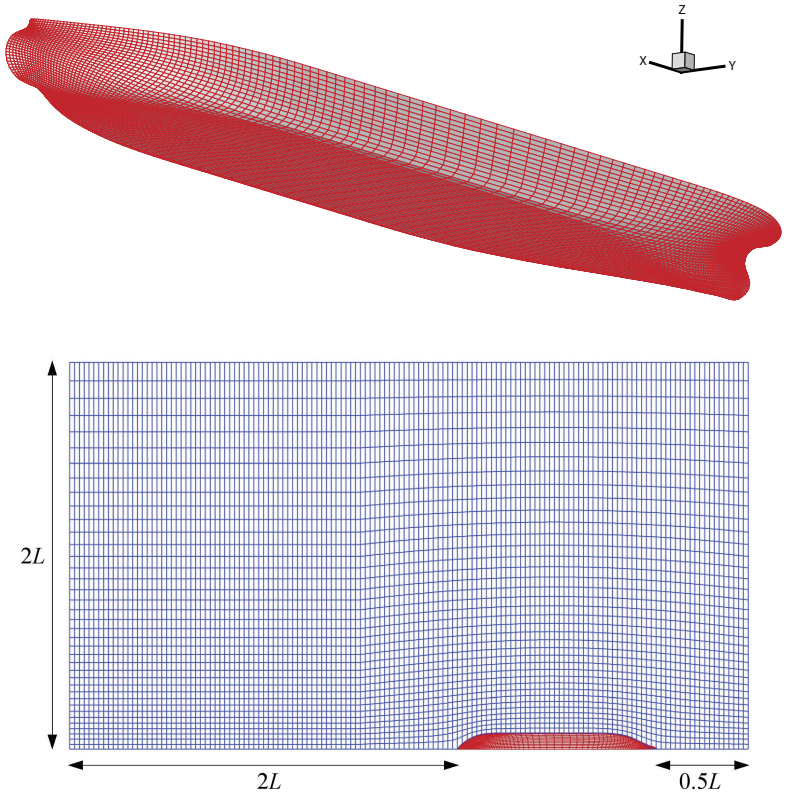

FIGURE 3.1: Computational mesh of RPM for RIOS bulk carrier, Upper: ship-hull surface mesh, Lower: free-surface mesh

studies have been made. For a review of the development of various interface capturing techniques, we can refer to Wackers *et al.* [51], which also describes the details of ISIS-CFD flow solver together with validation results. Application of ISIS-CFD flow solver to unsteady seakeeping problems was shown by Guo *et al.* [10], and careful and systematic study on uncertainty and convergence using 4 different meshes was performed, which shows the reliability and accuracy of computed results for the prediction of ship motions and added resistance. Hänninen *et al.* [28] also applied ISIS-CFD solver to compute the time histories of local pressure at 10 locations around the still waterline in the bow area of a passenger ship. By using 3 different meshes, they have checked the dependency of numerical results on the mesh resolution, the time step per wave period, and the iteration number within a time step, thereby confirming reliability of the method, although the computational cost is still very high.

Judging from these results obtained so far regarding the reliability of the ISIS-CFD flow solver for seakeeping problems, it may be appropriate to use FINE/Marine as an analysis tool for hydrodynamic discussion on the experimental results to be obtained in the present study.

This CFD code solves the incompressible unsteady RANS equations using the finite volume method to generate the spatial discretization of the equations. The governing equations for an incompressible flow are the Navier-Stokes and continuity equations. In treating turbulent flows,

it is common to separate the velocity vector into mean and fluctuating parts as follows:

$$u_i = \overline{u}_i + u_i' \tag{3.15}$$

where an overbar denotes the average value and u_i' the fluctuating component. Then the averaged Navier-Stokes and continuity equations can be written as

$$\frac{\partial \overline{u}_i}{\partial t} + \overline{u}_j \frac{\partial \overline{u}_i}{\partial x_j} = -\frac{1}{\rho}\frac{\partial \overline{p}}{\partial x_i} + \nu \nabla^2 \overline{u}_i + g\,\delta_{i3} - \frac{\partial}{\partial x_j}\overline{u_i' u_j'} \tag{3.16}$$

$$\frac{\partial \overline{u}_j}{\partial x_j} = 0 \tag{3.17}$$

where ρ and ν denote the density and kinematic viscosity coefficient of the fluid, respectively, and δ_{i3} is the Kronecker's delta, equal to 1 only for $i = 3$.

Because of existence of the last term in Eq. (3.16), which is due to the Reynolds stress $-\rho\,\overline{u_i' u_j'}$, some kinds of turbulence modeling must be normally introduced. The k - ω SST model [52] [53] is adopted for the simulation with FINE/Marine.

TABLE 3.1: Summary of schemes used in the CFD simulations by FINE/Marine [2]

Item	Scheme used
Grid system	Unstructured, non-conformal, fully hexahedral grid
Spatial discretization	Finite volume method
Advection term	QUICK 3rd-order upwind difference
Viscous diffusion term	2nd-order central difference
Time marching	Backward difference, sub-iteration with virtual time
Coupling between pressure and velocity	Projection method solving Poisson's equation
Free-surface capturing	VOF method (BRICS scheme)
Turbulence model	k - ω SST
Body-surface boundary condition	Logarithmic function as wall function

Table 3.1 shows a summary of the schemes used in the present CFD simulation. Details refer to FINE/Marine V,8.2 [2]. In Fig. 3.2, only half of the ship hull is used in the calculations, thus a symmetry boundary condition is adopted at the center plane boundary. Box 1 represents the domain of the incident wave coming from inlet wave generator, ship-hull, and vortex. Thus, the mesh density of this domain was set to be relatively fine to prevent the numerical attenuation of the wave. Boxes 2, 3 and 4 represent the downstream domain which contains the numerical damping zone. Within this zone, a sponge layer acts as a damping medium in z-direction [2]. Since the Kelvin waves created by the ship will be dampened by the damping zone behind the body hence no particular sidewise damping zone is needed. In these domains, the mesh density was relatively coarse to prevent the wave reflection from the external boundary which might interfere with the incident waves as shown in Fig. 3.2.

The inlet boundary was set to external as a wave generator. Both sides of the boundary were set to mirror for the case of head waves to suppress the wave reflection on the side boundary. The outlet boundary was set to external and the speed was 0 m/s at the outer far field. L_{ref} in Fig. 3.2 takes a larger value between ship length L and wavelength λ. H_w is the wave height equal to $2\zeta_a$. Stokes waves from 1st to 3rd order can be applied and the estimation of the wave order is automatically performed according to Fig. 3.3. The 2nd order Stokes waves were used in this simulation considering the tendency in the experimental wave profiles for the head waves simulation with a half body, the ship is set free to heave and pitch, while sway, roll, and yaw are restricted due to symmetry condition.

Regarding the behavior of the mesh when the ship is in motion, two methods should be distinguished; i.e. overset grid method (Chimera approach) and mesh deformation technique. The overset grid method as depicted in Fig. 3.4 can handle larger ship motions than the mesh deformation technique despite the drawback is also followed by some numerical errors associated with the interpolation exchange in the overlapping cells. Considering the importance of large ship motions in nonlinear phenomena however the overset grid method is applied to the present study.

The computational domain represents the numerical towing tank. To obtain good accuracy and

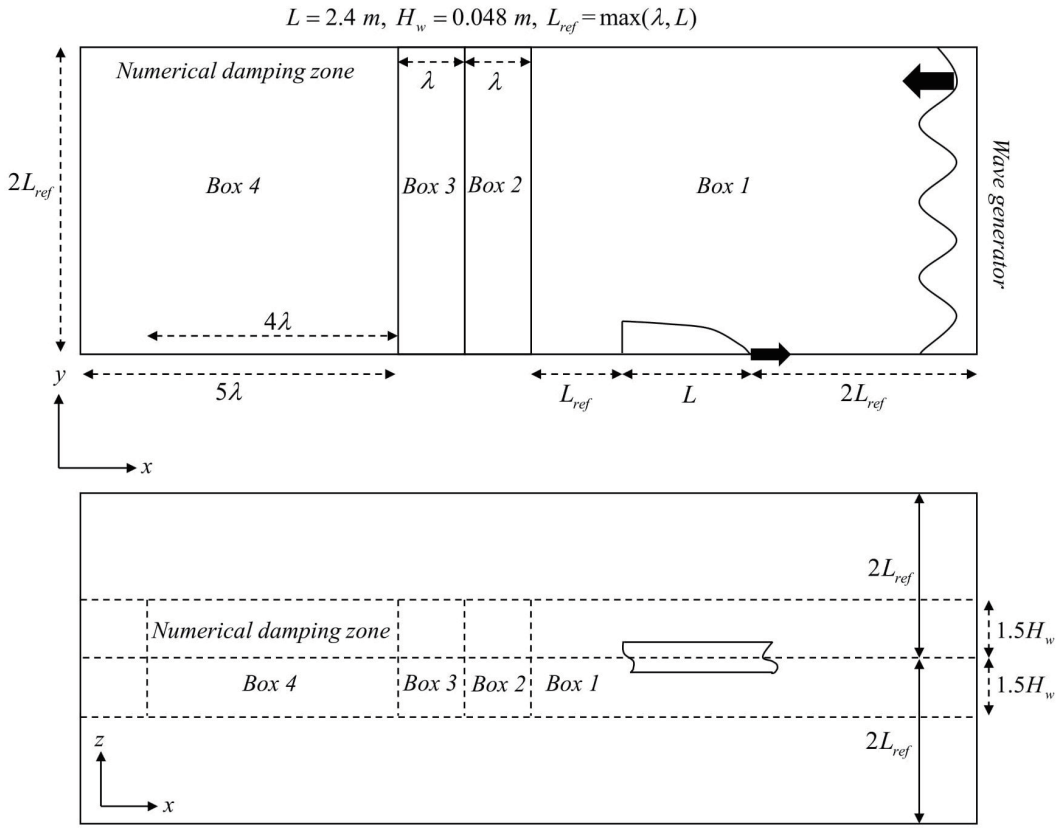

FIGURE 3.2: Calculation domain of CFD computation for RIOS bulk carrier

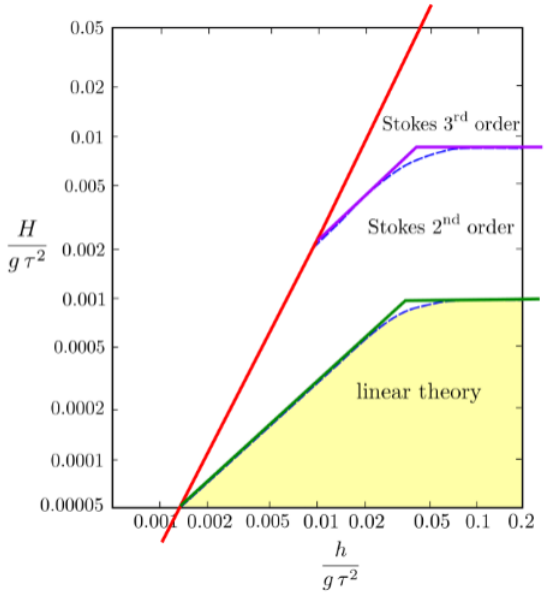

FIGURE 3.3: Estimation of Stokes wave order [2]

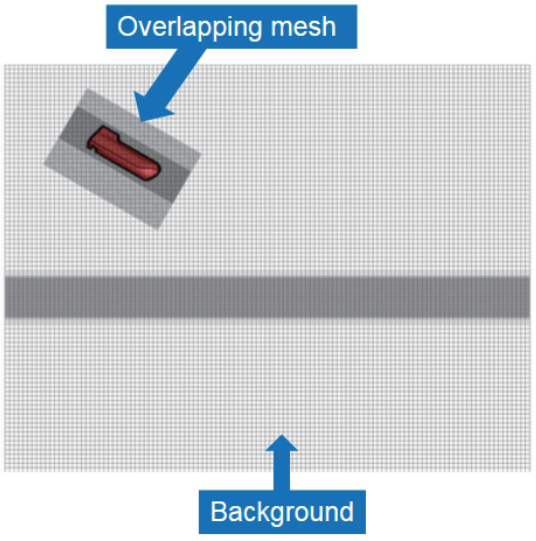

FIGURE 3.4: Overset grid method [2]

efficiency, the size of the domain depends on the problem, i.e. on the ship size, speed as well as the incident waves. In particular, in this study at wavelength of $\lambda/L = 1.25$, the total number of elements was 2,907,979, as shown on the left side of Fig. 3.5 and on the right side of Fig. 3.5, close-up views of the mesh for the bow and stern parts are shown.

The simulation time needs to be divided into discrete time steps. A time step of at least 100 steps per wave period is recommended by the ITTC (2011) [54] and however in this study the time step was taken equal to 1/250 of the encounter period with the incident-wave amplitude equal to 0.0240 m in accordance with the experiment. Use of sub-cycling acceleration enables

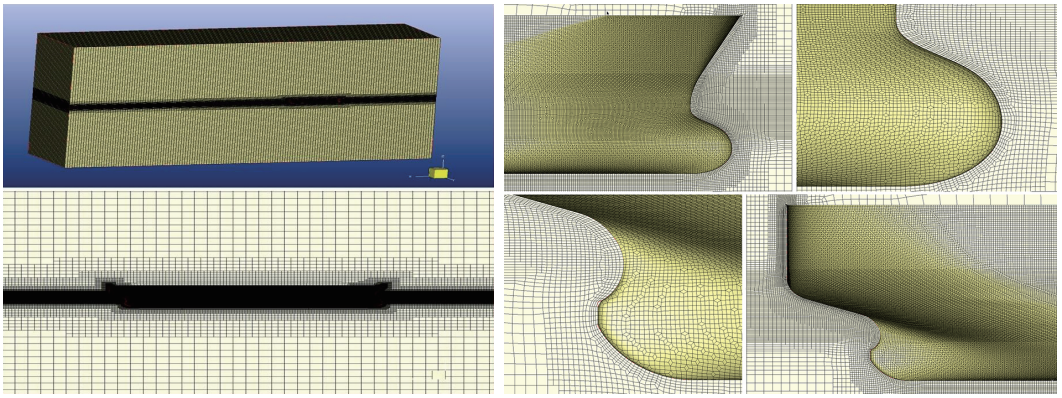

FIGURE 3.5: Computational mesh of CFD for bulk carrier, Left: calculation domain mesh, Right: close-up view of bow and stern part mesh

us to split the global time step ΔT into smaller one dt for which only the volume fraction of the Navier-Stokes equations are solved which supposed to reduce the computational time [2]. For implicit solver like ISIS-CFD the Courant number condition does not apply as the explicit solver [54] and hence the BRICS scheme is applied instead.

For each time step, the solver carries out some non-linear iterations to find the most accurate solution to the system of equations. To satisfy this condition according to the recommendation from FINE/Marine, [2] a number between 12 and 22 non-linear iterations for seakeeping simulations and a convergence criteria of 4 orders of magnitude have been tested although the ITTC (2011) [54] recommends at least 3 orders.

In fact, there are recommended values in the user manual of FINE/Marine for the number of mesh and time step, which were used for the computations in this paper. Furthermore, before implementing the present study, we have studied independently for a simpler problem of incident-wave propagation to check the dependency of numerical results on the number of mesh and time step, and we have confirmed appropriate selection of the parameters; with which we confirmed that virtually no decaying phenomenon exists in an important computational domain around a ship. Therefore we believe that computed results by the CFD method shown in this paper are reliable enough for the purpose of observing underlying physics to be seen in the measured results, although detailed convergence study is not performed by ourselves.

3.3 Analysis of Ship-side Wave

In order to synchronize the time histories of unsteady physical quantities measured in the experiment, the origin of time should be taken equal to the time instant when the crest of incident wave arrives at the origin of the coordinate system. In what follows, we consider a general case that the

forward speed U of a ship exists; hence the circular frequency of encounter ω_e $(= \omega - KU\cos\chi)$ must be used for harmonic oscillation problems.

Suppose that a regular head wave with amplitude ζ_a and wavenumber K $(= \omega^2/g)$ was measured at $x = \ell$ and its first-harmonic component in the Fourier series was obtained in the form

$$\zeta(\ell, t) = \mathrm{Re}\left[\,(\zeta_{\ell c} - i\,\zeta_{\ell s})e^{i\omega_e t}\,\right] = \mathrm{Re}\left[\,(\zeta_{0c} - i\,\zeta_{0s})e^{i(\omega_e t + K\ell)}\,\right] \tag{3.18}$$

Here the complex amplitude at the origin $(x = 0)$ is denoted as $\zeta_{0c} - i\,\zeta_{0s}$, which can be obtained from Eq. (3.18) as

$$\zeta_{0c} - i\,\zeta_{0s} = (\zeta_{\ell c} - i\,\zeta_{\ell s})e^{-iK\ell} \equiv \zeta_0 \equiv \zeta_a e^{i\varphi} \tag{3.19}$$

Therefore the amplitude ζ_a and phase φ can be calculated as

$$\zeta_a = \left|\,\zeta_0\,\right| = \sqrt{\zeta_{\ell c}^2 + \zeta_{\ell s}^2}\,, \quad \varphi = -K\ell - \tan^{-1}\left(\zeta_{\ell s}/\zeta_{\ell c}\right) \tag{3.20}$$

Meanwhile, suppose that the ship-side wave at an arbitrary point $\zeta(t)$ was recorded and its Fourier-series expansion is written as

$$\zeta(t) = \zeta^{(0)} + \sum_{n=1}^{N} \mathrm{Re}\left[\,(\zeta_c^{(n)} - i\,\zeta_s^{(n)})e^{in\omega_e t}\,\right] \tag{3.21}$$

In order to synchronize the phase of this time record with the incident wave measured at the origin, the time-dependent part should be divided by the complex amplitude ζ_0 given by Eq. (3.19). For instance, the first-harmonic component of Eq. (3.21) can be transformed as

$$\mathrm{Re}\left[\,\frac{\zeta_c^{(1)} - i\,\zeta_s^{(1)}}{\zeta_0}e^{i\omega_e t}\,\right] = \mathrm{Re}\left[\,\frac{\zeta_c^{(1)} - i\,\zeta_s^{(1)}}{\zeta_a}e^{i\omega_e(t-\varphi/\omega_e)}\,\right] \tag{3.22}$$

Therefore, the time histories of all ship-side waves measured should be shifted in time with $\Delta t = \varphi/\omega_e$.

In the same way for higher-harmonic components in Eq. (3.21), we can shift the time with $\Delta t = \varphi/\omega_e$ and hence write the ship-side wave record in the form

$$\left.\begin{aligned} \zeta(t) &= \frac{U^2}{2g}\,c_0 + \zeta_a \sum_{n=1}^{N} \mathrm{Re}\left[\,c_n e^{in\omega_e t}\,\right] \\ c_0 &= 2\,K_0\,\zeta^{(0)}\,, \quad c_n = \frac{(\zeta_c^{(n)} - i\,\zeta_s^{(n)})}{\zeta_0^n}\left|\,\zeta_0\,\right|^{n-1} \end{aligned}\right\} \tag{3.23}$$

where the steady-wave component has been normalized with $U^2/2g = 1/2\,K_0$ and the unsteady-wave component normalized with ζ_a. In the present study, we used up to the 5th harmonic

component ($N = 5$) and the coefficients c_n ($n = 0 \sim 5$) for each ship-side wave were saved for subsequent use.

The same transformation must be implemented to all harmonic oscillatory quantities such as wave-induced ship motions and hydrodynamic pressures on the ship hull; thereby we can synchronize all the data, even if the measurement had been carried out at different times.

3.4 Analysis of Pressure

In the experiment measuring the pressure, the static pressure when the ship does not move in still water was taken as the zero base. Thus the time histories of measured pressure fluctuate around zero. However, the data obtained by pressure sensors affixed around the still waterline must be of rectified pulse-type signals, because the sensor positions repeat coming out and plunging into water. The possible physical reason for the non-zero value of pressure time histories when the pressure is in air might be attributed to the remaining water layers on the FBG sensor surface once the sensors coming out of water.

Typical examples of the pressure time history are shown in Fig. 3.6, which were obtained from the measurement with FBG sensors at the transverse section of ordinate number 9.5 and at 4 different locations along the girth, i. e. $\theta = 30$, 60, 90, and 93 degs from the lowest figure (where θ is the polar angle with $\theta = 0$ taken at the bottom center and $\theta = 90$ the still waterline). We note here that the hydrostatic pressure is set as the zero base in this measurement of the pressure. We can see that the time histories at $\theta = 90$ and 93 degs show half-rectified pulse-type variation

FIGURE 3.6: Examples of the time history of measured pressure in motion-free condition

because the location of the pressure sensor is repeatedly coming out of water and plunging into water. However, looking at closely these nonlinear time histories, it can be seen that the pressure is not exactly zero when the sensor is obviously in air (e. g. in the case of $\theta = 93$ deg shown in the uppermost figure). These data must be analyzed and modified if necessary, with the information of ship-side wave.

The procedure for rectifying physically unreasonable time histories of the pressure is as follows. (1) In order to decide the time instant and duration for the analysis, the trigger signal will be searched in the time record. This is because the Fourier analysis for all the measured quantities has been made with the trigger signal used as a reference time instant every time, so that we can use the time record measured at the same location in the towing tank for every measurement. Then the time duration for the analysis was decided to be $\pm T$ (encounter wave period) from the trigger signal. (2) From the incident-wave record, the origin of the time history will be adjusted as explained with regard to Eqs. (3.22) and (3.23), and thereby synchronized with the record of the ship-side wave. (3) The time instant when the ship-side wave intersects the position of the pressure sensor in question will be searched, so that the time instant and duration when the sensor is in air can be determined. If the measured value of the pressure is nonzero during that time span, the value at intersecting time will be set equal to zero and at the same time the profile of measured pressure will be shifted to satisfy the physical condition that the pressure is exactly zero when the sensor is in air.

Once the time history of the pressure has been rectified, the Fourier-series analysis incorporating higher-order terms will be made for the pressure time histories, as will be explained later. For that analysis, however, the constituents of the total pressure should be correctly understood, which can be made as explained in what follows. The total pressure $P(\boldsymbol{x}, t)$ at a certain sensor can be written, with the atmospheric pressure taken as the base, in the form

$$P(\boldsymbol{x}, t) = -\rho\, g\, z + p(\boldsymbol{x}, t) \tag{3.24}$$

The first term on the right-hand side is the hydrostatic pressure, and the second term is the steady and unsteady hydrodynamic pressures to be measured in the experiment.

When the amplitude of ship motions is small, the relationship between the inertial coordinate system $\boldsymbol{x}$ moving at constant speed of a ship (which is called the space-fixed coordinate system) and the body-fixed coordinate system $\overline{\boldsymbol{x}}$ is given as

$$\boldsymbol{x} = \overline{\boldsymbol{x}} + \boldsymbol{\alpha}_{Ts} + \boldsymbol{\alpha}_T(t) + \left[\, \boldsymbol{\alpha}_{Rs} + \boldsymbol{\alpha}_R(t)\right] \times \overline{\boldsymbol{x}} \tag{3.25}$$

$$\left.\begin{aligned} \boldsymbol{\alpha}_{Ts} = (0, 0, \xi_{3s}) \;\; \boldsymbol{\alpha}_{Rs} = (0, \xi_{5s}, 0) \\ \boldsymbol{\alpha}_T(t) = (\xi_1(t), 0, \xi_3(t)\,) \;\; \boldsymbol{\alpha}_R(t) = (0, \xi_5(t), 0) \end{aligned}\right\} \tag{3.26}$$

where $\boldsymbol{\alpha}_T$ and $\boldsymbol{\alpha}_R$ denote the translational and rotational motion vectors, respectively, and these are given in head waves as shown above. Suffix s implies the steady components.

Substituting the z-component of Eq. (3.25) into Eq. (3.24), it follows that

$$P(\boldsymbol{x},t) = -\rho g\bar{z} - \rho g(\,\xi_{3s} - \bar{x}\,\xi_{5s}\,) - \rho g\{\xi_3(t) - \bar{x}\,\xi_5(t)\} + p(\boldsymbol{x},t) \tag{3.27}$$

Since the value of $-\rho g\bar{z}$ is taken as the zero base in the actual measurement, the pressure on the right-hand side of Eq. (3.27) except for $-\rho g\bar{z}$ is the measured pressure at sensor positions on the ship hull; let this measured pressure be denoted as $p_M(\overline{\boldsymbol{x}},t)$. Then the total pressure can be retrieved from the following relation:

$$p_T(\overline{\boldsymbol{x}},t) = \begin{cases} p_M(\overline{\boldsymbol{x}},t) & \text{for } \bar{z} > 0 \\ p_M(\overline{\boldsymbol{x}},t) - \rho g\bar{z} & \text{for } \bar{z} < 0 \end{cases} \tag{3.28}$$

The total pressure thus obtained was expanded with the Fourier series as follows:

$$\begin{aligned} p_T(\overline{\boldsymbol{x}},t) &= p^{(0)}(\overline{\boldsymbol{x}}) + \sum_{n=1}^{N} \mathrm{Re}\left[\,\{p_c^{(n)}(\overline{\boldsymbol{x}}) - i\,p_s^{(n)}(\overline{\boldsymbol{x}})\}e^{in\omega_e t}\,\right] \\ &\equiv p^{(0)}(\overline{\boldsymbol{x}}) + p_u(\overline{\boldsymbol{x}},t) \end{aligned} \tag{3.29}$$

where $p_u(\overline{\boldsymbol{x}},t)$ is meant to denote only the time-variant term, and it is found that $N = 10$ is sufficient to represent even highly nonlinear rectified pulse-type signals. This time-variant unsteady pressure $p_u(\overline{\boldsymbol{x}},t)$ will be used to compute the wave loads in the next section.

However, we note that the unsteady pressure obtained above is just the value only at the location of the pressure sensor. In order to compute the unsteady pressure at any point on the ship-hull surface (which will be needed in the pressure integration), we will have to use a spline interpolation in terms of the values at sensor positions. The interpolation has been done firstly along the girth (θ direction) at each transverse section where the measurement was made. The number of interpolation points along the girth is 40 points (in symmetrical). Then in terms of the values along the girth, the secondary interpolation was made in the longitudinal direction. The number of interpolation points in the longitudinal direction is 120 points. Convergence of the results was confirmed by computing integrated forces with increasing the number of panels on the ship hull.

Chapter 4

Vertical Bending Moment

In Chapter 4, describes the formulation of vertical bending moment. The following explains the discretization procedures and the interval of integration. The last part presents the weight distribution used in the present study under the assumption of uniform structural density.

4.1 Vertical Bending Moment

The wave loads normally refer to the shear force and bending moment, but in this paper, attention is focused on the vertical bending moment (VBM hereinafter). There are two components in VBM owing to the integration of unsteady pressure and the inertia force [48]. These are time-variant and basically nonlinear, thus the VBM acting on the transverse section at $x = x_0$ in the ship's longitudinal direction may be computed from

$$M_v(x_0,t) = \int_{x_A}^{x_0} dx \int_{C_H(x)} p_u(\overline{\boldsymbol{x}},t)\, n_5(\boldsymbol{x},t)\, d\ell - \int_{x_A}^{x_0} \frac{w(x)}{g}(x-x_0)\Big\{\ddot{\xi}_3(t) - (x-\ell_x)\,\ddot{\xi}_5(t)\Big\}\, dx \tag{4.1}$$

where

$$n_5(\boldsymbol{x},t) = (z-\ell_z)\, n_1(\boldsymbol{x},t) - (x-x_0)\, n_3(\boldsymbol{x},t) \tag{4.2}$$

is the extended normal vector for computing the VBM at $x = x_0$, and the hogging moment is defined to be positive in Eq. (4.1). The origin of the coordinates in Eq. (4.1) is shifted to the center of gravity, denoted as $(\ell_x, 0, \ell_z)$. The x- and z-components of the normal vector, $n_1(\boldsymbol{x},t)$ and $n_3(\boldsymbol{x},t)$, are expressed in the space-fixed coordinate system, which are changing in time due to wave-induced ship motions, although the corresponding terms in the body-fixed coordinate system, denotes as $\tilde{n}_1(\overline{\boldsymbol{x}})$ and $\tilde{n}_3(\overline{\boldsymbol{x}})$, are time-invariant. The relationship between these terms is

given as follows:

$$\left\{ \begin{array}{c} n_1(\boldsymbol{x},t) \\ n_3(\boldsymbol{x},t) \end{array} \right\} = \left[\begin{array}{cc} \cos\xi_5(t) & \sin\xi_5(t) \\ -\sin\xi_5(t) & \cos\xi_5(t) \end{array} \right] \left\{ \begin{array}{c} \tilde{n}_1(\overline{\boldsymbol{x}}) \\ \tilde{n}_3(\overline{\boldsymbol{x}}) \end{array} \right\} \tag{4.3}$$

where $\xi_5(t)$ is the wave-induced pitch motion of a ship. The lower limit x_A in the integral with respect to x in Eq. (4.1) is the longitudinal position of aft end of a ship and $C_H(x)$ the contour of transverse section at station x.

We note that the wetted surface of ship hull can be computed with a spline interpolation from the information of ship-side wave given by Eq. (3.23) and the unsteady pressure $p_u(\overline{\boldsymbol{x}},t)$ from Eq. (3.29) at each time step; both of these are given in the body-fixed coordinate system. Furthermore, as shown by Eq. (4.3), the normal-vector components in the space-fixed coordinate system can be computed from the information of body-fixed coordinates. In the present case, the unsteady pressure $p_u(\overline{\boldsymbol{x}},t)$ includes nonlinear components as indicated by Eq. (3.29), but in the linear problem consisting of only the first-harmonic components, the unsteady pressure may be given as a linear superposition of the diffraction pressure p_D, the radiation pressure p_R, and the variation of hydrostatic pressure p_S; which is the case in the linear potential-flow theory like RPM.

The second line in Eq. (4.1) indicates the inertia-force term, where $\ddot{\xi}_3(t)$ and $\ddot{\xi}_5(t)$ are the acceleration in heave and pitch, respectively, and $w(x)$ is the weight-distribution function related to the ship's mass m and the gyrational radius in pitch κ_{yy} as follows:

$$\int_{x_A}^{x_F} \frac{w(x)}{g}\,dx = m, \quad \int_{x_A}^{x_F} \frac{w(x)}{g}\,x\,dx = m\,\ell_x, \quad \int_{x_A}^{x_F} \frac{w(x)}{g}(x-\ell_x)^2\,dx = m\,\kappa_{yy}^2 \tag{4.4}$$

where x_F in the upper limit of integration range denotes the fore end of a ship.

Normally the weight distribution should be provided as input data in actual problems. However, in the present study, since the weight distribution was not measured and unknown, the VBM due to the inertia force is computed under the assumption of uniform structural density without point load; that is, the sectional weight distribution is assumed to equal to the sectional distribution of volume displacement (sectional buoyancy) as depicted in Fig.4.1.

Fig.4.1 presents the volume of the immersed portion from each transverse section throughout the ship's length which is the Bonjean curve. The volume distribution in terms of Bonjean curve represents the function of volume distribution at each transverse section over the ship draft. The number of spline interpolation points of the volume distribution is the same as the interpolation to be made in the interpolation of pressure, that is 40 points (in symmetric) at the girth direction and 120 points in the longitudinal direction. With respect to the discretized values of the volume distribution over the ship draft as well as the discretized values of forces, hence we can obtain

the vertical bending moment distribution at each transverse section (in z-direction) over the ship length from Eq. 4.1.

Considering the degree of wave-induced ship motion however, the volume of the immersed portion is distinguished between the linear and non-linear response which corresponding to the mean values of the time instant wetted surface of the steady and unsteady pressure acting on the ship hull.

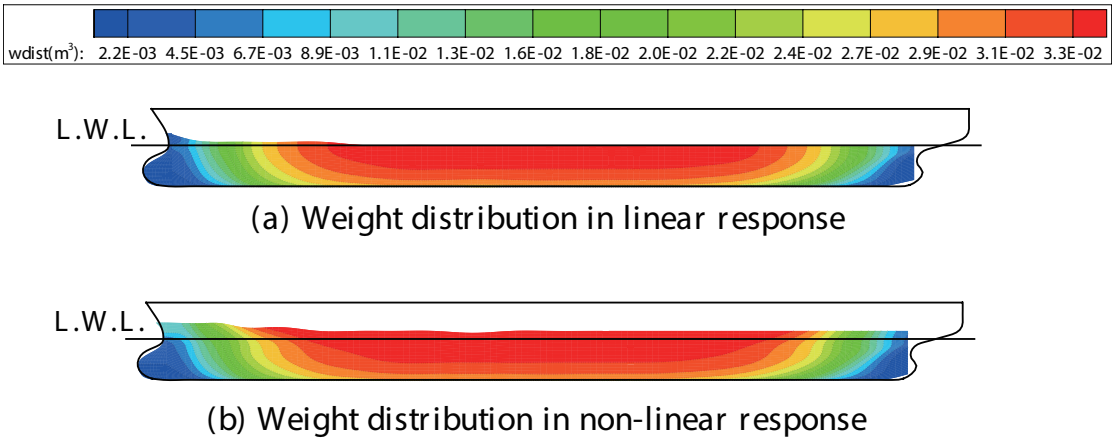

FIGURE 4.1: Weight distribution in terms of uniform structural density, (a) For linear response, (b) For non-linear response

In calculating the VBM according to Eq. (4.1), the integrated result up to $x_0 = x_F$ must be consistent to the equations of coupled motion equations in surge, heave, and pitch. Namely the integrated value of Eq. (4.1) up to $x_0 = x_F$ must be equal to zero. In order to ensure this condition of zero VBM at the fore end of a ship and the correct computation of VBM in the time domain, the origin in time histories (i.e. the phase with respect to an incident wave) of all harmonic oscillatory quantities, particularly both unsteady pressure and ship motions, must be synchronized as explained in Chapter 3 Section 3.3.

Chapter 5

Results and Discussion

Chapter 5 presents the results of experiments and their comparisons with the computations. First, the measured ship-side wave is presented and the shifting coefficient for each ship-side wave is obtained. Afterward, the same transformation is applied to synchronize the time histories of other quantities such as wave-induced ship motions and hydrodynamic pressure on the ship hull in the subsequent analysis. After that, the validation of measured unsteady pressure distribution is presented. Then, the vertical bending moment at zero-and forward-speed in head waves is discussed. Some comparisons and discussion of experiments with the computation methods by the linear potential flow theory and nonlinear CFD are made as well as the features of linear and nonlinear responses. An important comparison is then made for the vertical bending moment measured directly at a specified transverse section by a segmented ship model for a wide range of wavelengths. Eventually, the analysis method is further validated through comparison with the benchmark data of a 6750-TEU container ship which used segmented hulls.

5.1 Ship-side Wave

The ship-side wave experiment was conducted for the case of a ship with forward-speed. Since the degree of nonlinearity on the ship motions and wetted hull surface emerges, hence accurate tracing of those time instants is crucial in the synchronizing of the data.

The result of the ship-side wave is presented in Fig. 5.1 for the case of resonant frequency at $Fn = 0.18$, $\lambda/L = 1.25$ in head wave. Red and white color symbols in the upper graph denote the first-harmonic component in Fourier series, the middle graph is the second-harmonic component, and white symbol in the lower graph shows the steady-wave component. The plots are shown in nondimensional value with ζ/ζ_a and the incident wave is however still in the framework of linear theory, $\zeta_a = 0.0240m$. More results regarding the ship-side wave in different wavelengths can be seen in the Appendices A.

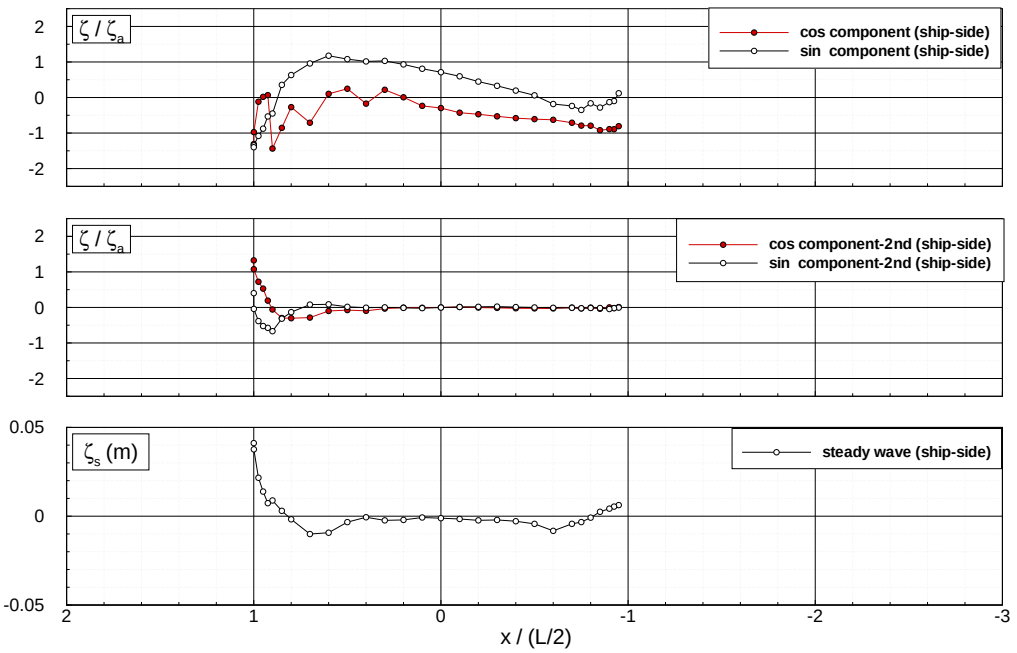

FIGURE 5.1: Wave profile measured along ship-side of RIOS bulk carrier at $Fn = 0.18$, $\lambda/L = 1.25$ in head wave. Values are shown with ζ/ζ_a and $\zeta_a = 0.0240$ m.

These Fourier series components describe the ship-side wave record at an arbitrary point $\zeta(t)$ as presented in Chapter 3, Eq. 3.21 which have been synchronized with the crest of incident wave measured at the origin of the coordinate system. With the obtained shifting coefficient $c_n(n = 0 \sim 5)$ for each ship-side wave at the time instant of wetted hull surface, then the same transformation is implemented to synchronized the time histories of other quantities such as wave-induced ship motion and hydrodynamic pressures on the ship hull.

5.2 Validation of Unsteady Pressure Distribution

Comparison of the spatial distribution of first-harmonic pressure has been done by Iwashita *et al.* [39, 40, 42, 43] and Kashiwagi *et al.* [1, 41] along the girth at some transverse sections between the results measured in the motion-free case in head waves and computed with some methods based on the linear potential-flow theory in the frequency domain, through which repeatability and reliability of the experimental data has been confirmed.

As another validation of measured results, we have computed the first-harmonic wave-exciting forces from the integration of unsteady pressure distribution measured for the diffraction problem and compared the result with the corresponding forces measured directly with dynamometer. The results are shown in Fig. 5.2, where the values obtained by the integration of measured unsteady diffraction pressure are indicated with black circle symbol and the values directly measured with dynamometer are indicated with white circle and gray diamond symbols (which are

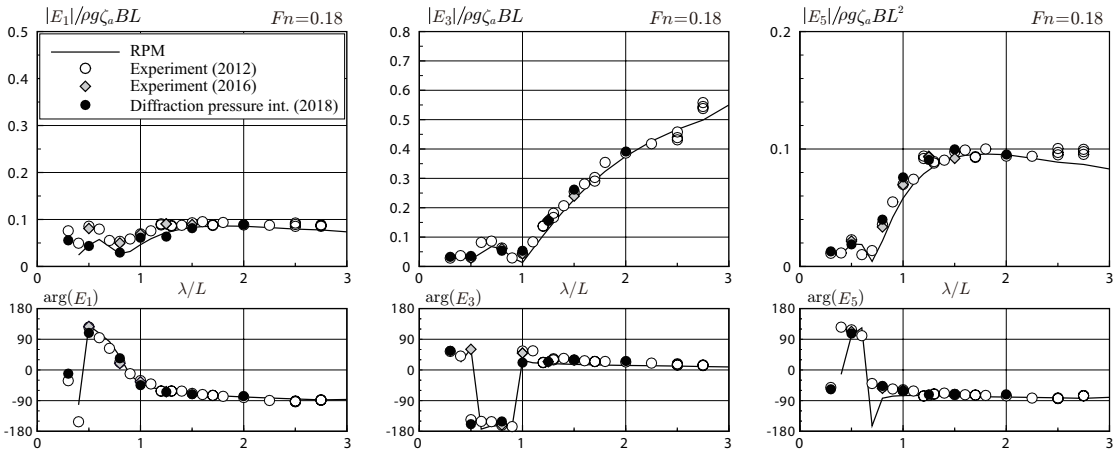

FIGURE 5.2: Validation of pressure integration on the hull surface of RIOS bulk carrier in diffraction problem: comparison with the values measured directly by dynamometer at $Fn = 0.18$ in head waves

TABLE 5.1: The results and relative errors of experiments between pressure integration and force measured with dynamometer

λ/L	$\lvert E_1\rvert/\rho g\zeta_a BL$			$\lvert E_3\rvert/\rho g\zeta_a BL$			$\lvert E_5\rvert/\rho g\zeta_a BL^2$		
	$\overline{Exp}$	DPI	E (%)	$\overline{Exp}$	DPI	E(%)	$\overline{Exp}$	DPI	E(%)
0.8	0.051	0.030	−41.18	0.064	0.054	−15.63	0.034	0.040	17.65
1	0.069	0.061	−11.59	0.044	0.054	22.73	0.070	0.076	11.43
1.25	0.090	0.064	−28.49	0.160	0.156	−2.50	0.093	0.091	−2.15
1.5	0.091	0.082	−9.89	0.247	0.262	6.07	0.095	0.100	5.26
2	0.087	0.091	4.60	0.381	0.392	3.02	0.095	0.095	0.53

the results in the experiments conducted in 2012 and 2016, respectively). Computed results by the RPM of the forward-speed version are provided with solid line for comparison.

Overall, good agreement can be observed in figures. In order to quantify the errors, Table 5.1 presents the relative errors between the results by the direct measurement and pressure integration at the range of wavelength $0.8 < \lambda/L < 2.0$. In this table, the values of direct measurement denoted as $\overline{Exp}$ are the average of the experiments in 2012 and 2016 and the results of diffraction pressure integration are indicated as DPI. The relative error is computed from $(DPI - \overline{Exp})/\overline{Exp}$. We note that the wave-exciting forces at shorter wavelengths are relatively small and slight discrepancy between the two small values provides a large value in the error percentage. For instance, at $\lambda/L = 1.0$ the largest relative error occurs in the heave exciting force with 22.73 % error, but the value itself is very small and thus this difference is not conspicuous in the figure. Looking at Table 5.1 with this fact kept in mind, we can see fairly good agreement for the heave force and pitch moment at all wavelengths, which indicates reliability of the unsteady pressure measured with FBG pressure sensors. We note however that there exist

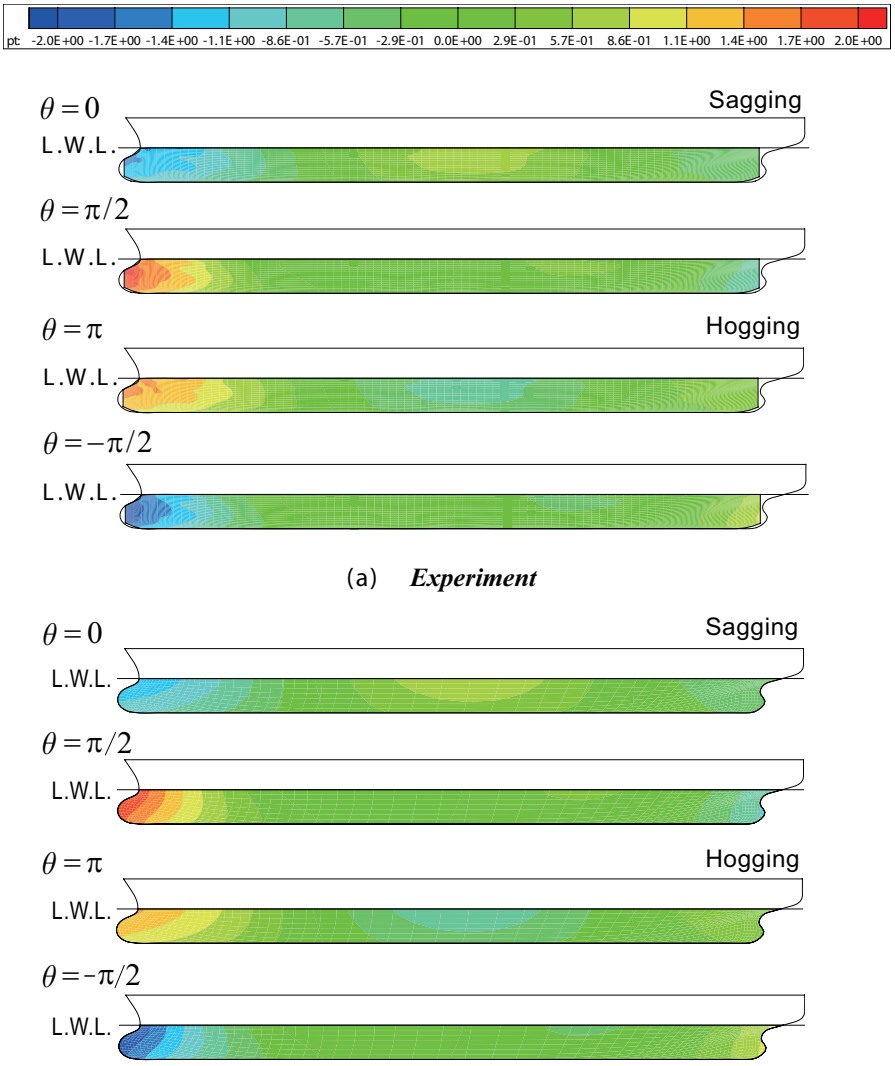

FIGURE 5.3: Unsteady pressure distribution at $\lambda/L = 1.0$ and $Fn = 0.0$ in head wave; (a) Experiment, (b) Computation by RPM. Values are shown with $p/\rho g\zeta_a$ and $\zeta_a = 0.0106$ m.

slight discrepancies in the surge exciting force at some shorter wavelengths, typically prominent underestimation with 41.18% error at $\lambda/L = 0.8$. This order of error is visible even in the figure. A possible reason of this difference may be attributed to the scarcity of FBG pressure sensors in the bow upper region above the still waterline, because the pressure on that region contributes to the surge force. On the other hand, the dominant pressures for the heave and pitch forces act on the bottom of a ship because of the direction of normal vector and the pressures near or above still waterline contribute little especially for a wall-sided ship.

As another demonstration of the results, a side view of the spatial distribution of unsteady pressure is shown in Fig. 5.3 for the case of $\lambda/L = 1.0$ in head wave and $Fn = 0.0$, where the pressure is shown in the nondimensional form of $p/\rho g\zeta_a$ and $\zeta_a = 0.0106$ m in accordance with the experiment in this particular example. Note that the color scale in the contour display is

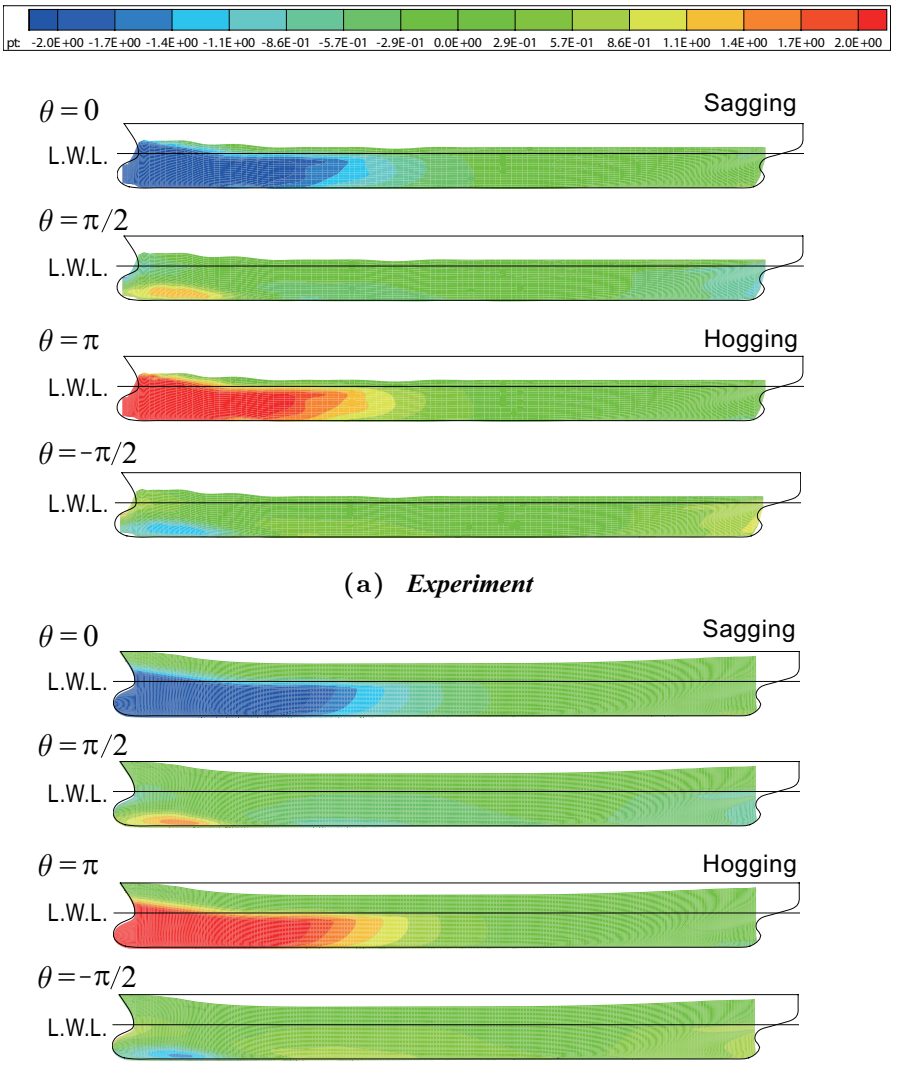

FIGURE 5.4: Unsteady pressure distribution at $\lambda/L = 1.25$ and $Fn = 0.18$ in head wave; (a) Experiment, (b) Computation by CFD. Values are shown with $p/\rho g\zeta_a$ and $\zeta_a = 0.0240$ m.

taken from −2.0 to +2.0, and that the phase of variation θ is taken such that $\theta = 0$ corresponds to the time instant of maximum sagging moment. Overall, favorable agreement can be seen between experimental data and computed results by the linear RPM explained in Subsection 3.1, although we can see slight discrepancy in the magnitude at the bow region particularly at time instants of $\theta = 0$ and $\theta = \pi$. Namely the phase in the pressure variation looks a little different between the experiment and the computation by RPM in this paper, but it is confirmed by Iwashita *et al.* [43] using the free-surface Green-function method that the amplitude of the first harmonic component in the unsteady pressure at $Fn = 0.0$ agrees well along the girth at each of the transverse sections where the measurement was conducted. More parametric results regarding the unsteady pressure at zero-speed in different wavelengths can be seen in the Appendices B.

Likewise, a side view of the unsteady pressure distribution at $\lambda/L = 1.25$ in head wave and $Fn = 0.18$ is shown in Fig. 5.4 in the nondimensional form of $p/\rho g\zeta_a$ with $\zeta_a = 0.0240$ m, where a comparison is made between experiment and nonlinear computation by CFD using FINE/Marine. It should be noted that the maximum nondimensional value of unsteady pressure becomes a little larger than 4.0 near the bow and free surface in this particular case, but the color scale in the contour display is kept the same as that in Fig. 5.3 to see the relative magnitude and to show overall good agreement even for the forward-speed case. We also note that $\lambda/L = 1.25$ is close to the resonant frequency in ship motions at $Fn = 0.18$ (as will be shown later) and the degree of agreement for this unsteady pressure distribution was not so good when compared to computed results by the forward-speed version of RPM [43], which may be due to large ship motions and hence strong nonlinear effects. More parametric results regarding the unsteady pressure at zero-speed and forward-speed in different wavelengths can be seen in the Appendices B.

5.3 Vertical Bending Moment at Zero Speed

We start with an easier case, i.e. at zero forward speed ($Fn = 0.0$) in head waves. Since the wave steepness H/λ (the ratio of wave height H with wavelength λ) in the experiment was set to about 1/50, measured phenomena must be in the framework of linear theory. Therefore the linear potential theory, typically RPM, can be used for the numerical computation. For computing the VBM from Eq. (4.1), the motion RAOs are necessary, the results of which are presented in Fig. 5.5 for surge, heave, and pitch motions, and good agreement can be seen between measured and computed results (the results shown with white and black circle symbols were obtained by the experiments conducted in 2015 and 2016, respectively).

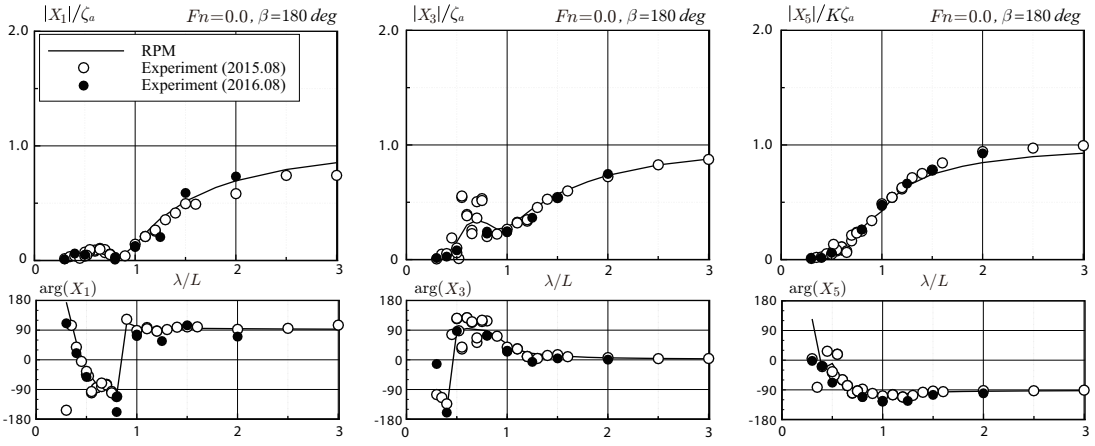

FIGURE 5.5: Surge, heave, and pitch RAOs of RIOS bulk carrier at $Fn = 0.0$ in head waves

We have already confirmed in Fig. 5.3 that the unsteady pressure distribution at $Fn = 0.0$ was also in good agreement between measured and computed results. Thus we can expect good

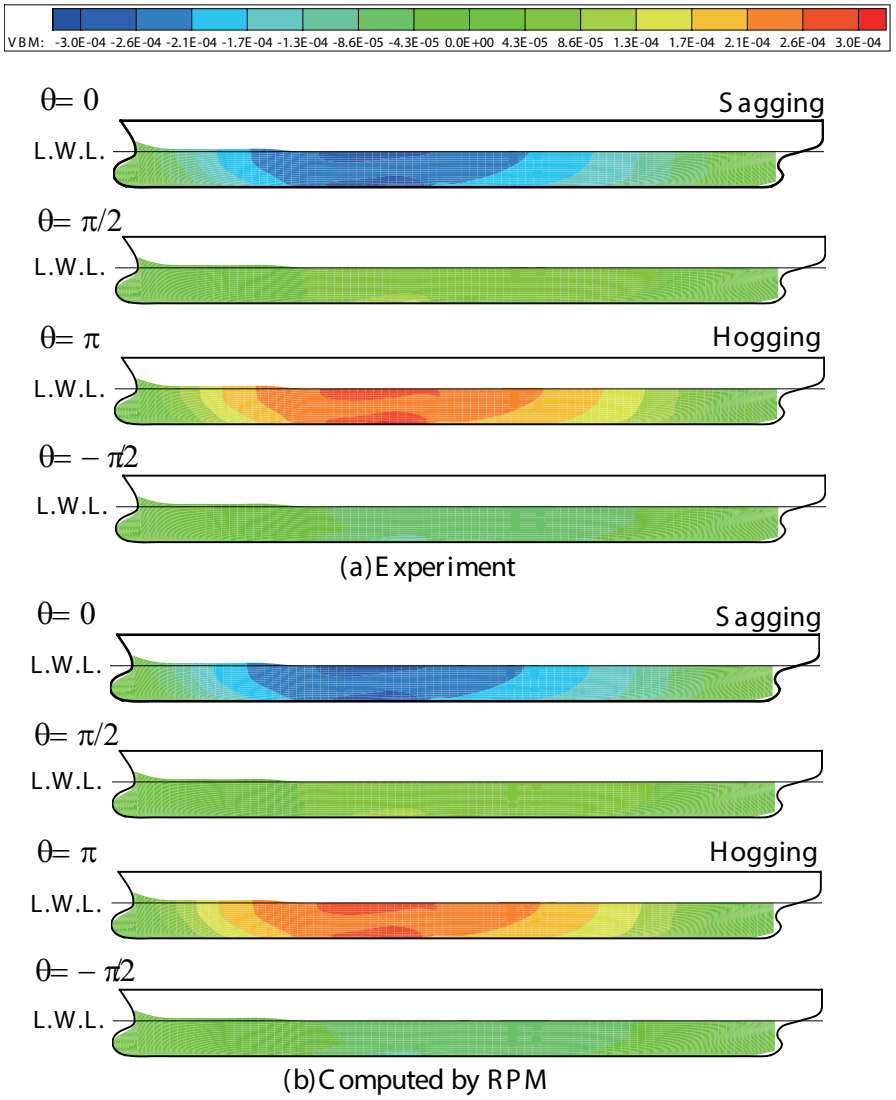

FIGURE 5.6: VBM distribution at $\lambda/L = 1.00$ of head wave and $Fn = 0.00$; (a) Experiment, (b) Computation by CFD

agreement in the VBM as well. In fact, the VBM was evaluated from Eq. (4.1) using only the measured data and also only the computed values by RPM. The integrand function of the VBM for the hydrodynamic term presented in the first part of Eq. (4.1) can be obtained by integrating throughout the ship's length the pressure distribution and normal vector $n_5(\boldsymbol{x}, t)$ as defined in Eq. (4.2). For the inertia term of VBM, the weight distribution as a volume distribution is initially treated according to the Bonjean curve data of the ship model distributed along the girth at each transverse section. Afterward, the inertia term of VBM obtained by integrating the weight distribution and the vertical ship motion acceleration throughout the ship's length. Then, the sum of these two terms which integrated along x up to an arbitrary length of $x = x_0$, the spatial VBM distribution can be plotted as presented in Fig. C.2 for the case of $\lambda/L = 1.00$ and $Fn = 0.0$ in a nondimensional form divided by $\rho g \zeta_a L^2$. The color scale in the contour display is set from $-3.0E-4$ to $+3.0E-4$, with the number of mesh of 40 and 80 at vertical

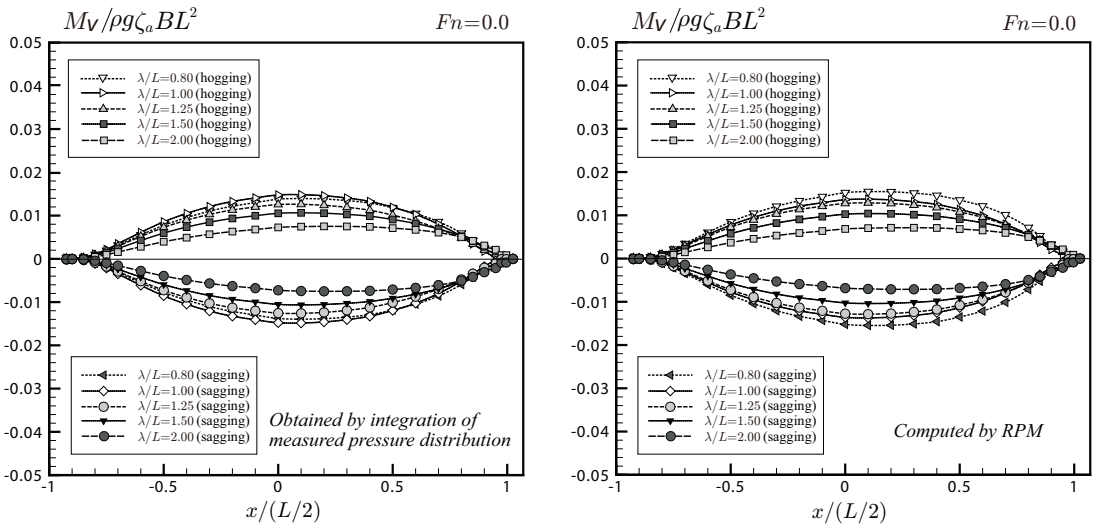

FIGURE 5.7: Longitudinal distribution of vertical bending moment (VBM) on RIOS bulk carrier at $Fn = 0.0$ in head waves. Left: integration of measured pressure distribution, Right: computed by RPM.

and longitudinal, respectively. Overall, good agreement can be seen in this VBM distribution. More results regarding the VBM distribution in different wavelengths at zero-speed can be seen in Appendices C. After integrating the VBM distribution then a comparison of the longitudinal distribution of VBM is shown in Fig. 5.7 accordingly at wavelengths of $\lambda/L = 0.8$, 1.0, 1.25, 1.5, and 2.0 for the maximum values in the hogging (plus) and sagging (minus) moments.

As we might expect, a ship with zero forward speed exhibits the linear responses in ship motions, wetted hull surface, and also the pressure distribution which eventually resulting in the linear response of symmetrical hogging and sagging. Moreover, the results indicate very good agreement can be confirmed for the sectional values of VBM between the values evaluated with experimental data and computed with RPM; which proves that the unsteady pressure distribution on the ship-hull surface has been successfully measured and the procedure for the data analysis and evaluation of VBM is consistent.

5.4 Vertical Bending Moment at Forward Speed

Next comparison is for the case of forward speed of $Fn = 0.18$, in which nonlinearity in the VBM must be observed especially when the ship motions are resonant around $\lambda/L = 1.25$; that is, as pointed out by some scholars [15–18], the magnitude in the sagging moment may be larger than that in the hogging moment, although the wave steepness is the same as that at $Fn = 0.0$. To see visually the degree of nonlinearity at $\lambda/L = 1.25$, two snapshots for the wave profile at sagging and hogging conditions in the experiment are shown in Fig.5.8. Since the degree

of nonlinearity looks conspicuous from these snapshots, numerical computations at $Fn = 0.18$ were implemented using CFD software, FINE/Marine V 8.2.

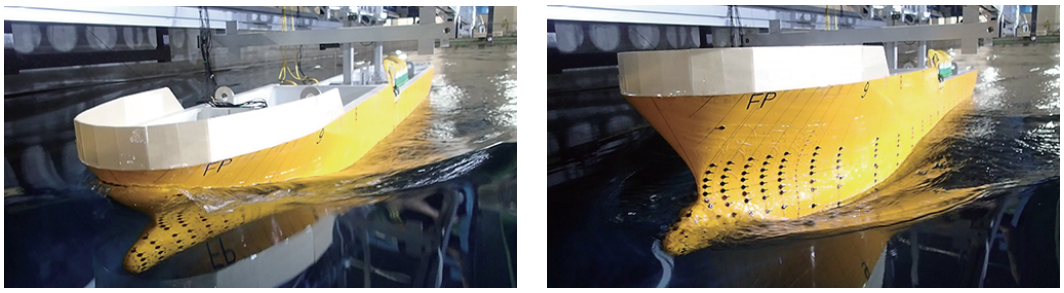

FIGURE 5.8: Snap shots of wave profile at $\lambda/L = 1.25$ of head wave and $Fn = 0.18$. Left: sagging, Right: hogging

As a preliminary check for computing the VBM, the motion RAOs are computed by CFD and compared with measured values (the experiments plotted with white and black circles were conducted in September 2017 and 2018, respectively). In CFD computations, the amplitude of ship motion was taken equal to half of the peak-to-peak mean value in the computed time histories. Obtained results are shown in Fig. 5.9 at 6 wavelengths in the range of $\lambda/L = 0.5 \sim 2.0$ for comparison. However, CFD results under $\lambda/L = 0.5$ are not presented because of large computation time due to necessity of increasing the number of meshes and time steps for obtaining converged results in short wave simulation. It should be noticed that the surge is fixed in the CFD computation whereas it was free in the experiment. The pitch is naturally coupled with surge even for a longitudinally symmetric body at zero speed. Thus there must be a difference in the physical situation between computation and experiment in the present comparison; which may affect particularly the pitch-motion results, although at forward speed the heave would also be affected by surge through the coupling among surge, heave, and picth motions.

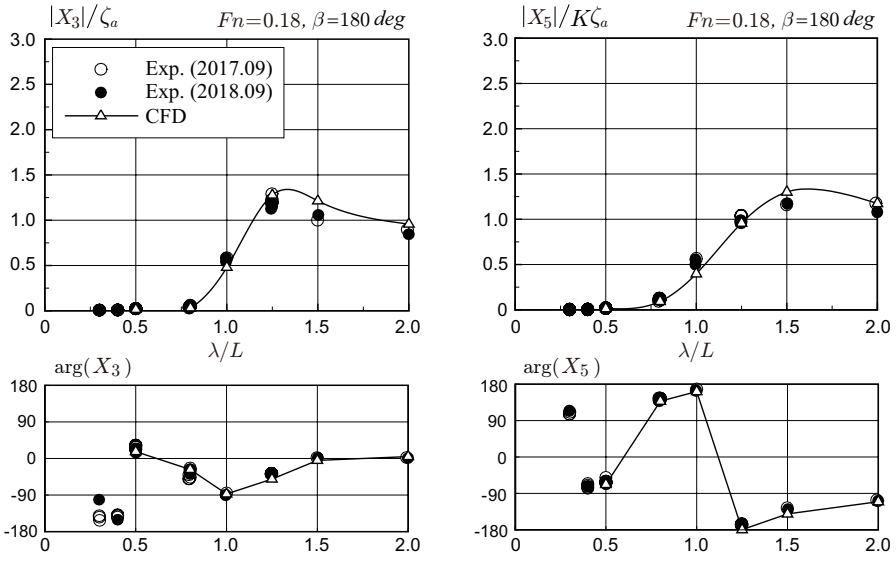

FIGURE 5.9: Heave and picth RAOs of RIOS bulk carrier at $Fn = 0.18$ in head waves

Table 5.2 shows the values in digits and the relative standard deviation (SD) representing the uncertainty of the experiment conducted in 2017 and 2018. The repeatability can be seen with relatively small deviation particularly in heave at $\lambda/L = 1.25$ and in pitch at $\lambda/L = 1.5$ with 0.18% and 0.73%, respectively. It is noted that the heave motion becomes resonant around $\lambda/L = 1.25$ at $Fn = 0.18$. Comparing the CFD results with the average value of the experiment, a good agreement can be seen at heave-resonant $\lambda/L = 1.25$ only with 7.80% overestimation and 4.01% underestimation for heave and pitch, respectively, although the surge is fixed in the CFD computations. We can conclude from these comparisons that overall computed results by CFD are in good agreement with measured values, despite slight discrepancies at some other wavelengths.

The spatial distribution of unsteady pressure at $\lambda/L = 1.25$ and $Fn = 0.18$ was already compared in Fig. 5.4, as a validation of the measured results. Even in this motion-resonant nonlinear condition, we could see favorable agreement in the pressure distribution on almost the whole ship-hull surface.

We also note that, in the forward-speed case, the steady hydrodynamic pressure due to forward translation of a ship, $p^{(0)}(\overline{x})$, as obtained from the expanded Fourier series in Eq.(3.29) is incorporated however in the VBM computation in terms of satisfying the steady-state equilibrium condition. Fig. 5.10 depicts the comparison of steady hydrodynamic pressure of the experiment and computed by CFD from the expanded Fourier series at $\lambda/L = 1.25$ and $Fn = 0.18$ in head wave. Although slight discrepancy is observed however is still within an acceptable range between the experiment and CFD.

Applying the same way as in the zero-speed case as obvious from Eq. (4.1), once the value of $n_5(\boldsymbol{x}, t)$ defined by Eq. (4.2) is multiplied by the pressure distribution, we can obtain the integrand function for the first term of VBM to be computed by the pressure integration. For the second inertia term of VBM in Eq. (4.1), the weight distribution is initially treated as the Bonjean

TABLE 5.2: The results and relative errors of heave and pitch between CFD and experiment

λ/L	$\lvert X_3\rvert/\zeta_a$					$\lvert X_5\rvert/K\zeta_a$				
	ex2017	ex2018	$SD(\%)$	CFD	$E(\%)$	ex2017	ex2018	$SD(\%)$	CFD	$E(\%)$
0.5	0.023	0.019	13.47	0.015	−28.57	0.018	0.018	0.00	0.014	−22.22
0.8	0.039	0.040	1.79	0.032	−18.99	0.097	0.097	0.00	0.093	−4.12
1	0.586	0.503	10.78	0.480	−11.85	0.565	0.501	8.49	0.398	−25.33
1.25	1.187	1.184	0.18	1.278	7.80	1.036	0.960	5.38	0.958	−4.01
1.5	1.001	1.059	3.98	1.213	17.77	1.162	1.174	0.73	1.300	11.30
2	0.897	0.845	4.22	0.957	9.87	1.176	1.080	6.02	1.174	4.08

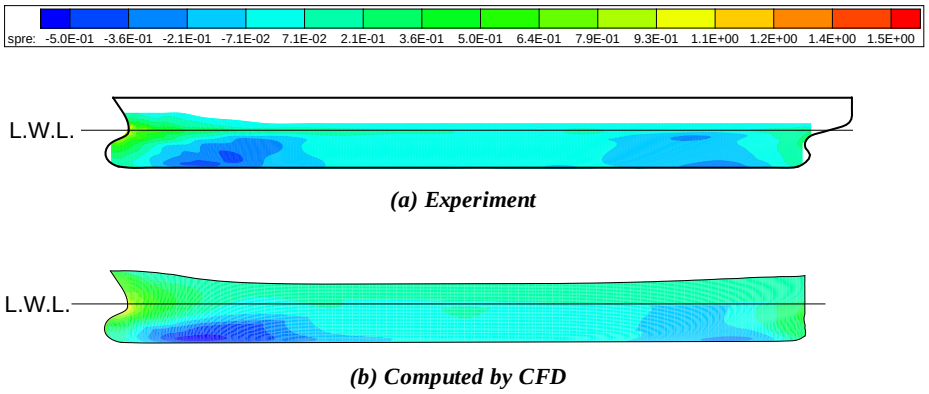

FIGURE 5.10: Steady pressure distribution at $\lambda/L = 1.25$ and $Fn = 0.18$ in head wave; (a) Experiment, (b) Computation by CFD. Values are shown with $p/(\rho U^2/2)$.

volume distribution along the girth at each transverse section. Then, once the sum of these two terms is integrated with respect to x up to a desired position $x = x_0$, we can provide the spatial distribution of VBM, which is depicted in Fig. 5.11 for the case of $\lambda/L = 1.25$ and $Fn = 0.18$ in a nondimensional form divided by $\rho g \zeta_a L^2$. Overall, good agreement can be seen also in this VBM distribution. More results regarding the VBM distribution in different wavelengths at forward-speed can be seen in Appendices C. It should be pointed out that the maximum values in both sagging and hogging moments occur at a slightly forward position from the midship.

According to Eq. (4.1), by integrating this kind of distribution of VBM along the girth direction at each transverse section in the ship's longitudinal direction, we can obtain the longitudinal distribution of VBM, as already done and shown in Fig. 5.7 for the zero-speed case. For the forward-speed case of $Fn = 0.18$, obtained results are shown in Fig. 5.12 for several wavelengths ($\lambda/L = 0.8 \sim 2.0$) of head waves. Computations are performed only with experimental data of the pressure distribution and ship motion and in the same way only with CFD. It should be noted that Fig. 5.8 are plotted for the maximum value in the hogging moment and the minimum value in the sagging moment in the time histories of the VBM generated according to Eq. (4.1).

From the comparison in Fig. 5.12, we can see the overall agreement between the experiment and CFD computation although CFD computation seems slightly overestimate for some wavelengths. For instance, at resonant frequency $\lambda/L = 1.25$ the overestimation as observed in Fig. 5.12 and obviously in Fig. 5.11 can be accounted even for the slight differences in the pressure distribution as well as ship motions.

Table 5.3 shows the values in digits and relative errors of VBM at several sections of $x/(L/2) = -0.2, 0.1, 0.4, 0.7$; which indicate relatively small difference even at around motion-resonant wavelengths, with maximum error 25%. More importantly, the asymmetric property in the VBM can be clearly observed by both experiment and CFD, with larger sagging moment for all wavelengths (although the degree of asymmetry is different depending on the wavelength),

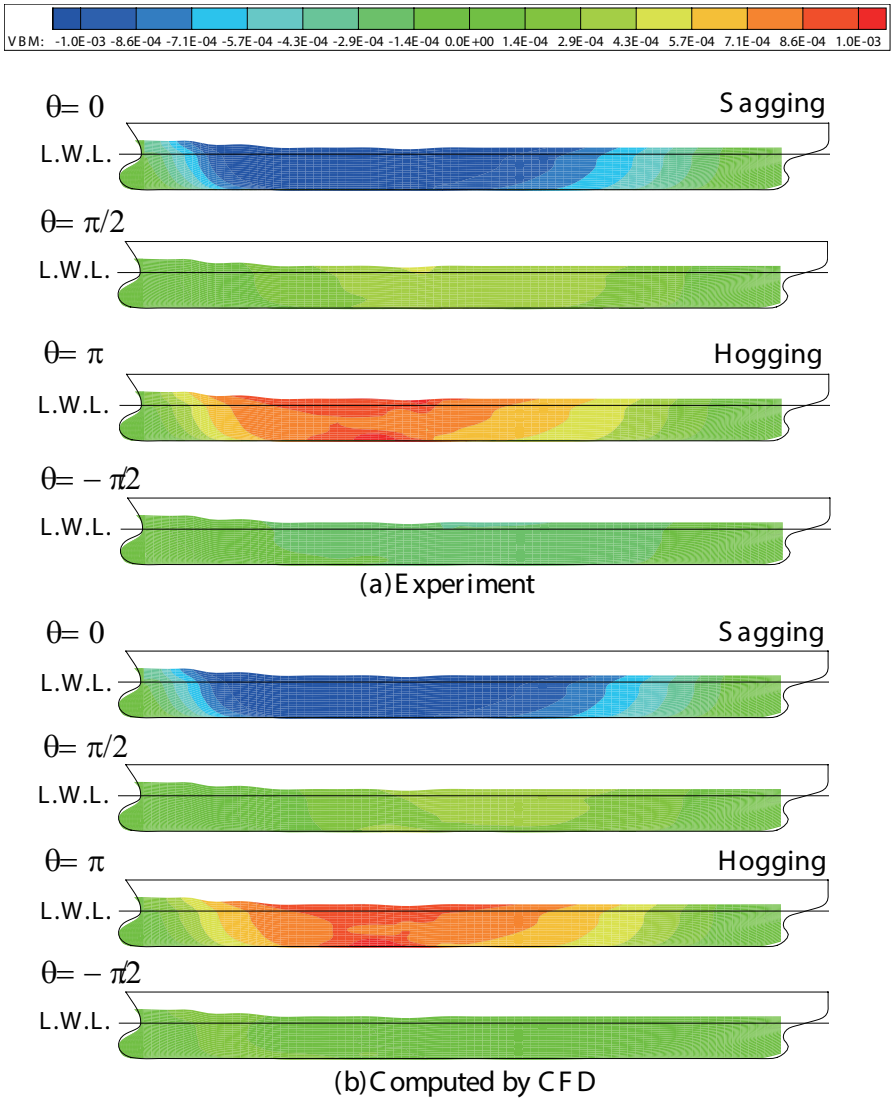

FIGURE 5.11: VBM distribution at $\lambda/L = 1.25$ of head wave and $Fn = 0.18$; (a) Experiment, (b) Computation by CFD

and the position where the cross-sectional VBM becomes maximal is shifted a little forward from the corresponding position observed at $Fn = 0.0$ (Fig. 5.7); which is anticipated also from Fig. 5.11 and must be understood as an important forward-speed effect. In fact, as shown in Fig. 5.4 for $Fn = 0.18$, the magnitude of unsteady pressure becomes very large in the bow region (particularly at resonant wavelength $\lambda/L = 1.25$) due to existence of the forward speed of a ship, and consequently the VBM tends to take maximal values at a position forward from the midship.

With respect to the Eq. 4.1, there are two components in VBM owing to the integration of unsteady pressure and the inertia force. According to it, however, the degree of contribution of each component could be presented. Fig. 5.13 shows the half peak-to-peak components of vertical bending moment (VBM) on RIOS bulk carrier obtained by the integration of measured pressure distribution at $Fn = 0.18$ in head waves. It should be noted in this particular figure the

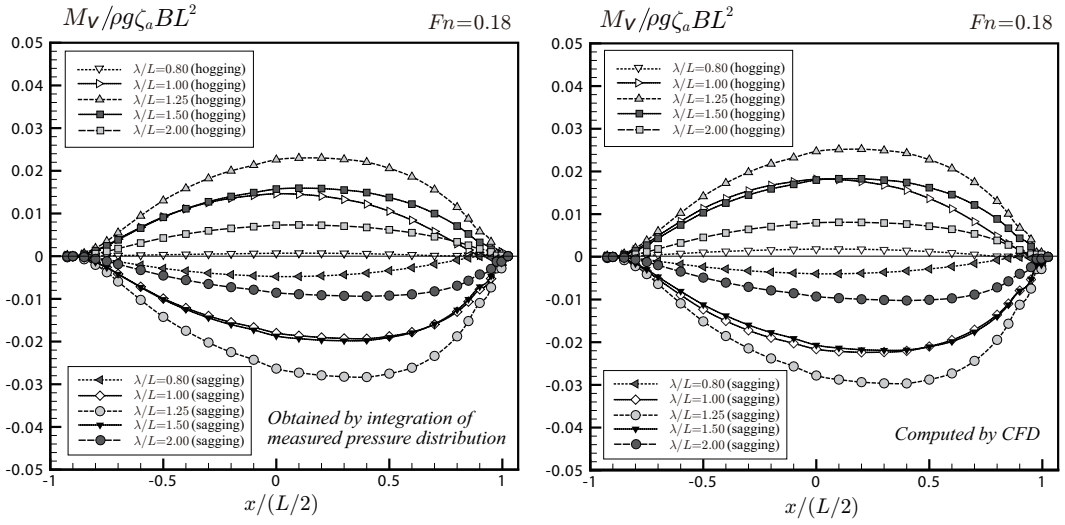

FIGURE 5.12: Longitudinal distribution of vertical bending moment (VBM) on RIOS bulk carrier at $Fn = 0.18$ in head waves. Left: integration of measured pressure distribution, Right: computed by CFD

vertical bending moment is taken as the mean value between the hogging and sagging phases. However, looking at the comparison of each component, we can understand there is a cancelation of the inertia and the pressure term. The magnitude of the inertia term seems larger than the pressure term. As the future works, it is important to conduct more parametrical studies to evaluate the dependency of the contributing component as well as the magnitude of the vertical

TABLE 5.3: The results and relative errors of VBM between CFD and experiment around motion resonant

λ/L	$x/(L/2)$	$M_V/\rho g\zeta_a BL^2$(Hogging)			$M_V/\rho g\zeta_a BL^2$(Sagging)		
		Exp	CFD	$E(\%)$	Exp	CFD	$E(\%)$
1	−0.2	0.014	0.016	14.3	−0.016	−0.019	18.8
	0.1	0.015	0.018	20.0	−0.019	−0.022	15.8
	0.4	0.012	0.015	25.0	−0.019	−0.022	15.8
	0.7	0.006	0.007	16.7	−0.016	−0.017	6.3
1.25	−0.2	0.020	0.022	10.0	−0.023	−0.024	4.3
	0.1	0.023	0.025	8.7	−0.027	−0.029	7.4
	0.4	0.022	0.024	9.1	−0.028	−0.030	7.1
	0.7	0.016	0.018	12.5	−0.023	−0.024	4.3
1.5	−0.2	0.014	0.016	14.3	−0.016	−0.018	12.5
	0.1	0.016	0.018	12.5	−0.019	−0.021	10.5
	0.4	0.015	0.017	13.3	−0.020	−0.022	10.0
	0.7	0.010	0.012	20.0	−0.016	−0.018	12.5

bending moment with the forward speed, incident wave heights, and hull shapes in conjunction with the magnitude of the inertia and pressure terms.

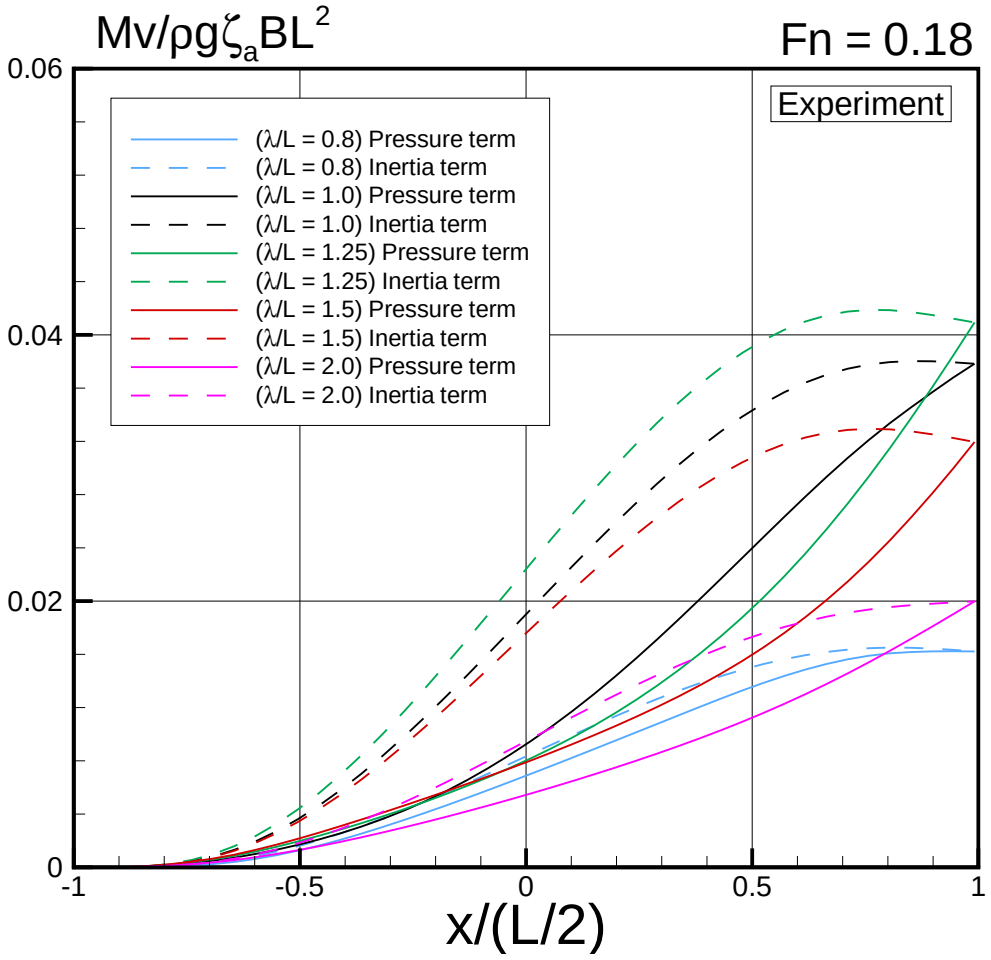

FIGURE 5.13: Half peak-to-peak components of vertical bending moment (VBM) on RIOS bulk carrier obtained by the integration of measured pressure distribution at $Fn = 0.18$ in head waves.

5.5 Validation of VBM with Benchmark Test Data

The VBM has been computed in this study by integrating the unsteady pressure distribution obtained by the experiment or computation over the ship hull and the results were compared, but this kind of comparison is essentially the same as the comparison of the spatial distribution of unsteady pressure. Thus, if possible, a comparison should be made for the VBM measured directly at a specified transverse section by a segmented ship model for a wide range of wavelength.

For that purpose, the analysis method in this paper was further validated through comparison with the benchmark data of a 6750-TEU container ship whose principal particulars are shown in

TABLE 5.4: Principal particulars of 6750-TEU container ship used for bench-mark test, Kim *et al.* [2]

Item	Prototype	Model
Scale	1/1	1/70
L_{OA} (m)	300.891	4.298
L_{BP} (m)	286.6	4.094
B (m)	40.0	0.571
d (m)	11.98	0.171
C_b	0.624	0.624
KM (m)	18.662	0.267
GM (m)	2.100	0.030
KG (m)	16.562	0.237
L_{CG} from AP (m)	138.395	1.977
κ_{xx} (m)	14.4	0.206
$\kappa_{yy}(=\kappa_{zz})$ (m)	70.144	1.002
Natural period of roll (sec)	20.5	2.450
Neutral axis from keel (m)	7.35	0.105

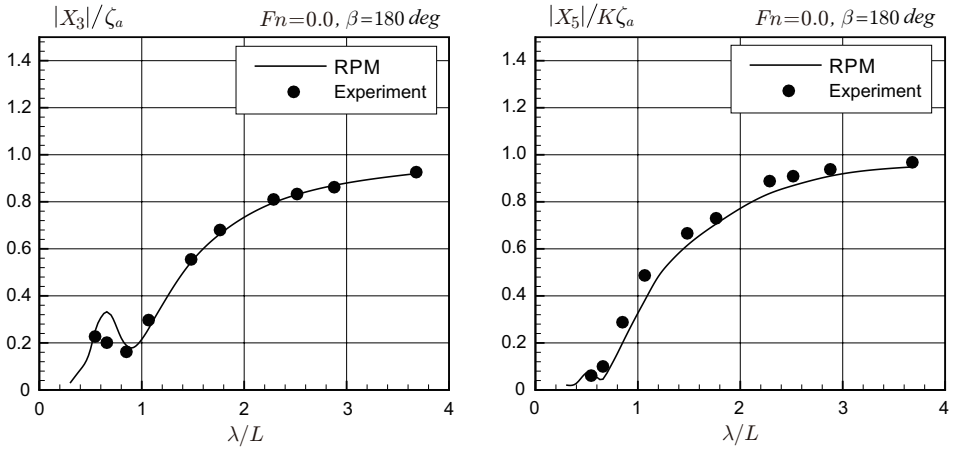

FIGURE 5.14: Comparison of heave and picth RAOs of 6750-TEU container ship, at $Fn = 0.0$ and $H/\lambda < 1/100$ in head waves (experiment data by Kim *et al.* [2])

Table 5.4. This benchmark test was conducted to assess the performance of seakeeping analysis codes and the results were disclosed at the ITTC-ISSC joint workshop in 2014. The experimental results were provided by KRISO and summarized by Kim *et al.* [2].

Since the tested container ship model was constructed using a flexible backbone and segmented hulls, hydroelastic responses may be prominent in waves especially for the forward-speed case. Thus for a comparison with the present method, the zero-speed test condition is chosen, which may satisfy the quasi-static assumption and the results are mostly linear. The tested ship model

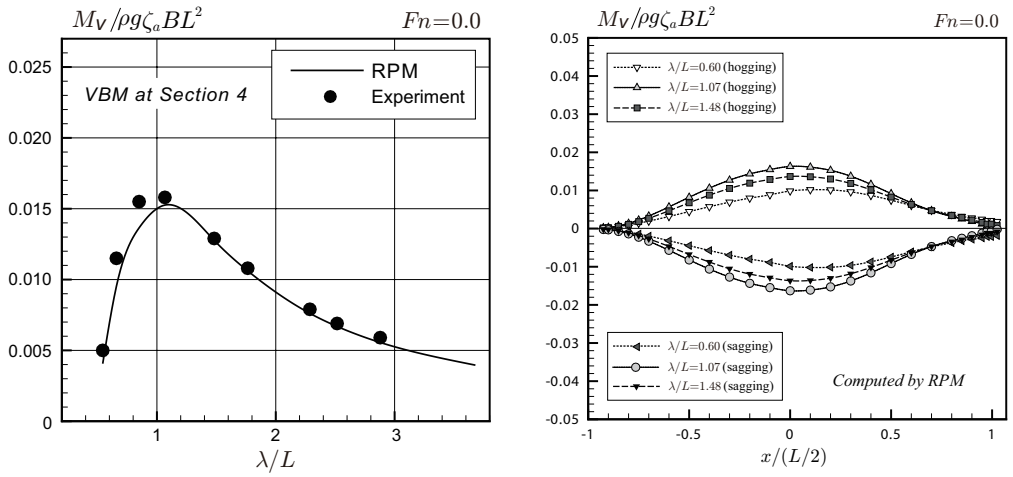

FIGURE 5.15: Validation of vertical bending moment (VBM) on 6750-TEU container ship, Left: comparison of VBM at Section 4, Right: longitudinal distribution of VBM computed by RPM (experiment data by Kim *et al.* [2])

TABLE 5.5: The results and relative errors of heave, pitch, and VBM at Section 4 of 6750-TEU container ship, Kim *et al.* [2]

Case	λ/L	$\lvert X_3\rvert/\zeta_a$			$\lvert X_5\rvert/\zeta_a$			$\lvert M_V\rvert/\rho g\zeta_a BL^2$		
		Exp	RPM	$E(\%)$	Exp	RPM	$E(\%)$	Exp	RPM	$E(\%)$
1	0.54	0.227	0.249	9.7	0.061	0.073	19.7	0.0050	0.0040	−20
2	0.67	0.201	0.332	65.2	0.100	0.046	−54	0.0115	0.0100	−13
3	0.85	0.162	0.189	16.7	0.288	0.199	−30.9	0.0155	0.0136	−12.3
4	1.07	0.297	0.260	−12.5	0.487	0.380	−22	0.0158	0.0153	−3.2
5	1.48	0.555	0.544	−2	0.666	0.615	−7.7	0.0129	0.0128	−0.8
6	1.76	0.680	0.663	−2.5	0.730	0.706	−3.3	0.0108	0.0106	−1.9
7	2.28	0.810	0.796	−1.7	0.888	0.836	−5.9	0.0079	0.0076	−3.8
8	2.52	0.833	0.831	−0.2	0.909	0.869	−4.4	0.0069	0.0067	−2.9
9	2.88	0.862	0.870	0.9	0.938	0.909	−3.1	0.0059	0.0056	−5.1
10	3.68	0.926	0.920	−0.6	0.968	0.948	−2.1	-	0.0040	-

consists of eight segmented hulls. The mass at each segmented hull approaches a uniform distribution and thus the total mass distribution is assumed equal to the distribution of volume displacement. Sectional forces were measured at seven sections by strain gauges installed on the backbone. Since the results are expected to be linear, comparison with the benchmark test data is made with the computation by RPM.

First, the RAOs of heave and pitch motions are presented in Fig. 5.14. Then the resulting VBM is shown in Fig. 5.15, where the RAO of VBM at Section 4 is compared on the left-hand side, whilst the longitudinal distribution of VBM is shown on the right-hand side for wavelengths of

λ/L = 0.6, 1.07 and 1.48. The values in digits and relative errors of the Fig. 5.14 and the left-hand side of the Fig. 5.15 are presented in Table 5.5. The amplitude of heave and pitch represents favorable agreement at wavelengths larger than λ/L = 1.07 despite slight underestimation in pitch. Looking at the amplitude of VBM at Section 4, it is noted that the maximum value of VBM is observed at λ/L = 1.07 but this maximum value is slightly underestimated with 3.2% by RPM; which may be attributed to a slight underestimation of heave and pitch motions as indicated at λ/L = 1.07. Slight underestimation of ship motions results in some underestimation of VBM at Section 4 for the corresponding wavelengths. Nonetheless, in general, the VBM computed by RPM is in good agreement with the results directly measured using a ship model with backbone and segmented hulls.

Chapter 6

Conclusions

- In order to provide world's first experimental data of the spatial distribution of wave-induced unsteady pressure on the whole hull surface of a ship oscillating in waves, an unprecedented experiment was conducted, measuring the pressures at a large number of locations on the ship hull simultaneously in terms of 333 FBG pressure sensors affixed with double-sided tape on almost whole ship-hull surface.

- We note some remarkable keys to success for this proposed method. To calculate the vertical bending moment distribution accurately from the measured pressure by using the FBG pressure sensors, the synchronization of the time histories of the ship-side wave indicating the wetted surface of the ship hull, spatial pressure, and ship motions are of the critical points.

- To detect the time-variant wetted surface of the ship hull, the measurement of incident head wave, wave-induced ship motions and ship-side wave profile was also carried out, and all the data were synchronized by adjusting the phase of all data in terms of the complex amplitude of incident wave obtained after the Fourier-series analysis. The time history of the spatial distribution of unsteady pressure was obtained with a spline-interpolation technique using point-wise pressures measured at 333 points which include a bow area above the still waterline.

- Since the pressure distribution is the base for computing almost all hydrodynamic quantities like total hydrodynamic forces, the VBM distribution, the added resistance, ship motions and so on, the experimental data obtained in this study can be effectively used for deepening our understanding of local physical phenomena; for example, which part of the ship hull provides dominant pressures to the physical quantity concerned, what kind of nonlinearities or hydrodynamic cancellation are essential in understanding the phenomenon in question.

- Validation of obtained data of unsteady pressure has been made by confirming the repeatability, namely the standard deviation, of the measured results and by comparing the measured and computed values along the girth at some of the transverse sections where the pressure measurement has been done. The pressure distribution obtained with interpolation was compared to the results computed by RPM for the zero-speed linear case and by CFD for the forward-speed nonlinear case. Remarkable agreement for both cases could be confirmed.

- In addition, in this paper, the first-harmonic wave-exciting forces were computed by integrating the unsteady pressure distribution over the wetted surface of a motion-fixed ship model and compared with the values directly measured with dynamometer. Good agreement was also confirmed in this validation, but at the same time small discrepancy in the surge exciting force was pointed out, a reason of which should be attributed to the scarcity of FBG pressure sensors in the bow upper region, suggesting a necessity of increasing the sensors in that region for more precise study.

- In terms of measured and computed spatial distribution of unsteady pressure and wave-induced ship motions, the longitudinal distribution of the VBM along the ship's length was computed and shown in a form of maximum values in the hogging and sagging moments. Obtained results by using only the measured data agreed well with computed results not only for the zero-speed linear case but also for the forward-speed nonlinear case. Especially for the latter case of $Fn = 0.18$, asymmetric and hence nonlinear property in the VBM was clearly observed with larger value in the sagging moment by both experiment and CFD computation.

- The error values in the nonlinear VBM were presented at several longitudinal positions and it could be seen from these values that the degree of agreement between measured and computed results is good especially at around the motion-resonant wavelengths.

- As an important forward-speed effect, it was also observed that the longitudinal position where the sectional VBM takes maximum is shifted forward from the midship due to large increase in the unsteady pressure in the bow region and also increase in the ship motions particularly near the motion-resonant frequency. This detailed understanding on the forward-speed effect on the VBM is remarkable.

- As further validation, a comparison was also made with the benchmark data used in the ITTC-ISSC joint workshop for the frequency-response function of the VBM measured at a specified longitudinal position using a segmented model of 6750-TEU container ship. Favorable agreement was confirmed also in this comparison.

- From these favorable results, the method proposed in this study may provide a new paradigm for obtaining experimentally the VBM distribution at any position, and obtained results could be useful as the validation data for other numerical computation methods.

Appendix A

Ship-side Wave Experiment Results

The ship-side wave is critical particularly for the accurate analysis of nonlinearity concerning the time instant synchronization. For a parametric study, the ship-side wave experiment results at forward-speed $Fn = 0.18$ then are provided for a wide range of wavelengths of eight cases according to the unsteady pressure measurement, $\lambda/L = 0.3 \sim 2.0$ as shown in Fig. A.1 - A.8. Nevertheless, five cases are considered to be sufficient to represent the response behavior in low to the high frequency that is the cases of $\lambda/L = 0.8 \sim 2.0$ for which mainly emphasizing the resonant frequency as a critical case for the VBM. The unsteady first-harmonic and second-harmonic wave profiles are presented along with the steady wave profile for each case. The first-harmonic component however is the dominant part for the analysis of VBM. Wave profiles captured to represent the time instant when the crest of incident wave coincides at the origin of the coordinate system. Thereby, for each case, the shifting value of the time histories then obtained and to be used for the subsequent analysis of pressure distribution and ship motions.

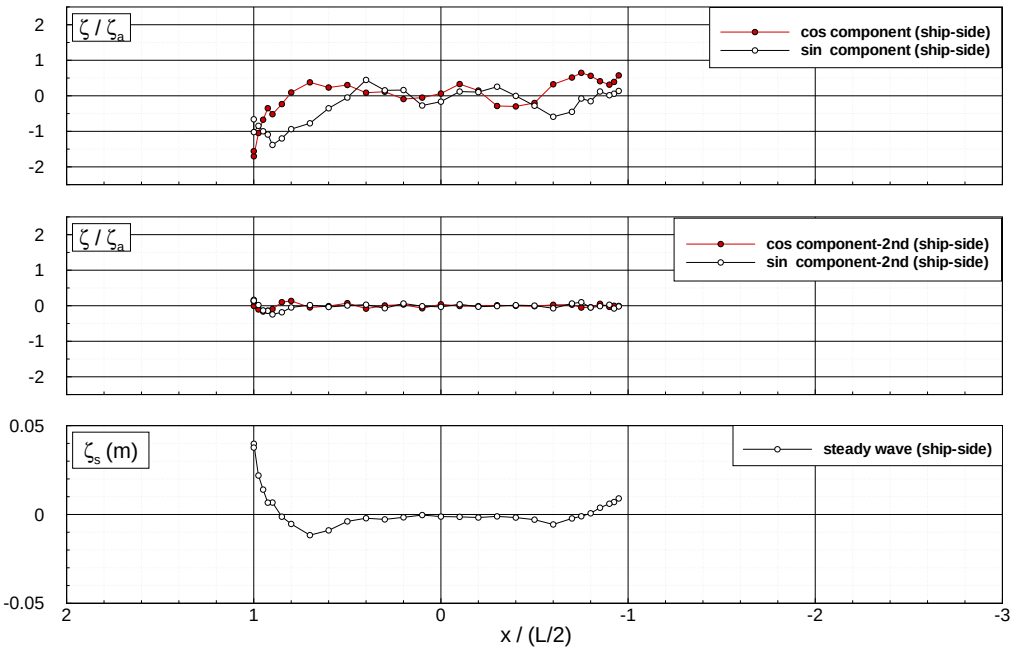

FIGURE A.1: Wave profile measured along ship-side of RIOS bulk carrier at $Fn = 0.18$, $\lambda/L = 0.3$ in head wave. Values are shown with ζ/ζ_a and $\zeta_a = 0.0240$ m.

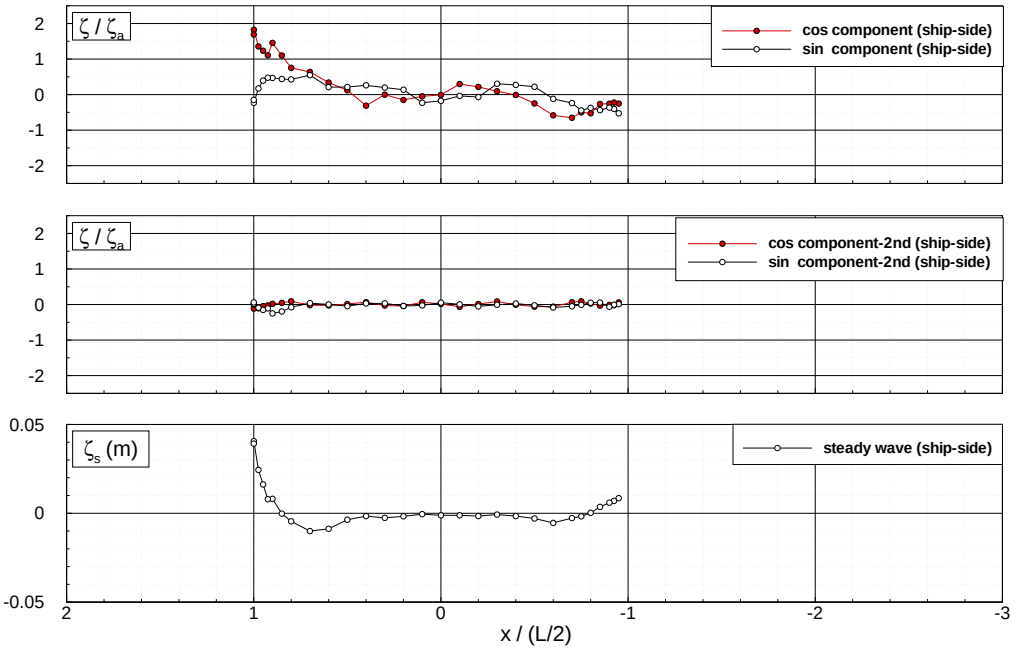

FIGURE A.2: Wave profile measured along ship-side of RIOS bulk carrier at $Fn = 0.18$, $\lambda/L = 0.4$ in head wave. Values are shown with ζ/ζ_a and $\zeta_a = 0.0240$ m.

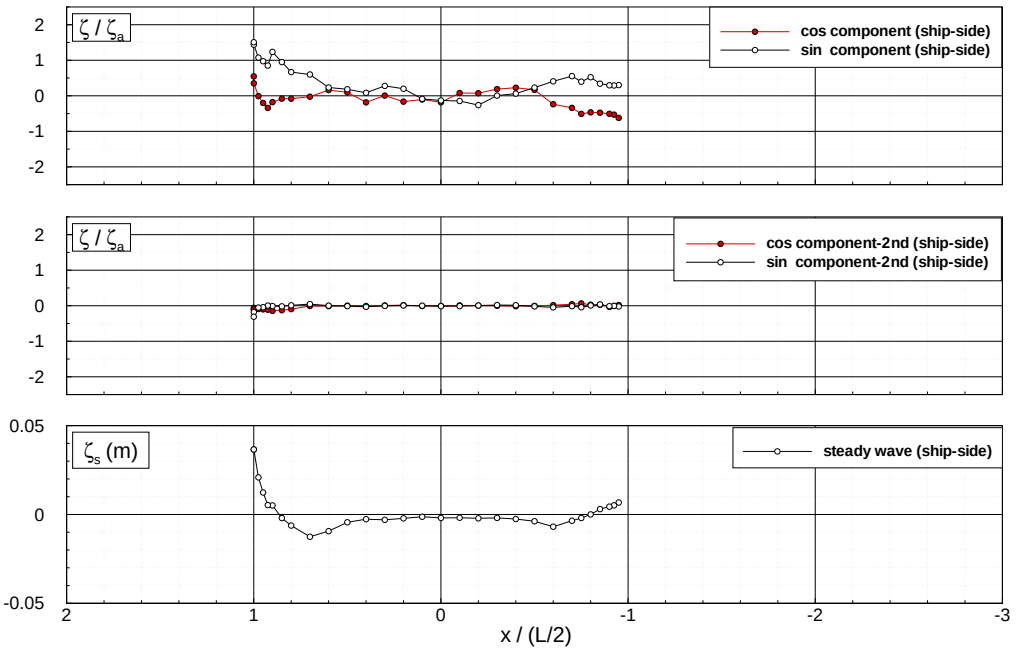

FIGURE A.3: Wave profile measured along ship-side of RIOS bulk carrier at $Fn = 0.18$, $\lambda/L = 0.5$ in head wave. Values are shown with ζ/ζ_a and $\zeta_a = 0.0240$ m.

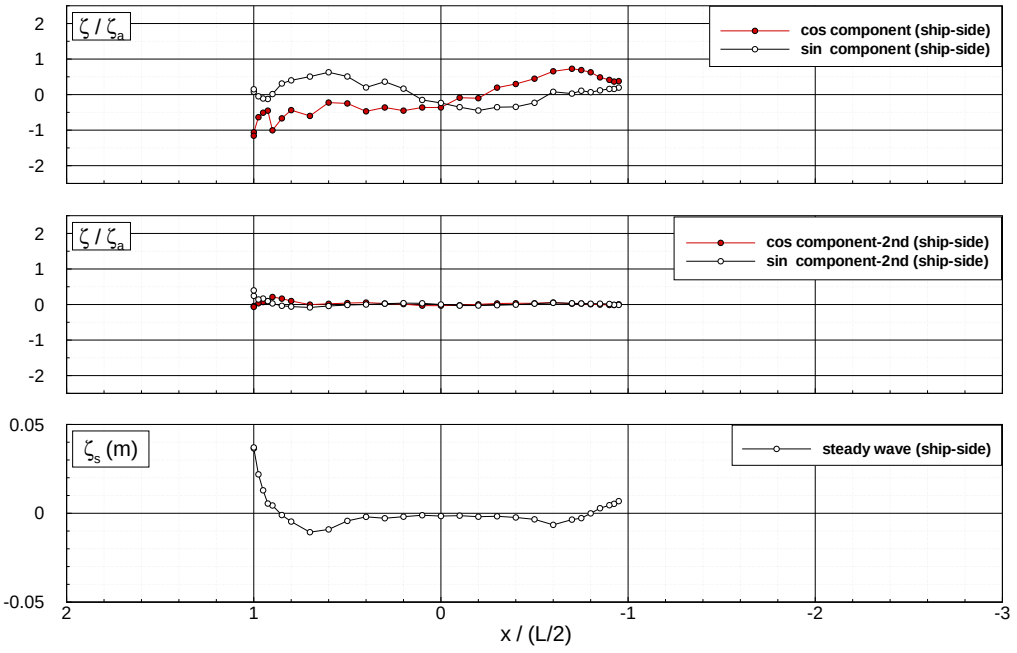

FIGURE A.4: Wave profile measured along ship-side of RIOS bulk carrier at $Fn = 0.18$, $\lambda/L = 0.8$ in head wave. Values are shown with ζ/ζ_a and $\zeta_a = 0.0240$ m.

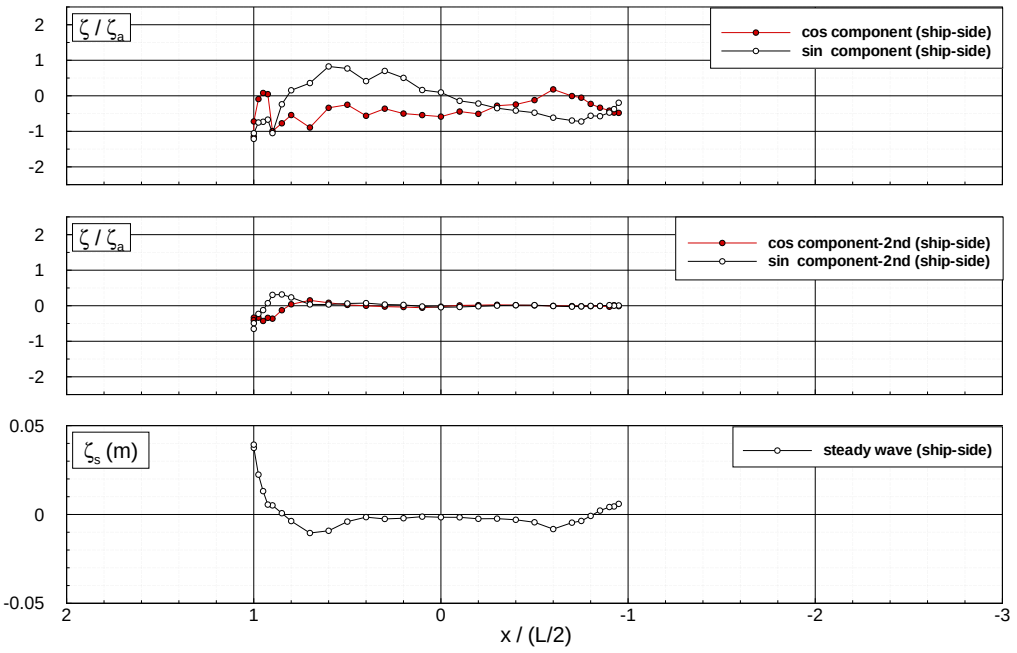

FIGURE A.5: Wave profile measured along ship-side of RIOS bulk carrier at $Fn = 0.18$, $\lambda/L = 1.0$ in head wave. Values are shown with ζ/ζ_a and $\zeta_a = 0.0240$ m.

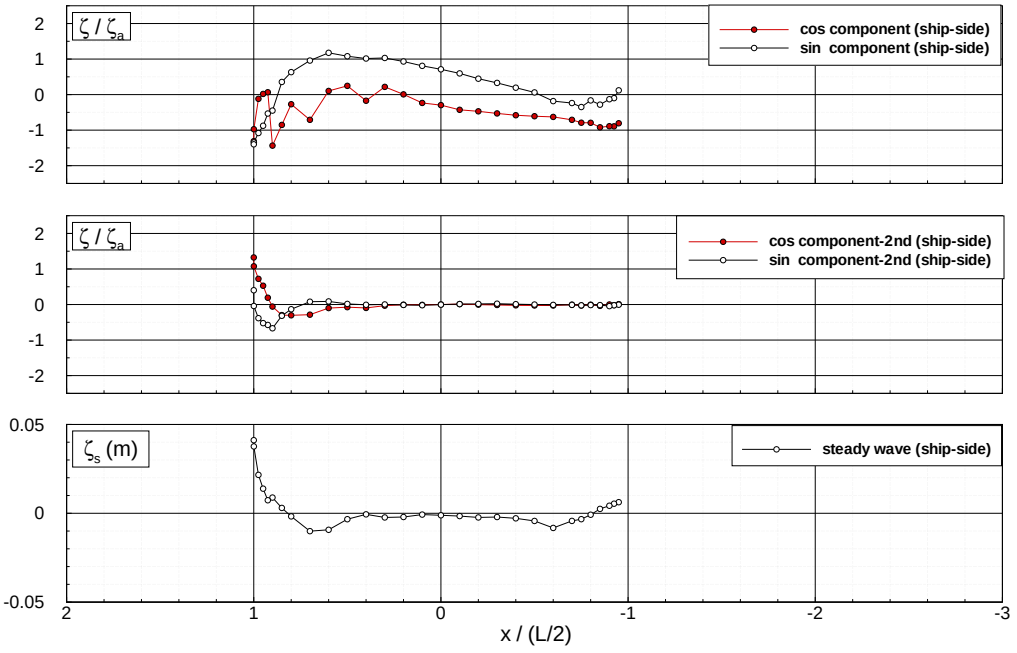

FIGURE A.6: Wave profile measured along ship-side of RIOS bulk carrier at $Fn = 0.18$, $\lambda/L = 1.25$ in head wave. Values are shown with ζ/ζ_a and $\zeta_a = 0.0240$ m.

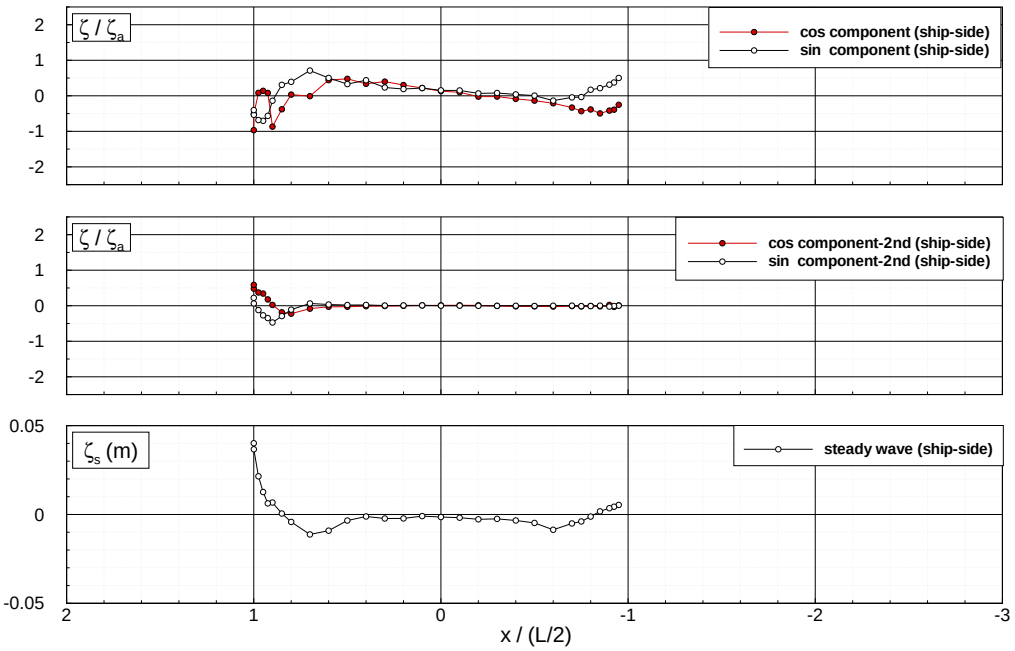

FIGURE A.7: Wave profile measured along ship-side of RIOS bulk carrier at $Fn = 0.18$, $\lambda/L = 1.5$ in head wave. Values are shown with ζ/ζ_a and $\zeta_a = 0.0240$ m.

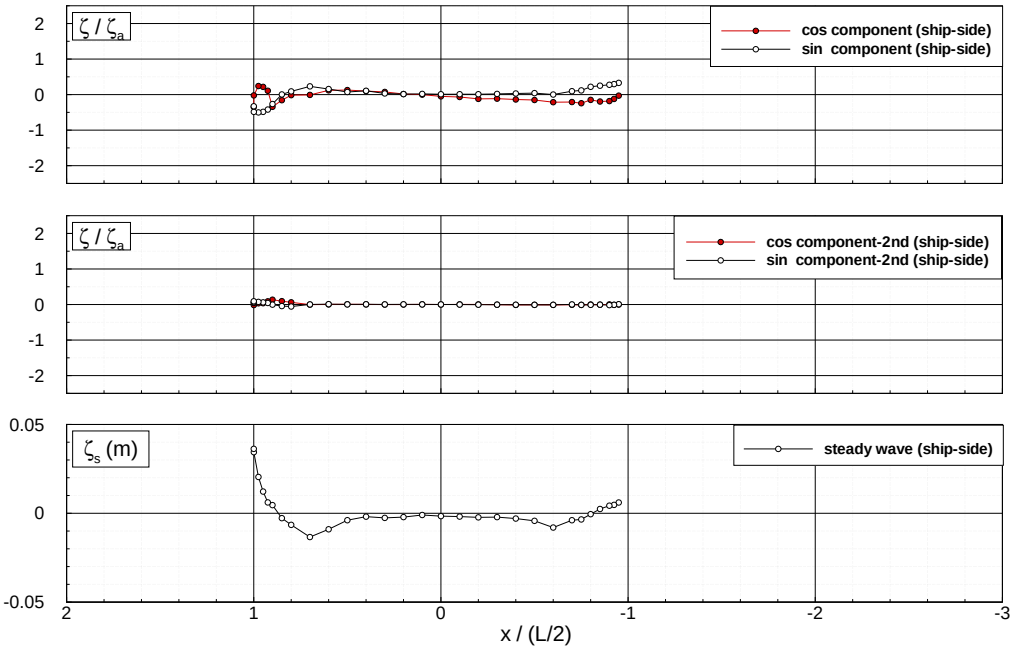

FIGURE A.8: Wave profile measured along ship-side of RIOS bulk carrier at $Fn = 0.18$, $\lambda/L = 2.0$ in head wave. Values are shown with ζ/ζ_a and $\zeta_a = 0.0240$ m.

Appendix B

Unsteady Pressure Distribution Results

As another evidence of the results for unsteady pressure distribution, the comparison between experimental data and computed results are presented as a parametric study. The pressure is shown in the nondimensional form of $p/\rho g\zeta_a$ and $\zeta_a = 0.0106$ m and 0.0204 m for the zero-speed and forward-speed, respectively in accordance with the experiment. The color scale in the contour display is taken from -2.0 to $+2.0$ with minus value means the pressure inward the ship-hull surface. It should be noted that the contour display is kept the same for the zero-speed and forward-speed to see the relative magnitude. The phase of time instant θ is taken such that $\theta = 0$ corresponds to the maximum sagging moment.

B.1 Zero-speed in head wave

A side view of the spatial distribution of unsteady pressure is depicted in Fig. B.1 - B.5 for the cases of $\lambda/L = 0.8 - 2.0$ in head wave and $Fn = 0.0$. Overall, for the linear cases, a good agreement can be seen between experimental data and computed results by RPM. It should be noted that the undulated plot of the experimental data comes from the limitation of the interpolation around the bulbous bow part. There is an obvious difference around the bow part for the case of zero-speed at $\lambda/L = 0.8$ shown in Fig. B.1. It is also noted that the analysis of pressure around the waterline for the experiment conducted in 2016 hasn't considered the correction properly whereas the latest has applied.

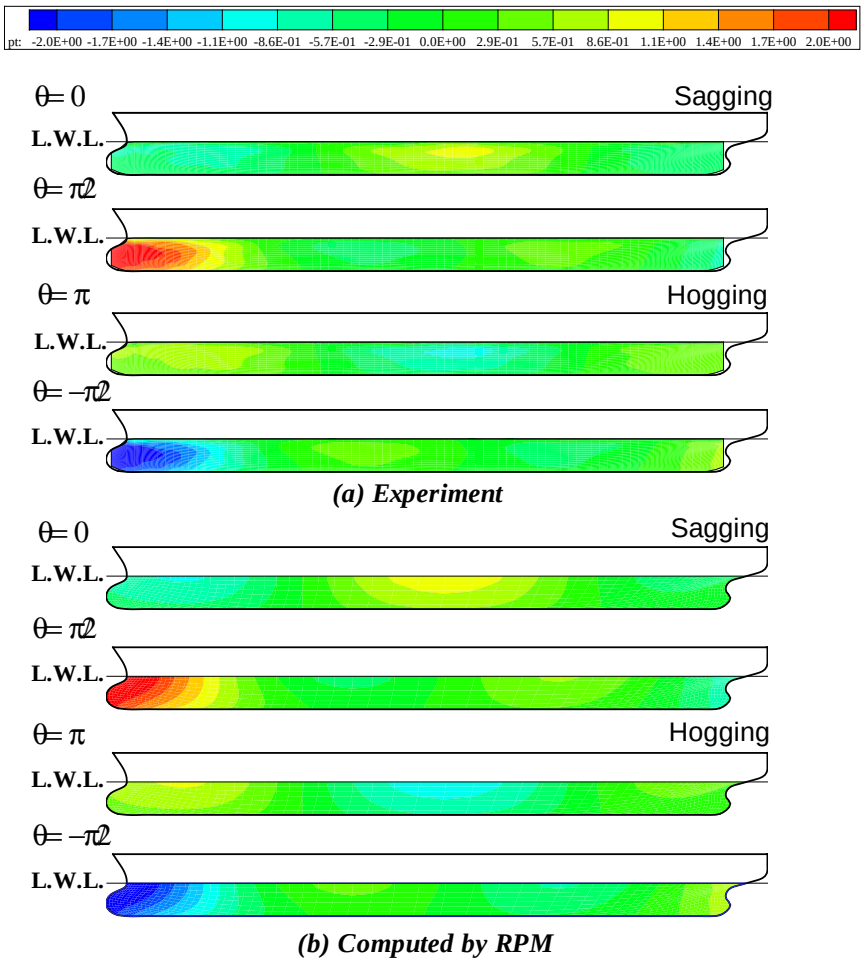

FIGURE B.1: Unsteady pressure distribution at $\lambda/L = 0.8$ and $Fn = 0.0$ in head wave; (a) Experiment, (b) Computation by RPM. Values are shown with $p/\rho g\zeta_a$ and $\zeta_a = 0.0106$ m.

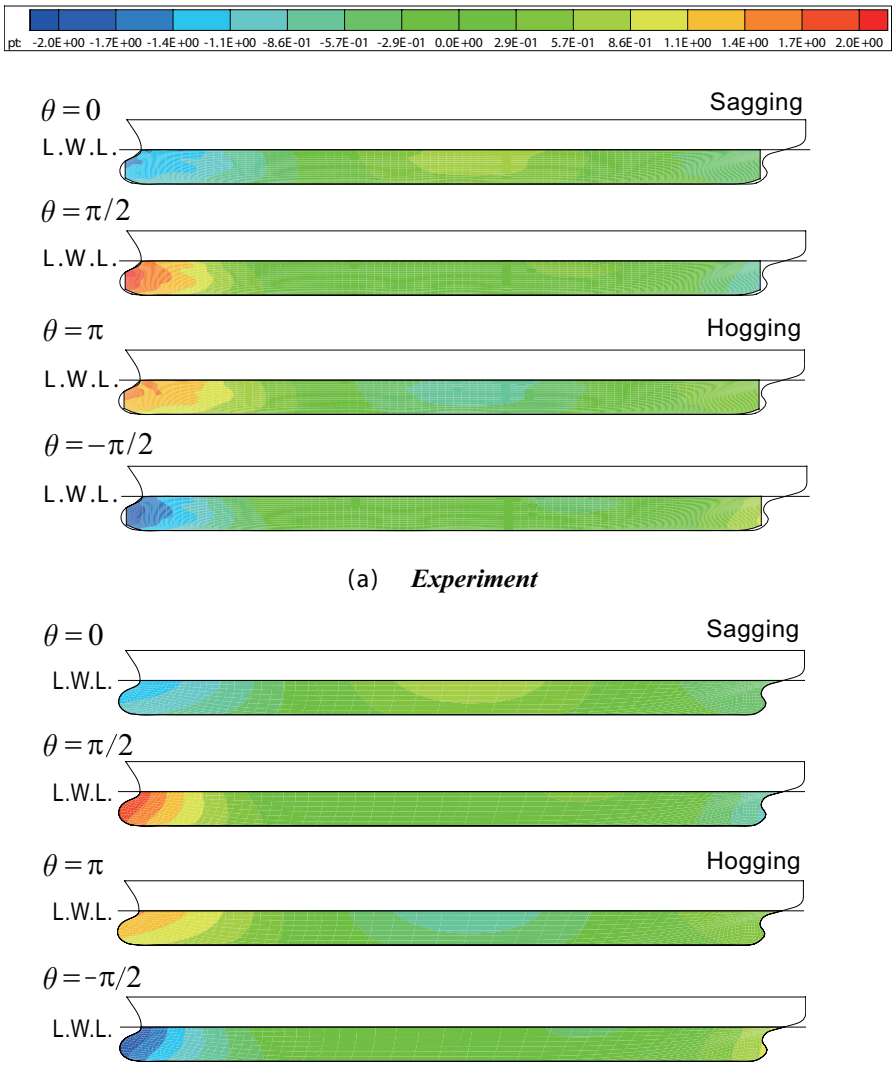

FIGURE B.2: Unsteady pressure distribution at $\lambda/L = 1.0$ and $Fn = 0.0$ in head wave; (a) Experiment, (b) Computation by RPM. Values are shown with $p/\rho g\zeta_a$ and $\zeta_a = 0.0106$ m.

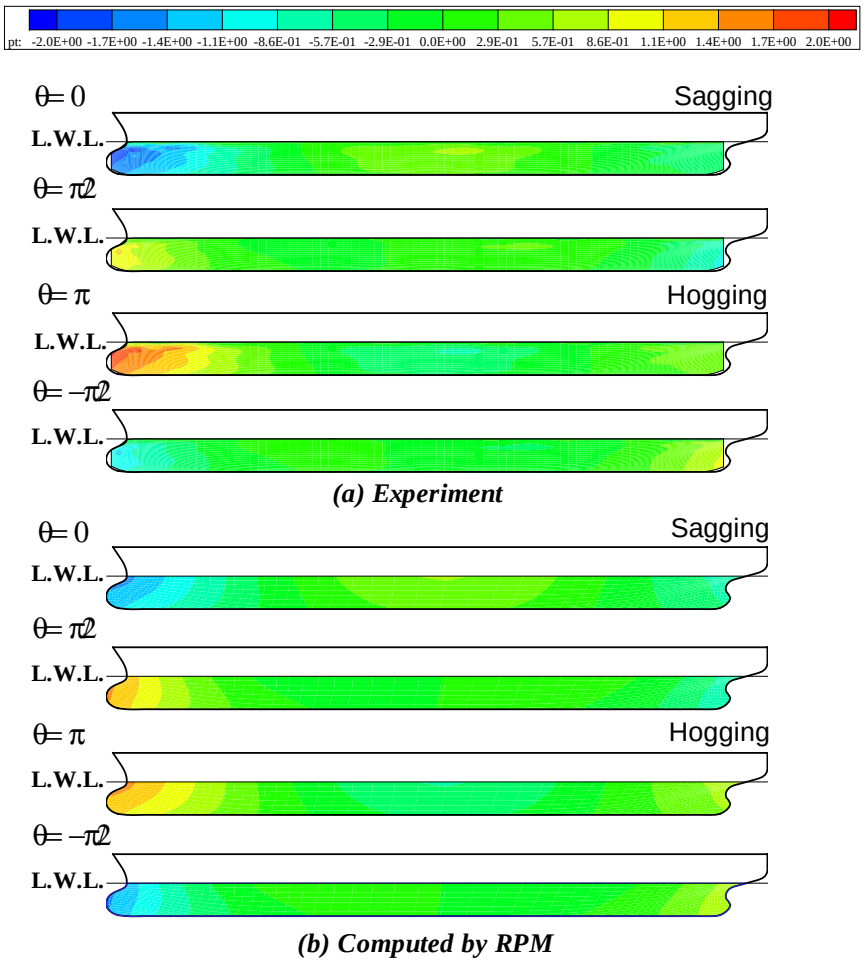

FIGURE B.3: Unsteady pressure distribution at $\lambda/L = 1.25$ and $Fn = 0.0$ in head wave; (a) Experiment, (b) Computation by RPM. Values are shown with $p/\rho g\zeta_a$ and $\zeta_a = 0.0106$ m.

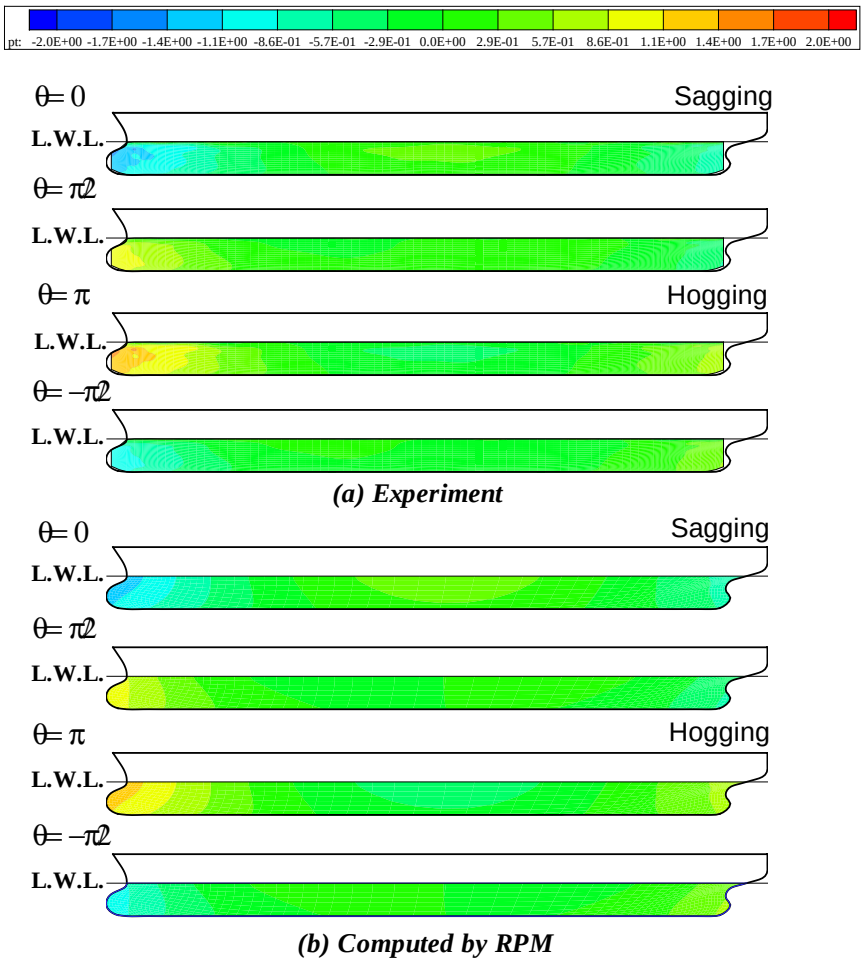

FIGURE B.4: Unsteady pressure distribution at $\lambda/L = 1.5$ and $Fn = 0.0$ in head wave; (a) Experiment, (b) Computation by RPM. Values are shown with $p/\rho g\zeta_a$ and $\zeta_a = 0.0106$ m.

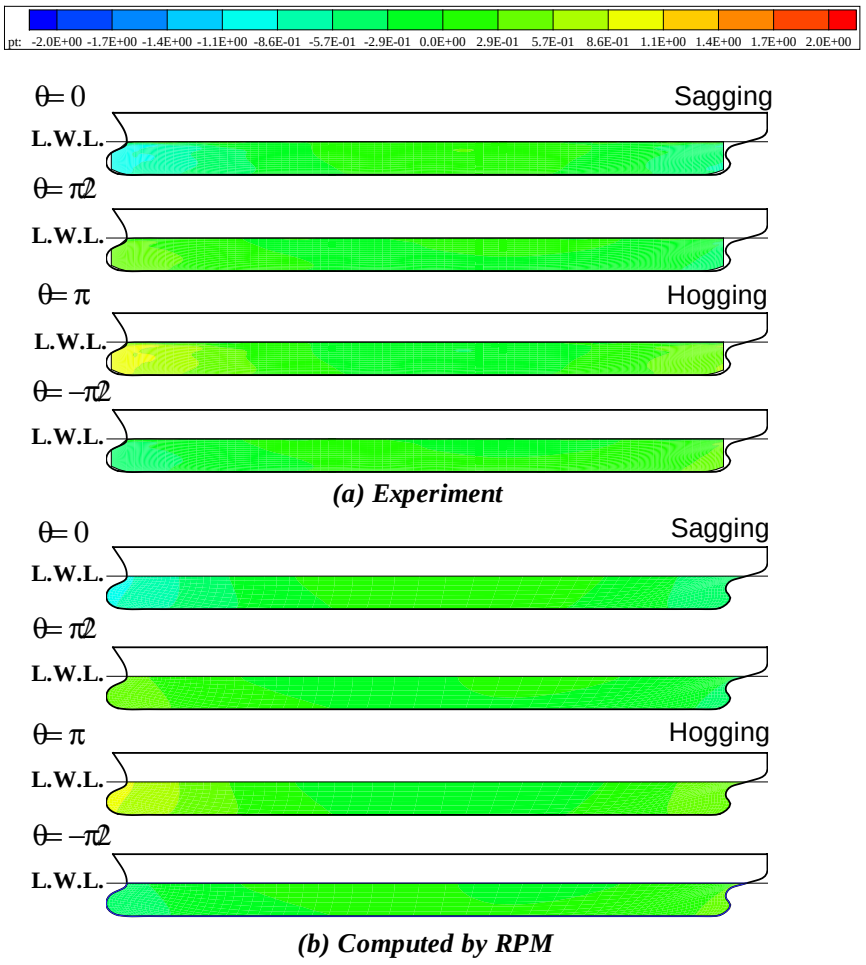

FIGURE B.5: Unsteady pressure distribution at $\lambda/L = 2.0$ and $Fn = 0.0$ in head wave; (a) Experiment, (b) Computation by RPM. Values are shown with $p/\rho g\zeta_a$ and $\zeta_a = 0.0106$ m.

B.2 Forward-speed in head wave

A side view of the unsteady pressure distribution is depicted in Fig. B.6 - B.10 for the cases of $\lambda/L = 0.8 - 2.0$ in head wave and $Fn = 0.18$. A comparison is made between experiment and nonlinear computation by CFD FINE/Marine. As obvious from the figures, the magnitude of pressure seems large particularly around the bow area at $\lambda/L = 1.0$ and reaching the maximum at $\lambda/L = 1.25$. In conjunction with a large amplitude of ship motions, the nonlinearity is conspicuous especially when looking at the pressure quantity above the waterline. The buoyancy force distribution depends on the underwater profile of the ship, which keep changing because the ship keeps encountering waves at different heights. This evidence attributes to an important forward-speed effect where the sectional VBM takes maximum is shifted forward from the midship and also the asymmetric property of the hogging and sagging. Overall good agreement can be seen between experimental data and computed results by CFD for all wavelengths.

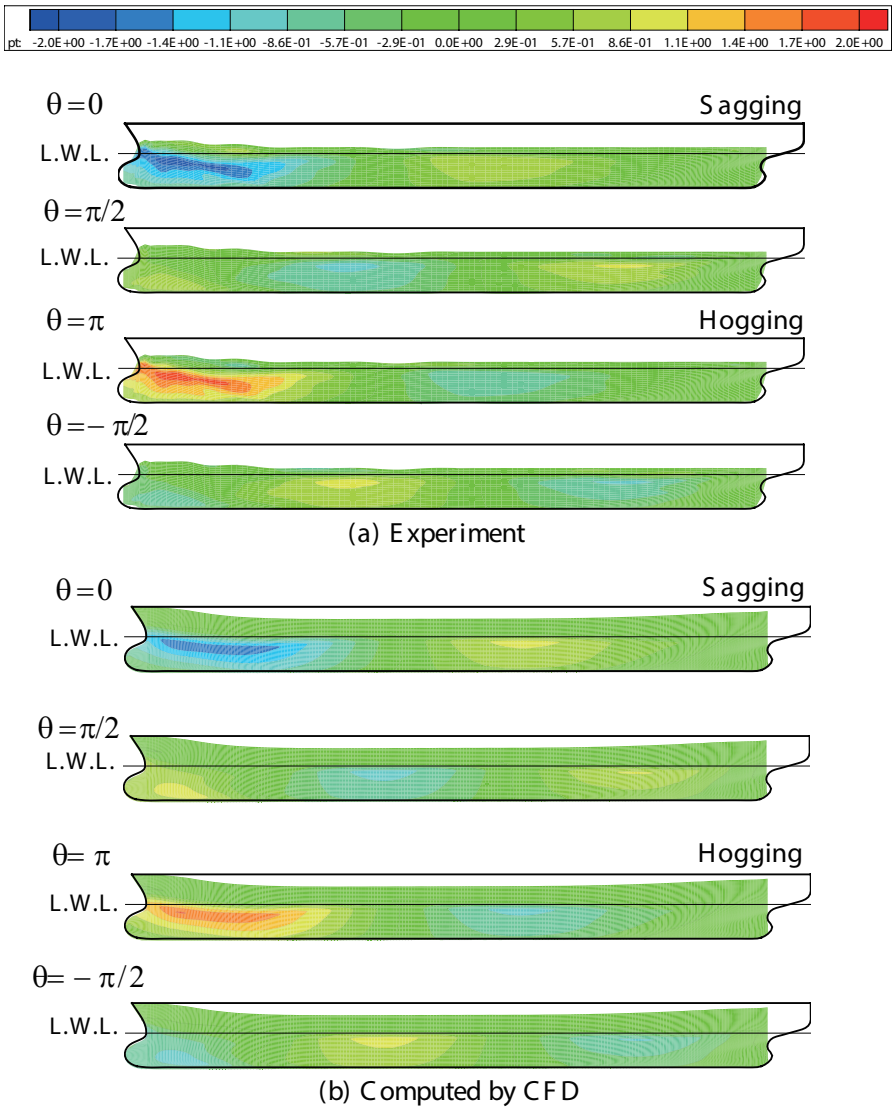

FIGURE B.6: Unsteady pressure distribution at $\lambda/L = 0.80$ and $Fn = 0.18$ in head wave; (a) Experiment, (b) Computation by CFD. Values are shown with $p/\rho g\zeta_a$ and $\zeta_a = 0.0240$ m.

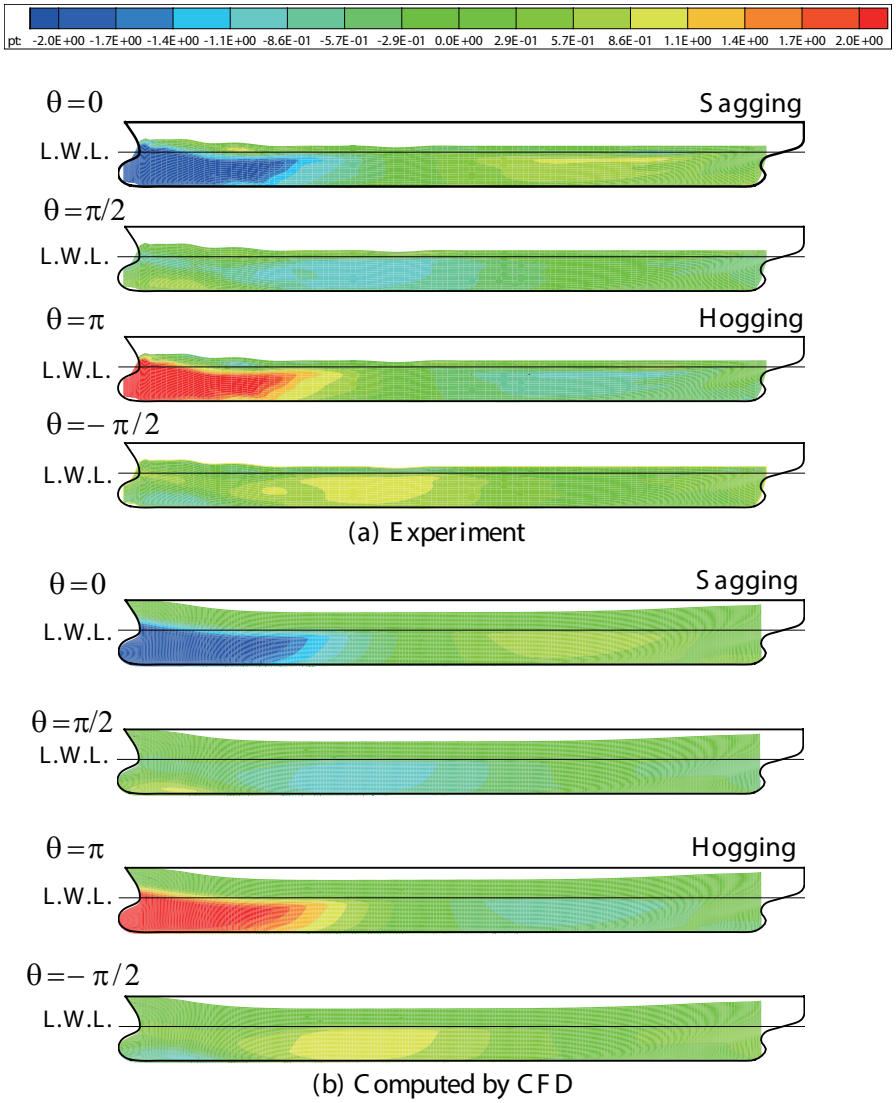

FIGURE B.7: Unsteady pressure distribution at $\lambda/L = 1.00$ and $Fn = 0.18$ in head wave; (a) Experiment, (b) Computation by CFD. Values are shown with $p/\rho g\zeta_a$ and $\zeta_a = 0.0240$ m.

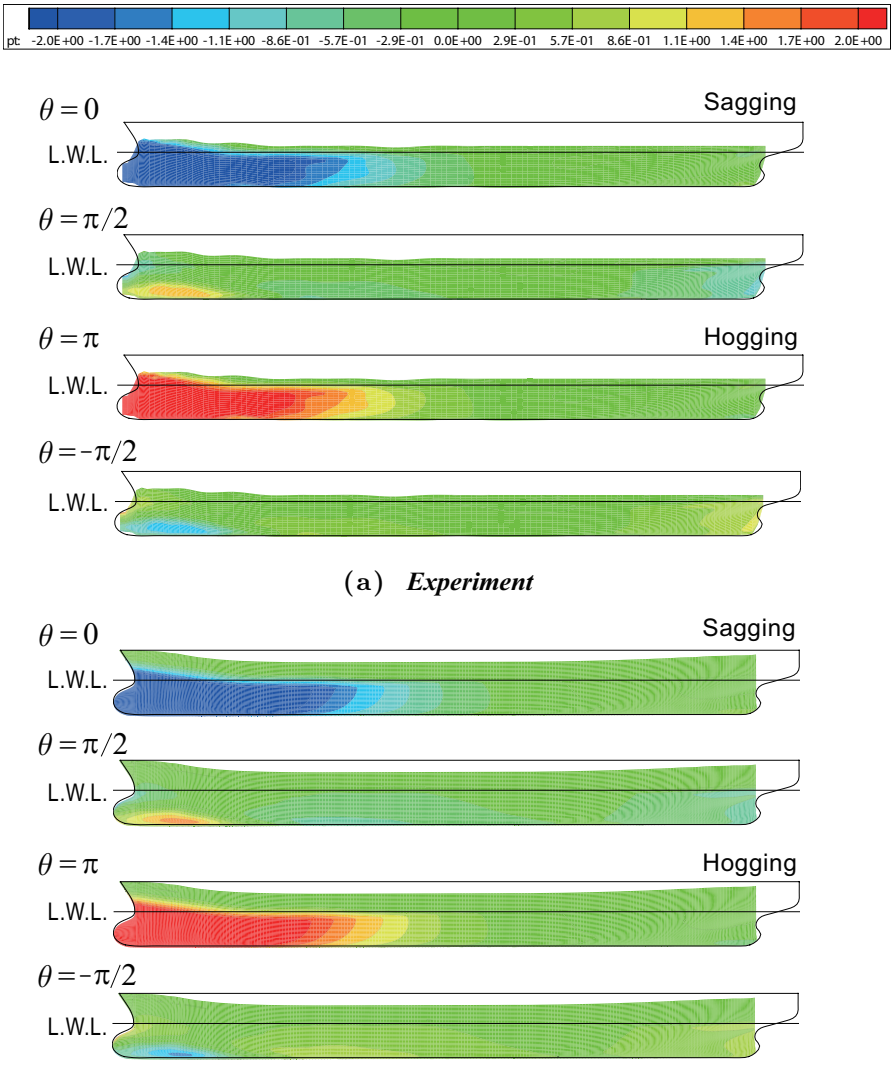

FIGURE B.8: Unsteady pressure distribution at $\lambda/L = 1.25$ and $Fn = 0.18$ in head wave; (a) Experiment, (b) Computation by CFD. Values are shown with $p/\rho g\zeta_a$ and $\zeta_a = 0.0240$ m.

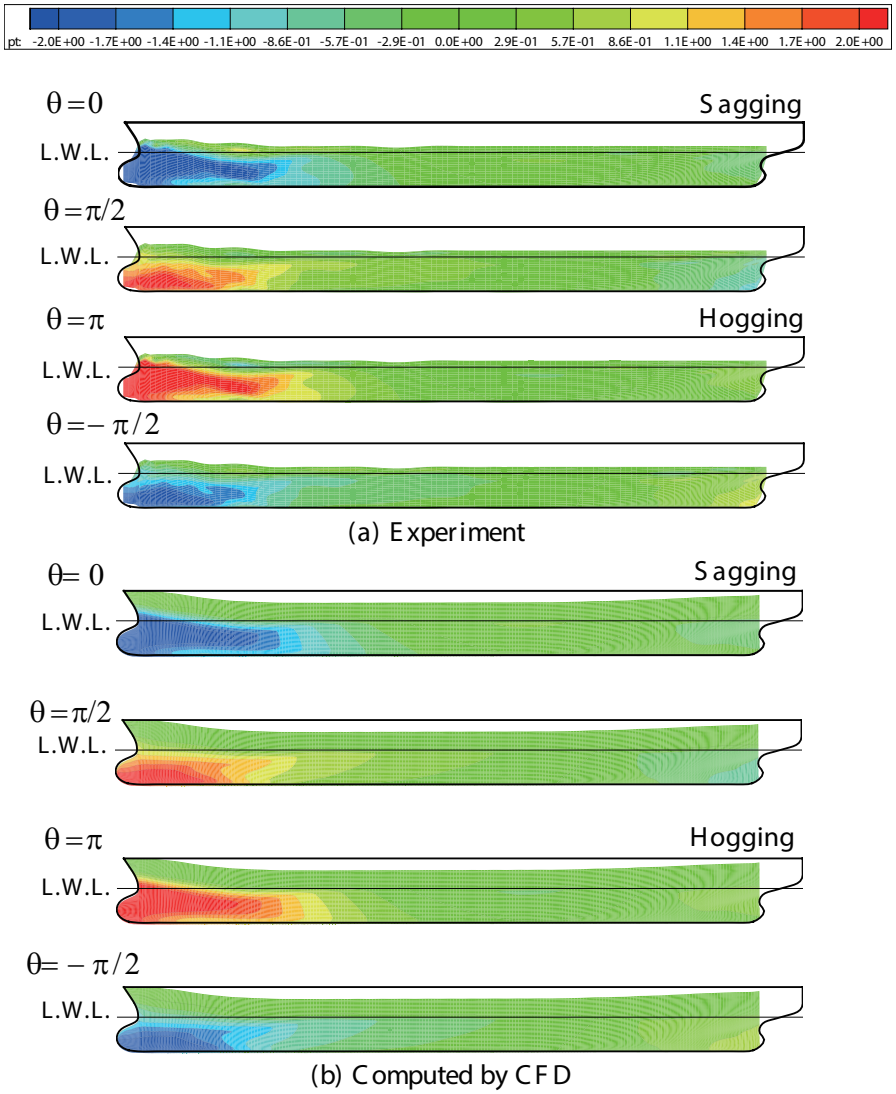

FIGURE B.9: Unsteady pressure distribution at $\lambda/L = 1.50$ and $Fn = 0.18$ in head wave; (a) Experiment, (b) Computation by CFD. Values are shown with $p/\rho g\zeta_a$ and $\zeta_a = 0.0240$ m.

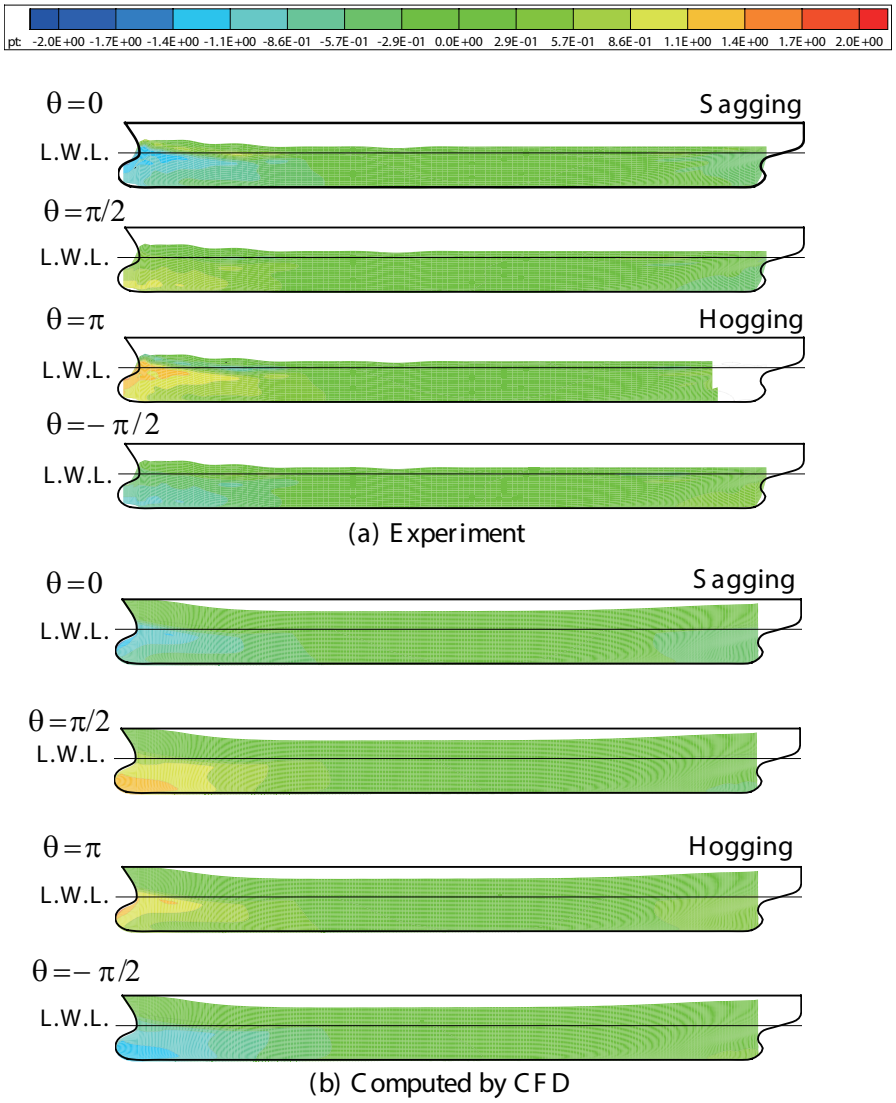

FIGURE B.10: Unsteady pressure distribution at $\lambda/L = 2.00$ and $Fn = 0.18$ in head wave; (a) Experiment, (b) Computation by CFD. Values are shown with $p/\rho g\zeta_a$ and $\zeta_a = 0.0240$ m.

Appendix C

Vertical Bending Moment Distribution Results

In Chapter 5, the results of VBM of zero-speed and forward-speed at motion resonants i.e. $\lambda/L = 1.0$ and $\lambda/L = 1.25$ are discussed. In addition, to understand the phenomena more comprehensively a parametric study is made such that the ship-side wave and unsteady pressure in the preceding Appendices. As obvious from Eq. (4.1), the VBM can be obtained mainly from the unsteady pressure and vertical motion acceleration. Moreover, as presented in Appendices B and Chapter 5, the unsteady pressure and ship motions show a good agreement and reasonable discrepancy even on the vicinity of nonlinear cases. Therefore, We may expect a good agreement also in the VBM distribution. The VBM distribution is plotted in a nondimensional form divided by $\rho g \zeta_a L^2$. The color scale in the contour display is set from $-3.0E-4$ to $+3.0E-4$ for the zero-speed case, with the number of the mesh of 40 and 80 at vertical and longitudinal, respectively. It should be noted however to keep the visibility in comparison, the color scale of the forward-speed case is adjusted higher from $-1.0E-3$ to $+1.0E-3$. Minus value means the sagging of VBM and vice versa.

C.1 Zero-speed in head wave

A side view of the spatial distribution of VBM is depicted in Fig. C.1 - C.5 for the cases of $\lambda/L = 0.8 - 2.0$ in head wave and $Fn = 0.0$. Likewise, on the comparison of unsteady pressure distribution, the experiment and computed results by RPM are compared and overall good agreement can be seen although some discrepancies are observed at $\lambda/L = 1.25$ which likely come from the difference in ship motions.

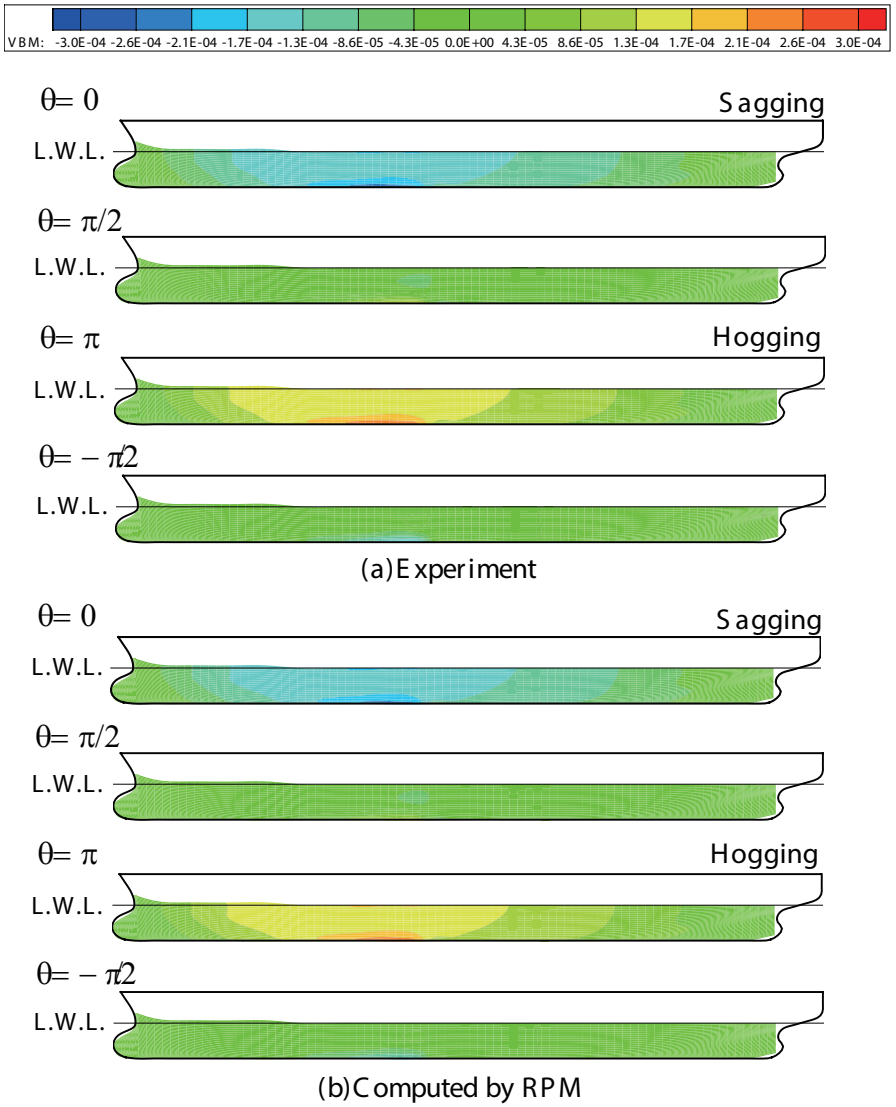

FIGURE C.1: VBM distribution at $\lambda/L = 0.80$ of head wave and $Fn = 0.00$; (a) Experiment, (b) Computation by RPM

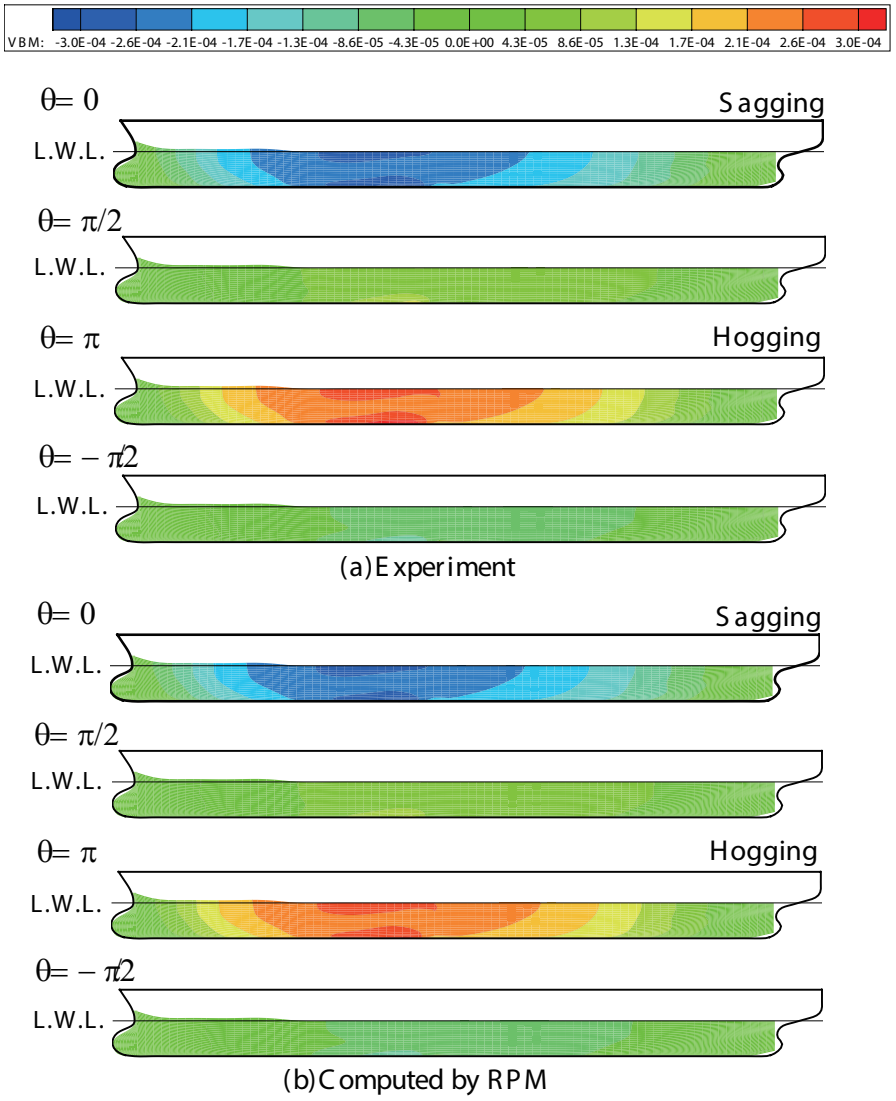

FIGURE C.2: VBM distribution at $\lambda/L = 1.00$ of head wave and $Fn = 0.00$; (a) Experiment, (b) Computation by RPM

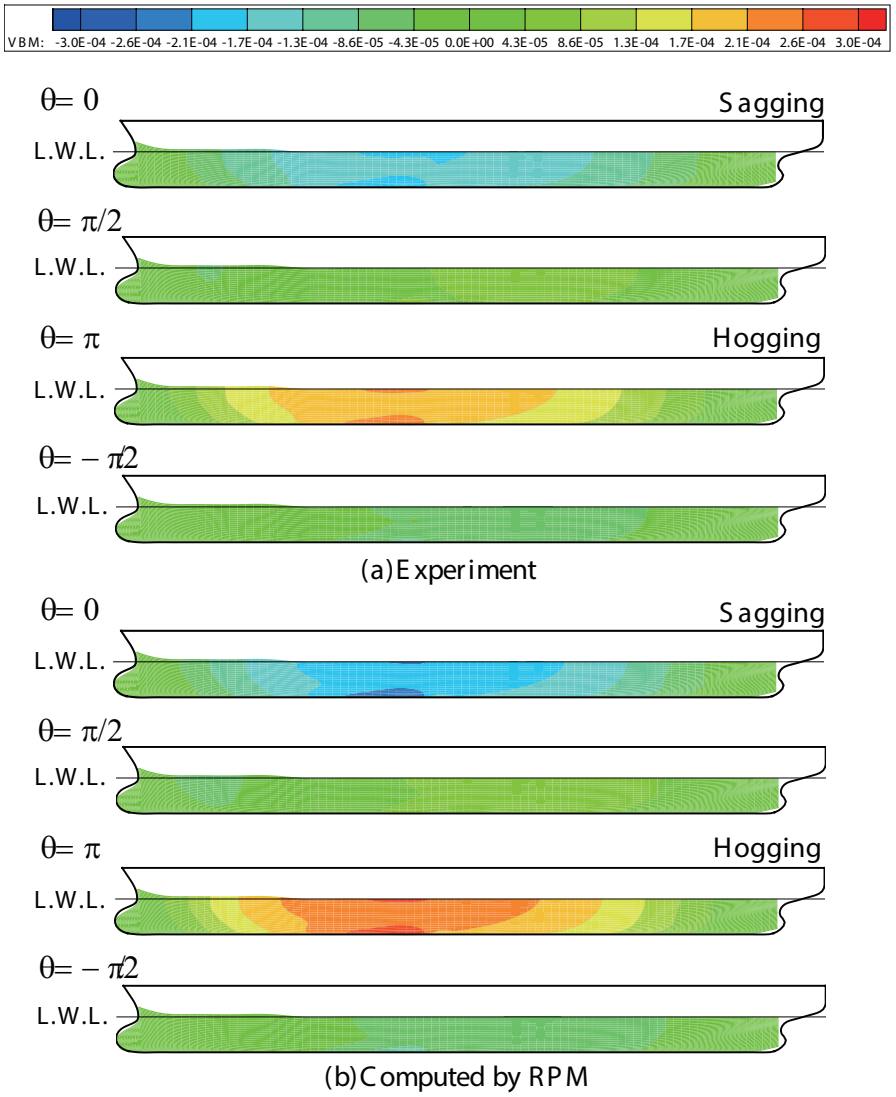

FIGURE C.3: VBM distribution at $\lambda/L = 1.25$ of head wave and $Fn = 0.00$; (a) Experiment, (b) Computation by RPM

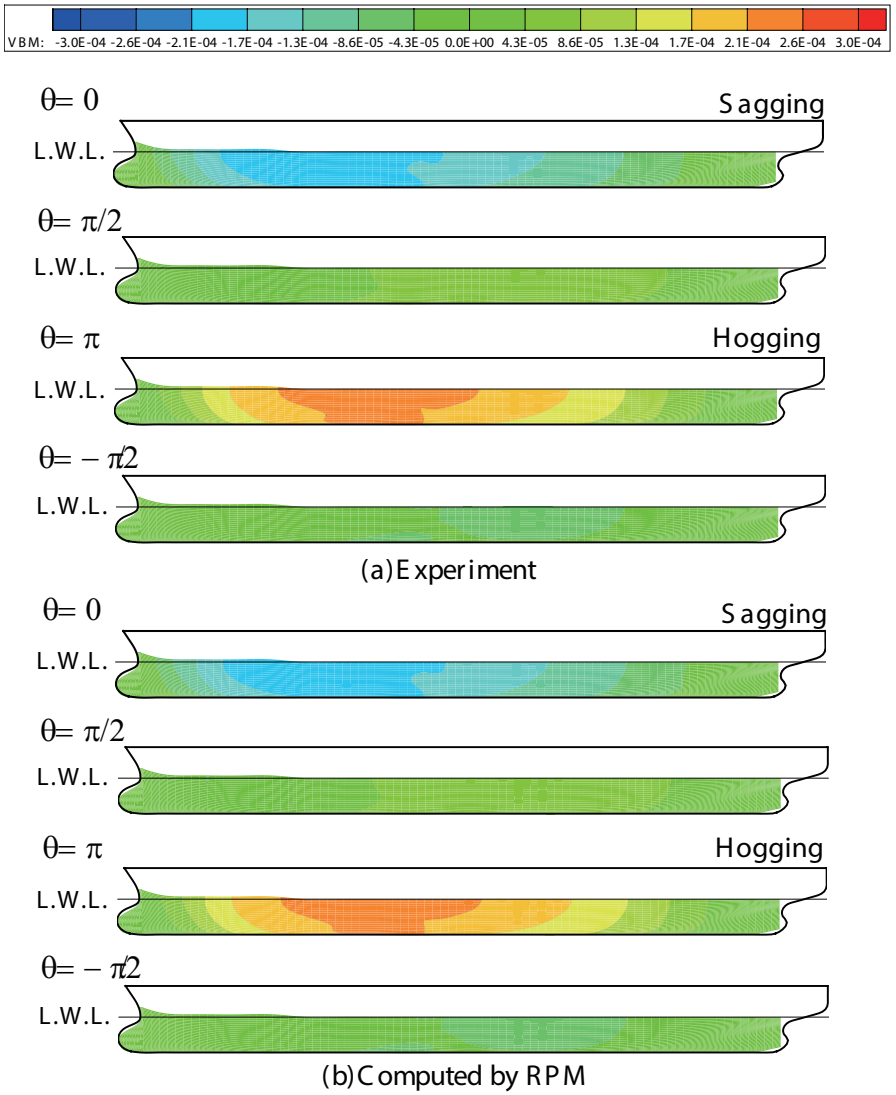

FIGURE C.4: VBM distribution at $\lambda/L = 1.50$ of head wave and $Fn = 0.00$; (a) Experiment, (b) Computation by RPM

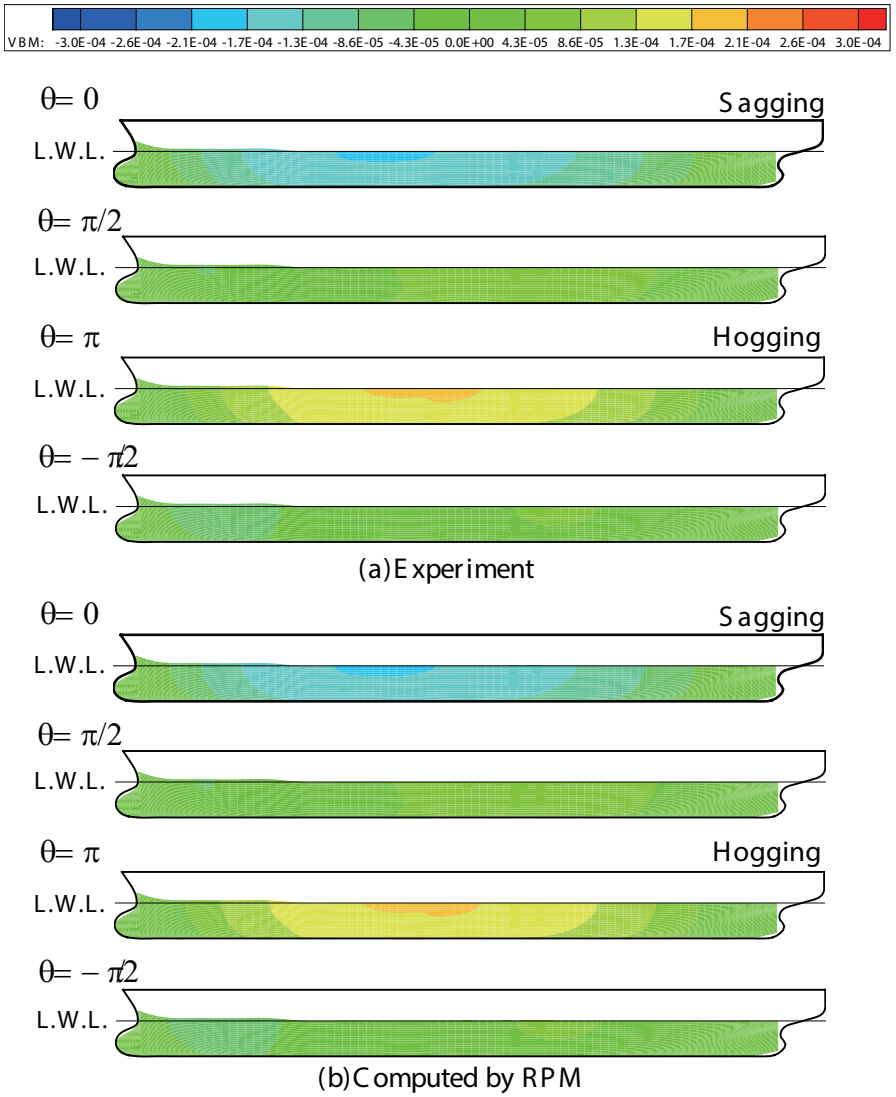

FIGURE C.5: VBM distribution at $\lambda/L = 2.00$ of head wave and $Fn = 0.00$; (a) Experiment, (b) Computation by RPM

C.2 Forward-speed in head wave

As an important part, a side view of the spatial distribution of VBM is depicted in Fig. C.6 - C.10 for the cases of $\lambda/L = 0.8 - 2.0$ in head wave and $Fn = 0.18$. In the same fashion from the comparison of unsteady pressure distribution, the experiment and computed results by CFD are compared and as expected overall good agreement and the reasonable result is obtained despite some discrepancies which might be caused by the ship motions. As obvious from the figures the magnitude of the VBM is small at $\lambda/L = 0.8$ and $\lambda/L = 1.0$ after that escalates significantly at resonant frequency $\lambda/L = 1.25$ and then attenuates over $\lambda/L = 1.5$. As we might notice the maximum VBM at sagging and hogging depicts a prominent nonlinearity in particular asymmetrical property between sagging and hogging and slightly shifted forward from the corresponding position observed at the zero-speed case.

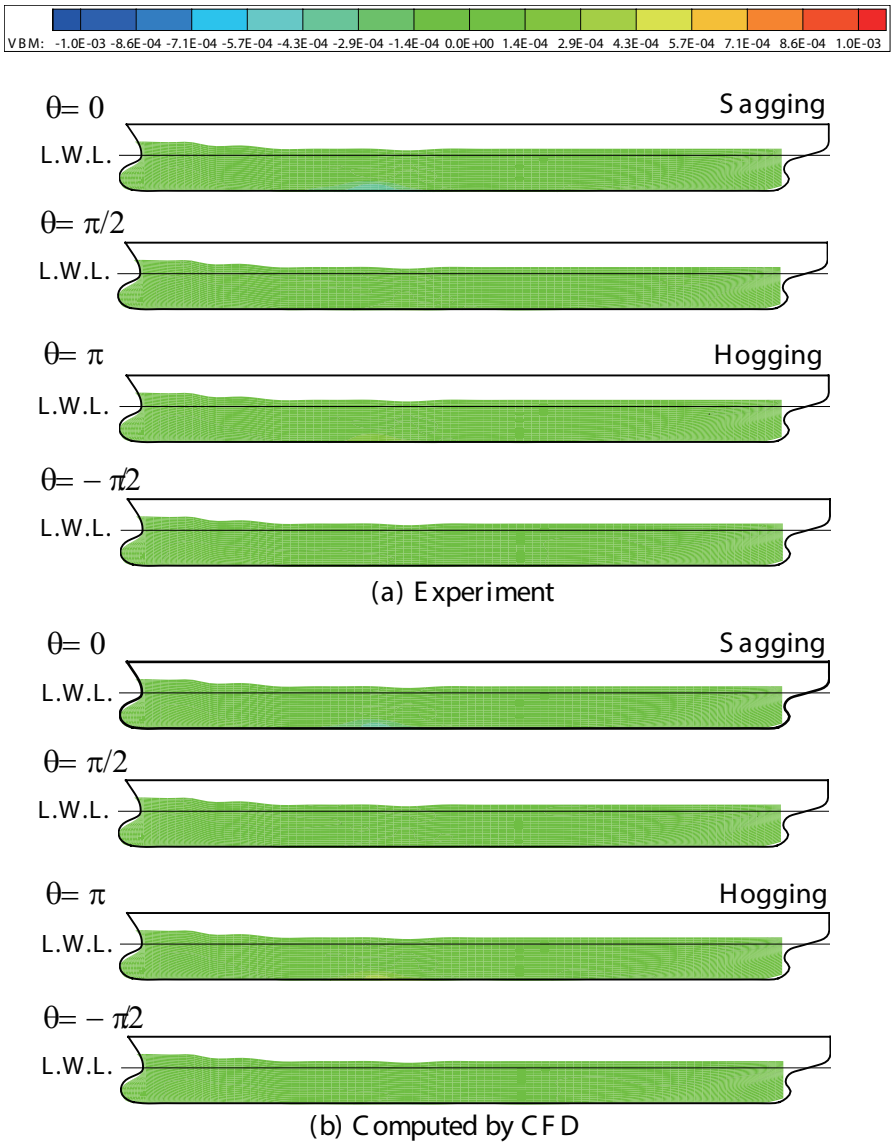

FIGURE C.6: VBM distribution at $\lambda/L = 0.80$ of head wave and $Fn = 0.18$; (a) Experiment, (b) Computation by CFD

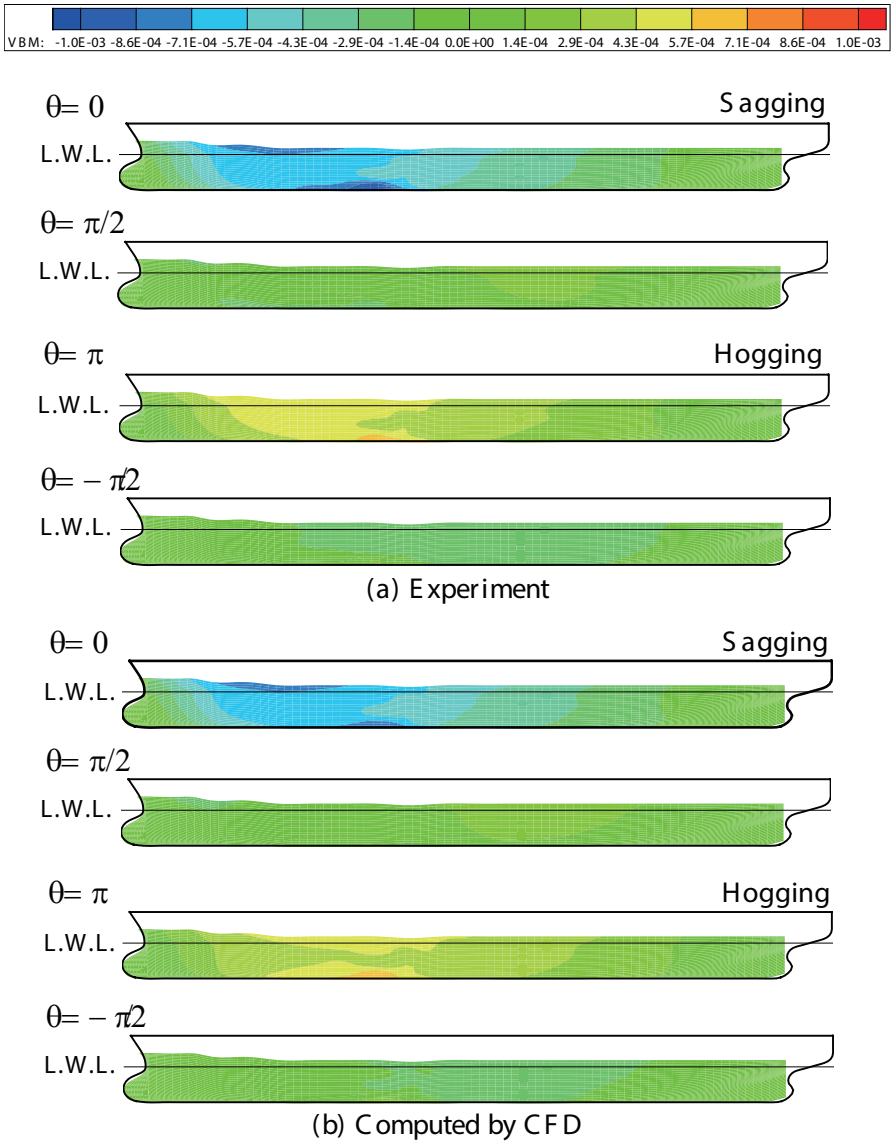

FIGURE C.7: VBM distribution at $\lambda/L = 1.00$ of head wave and $Fn = 0.18$; (a) Experiment, (b) Computation by CFD

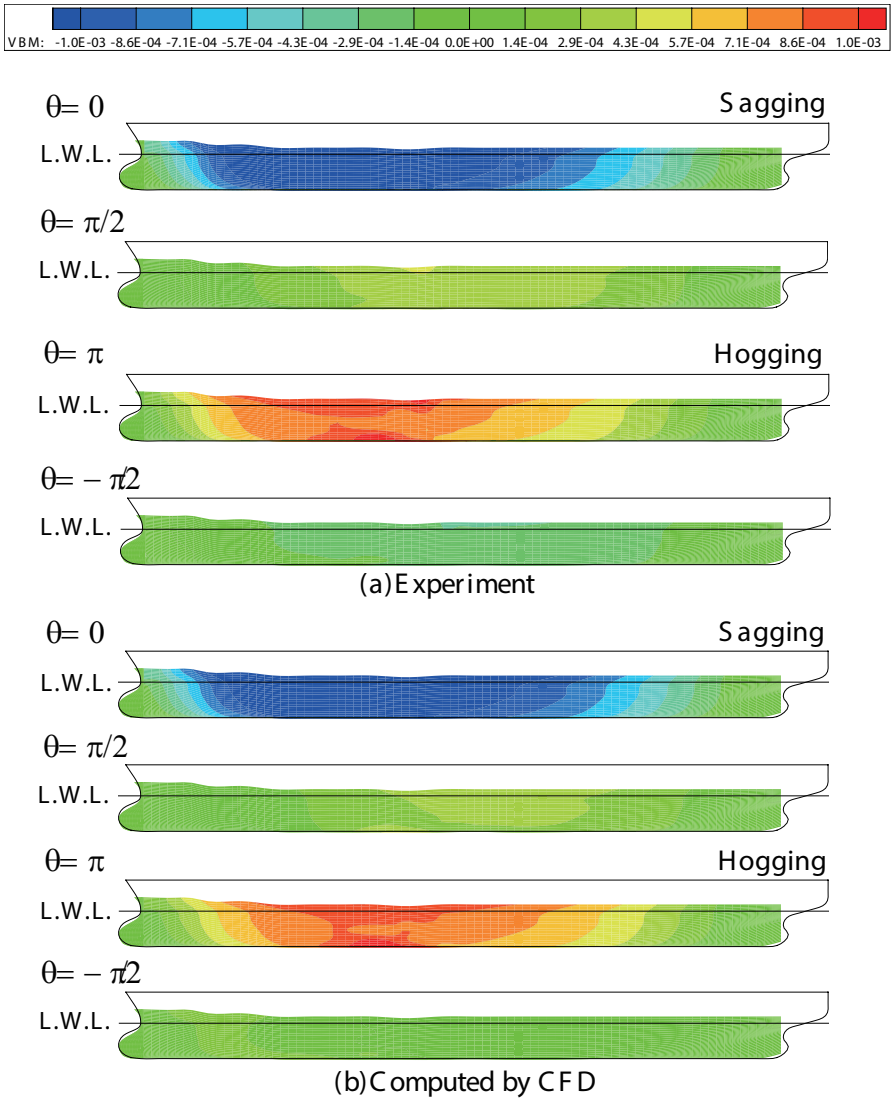

FIGURE C.8: VBM distribution at $\lambda/L = 1.25$ of head wave and $Fn = 0.18$; (a) Experiment, (b) Computation by CFD

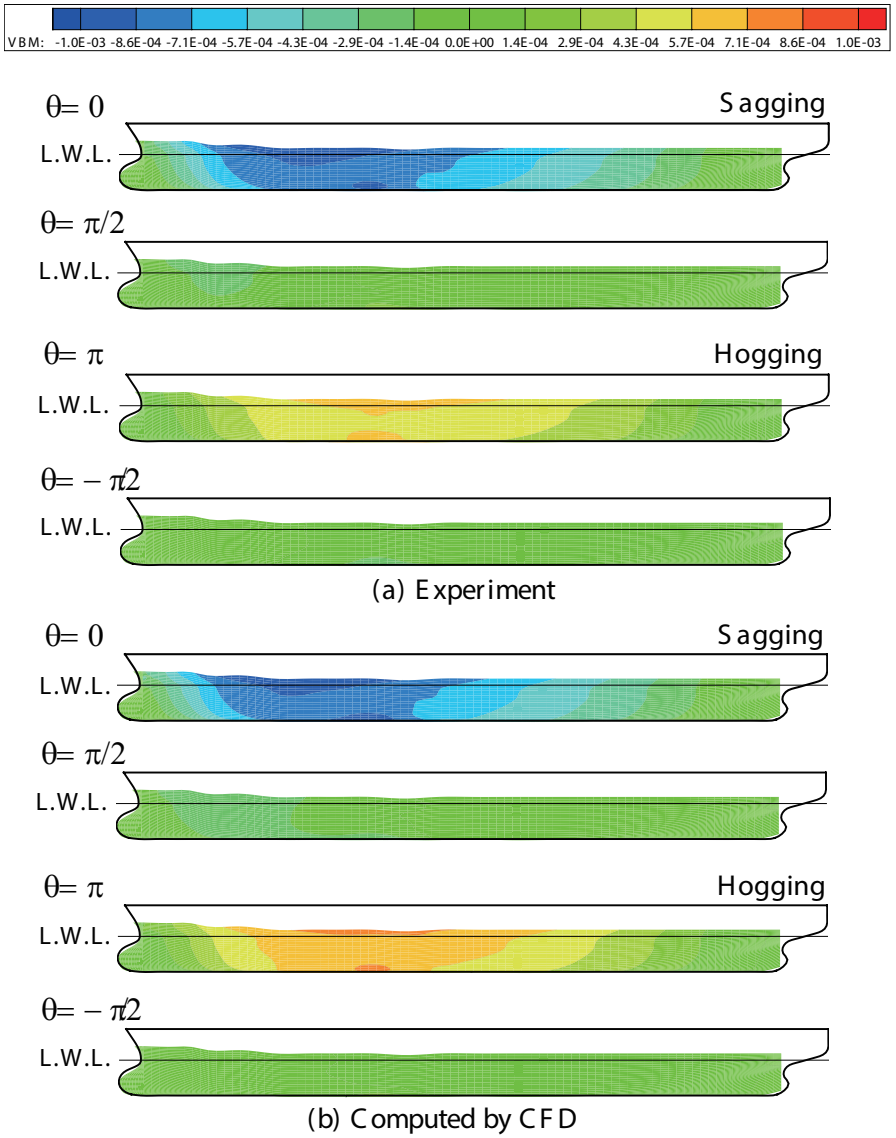

FIGURE C.9: VBM distribution at $\lambda/L = 1.50$ of head wave and $Fn = 0.18$; (a) Experiment, (b) Computation by CFD

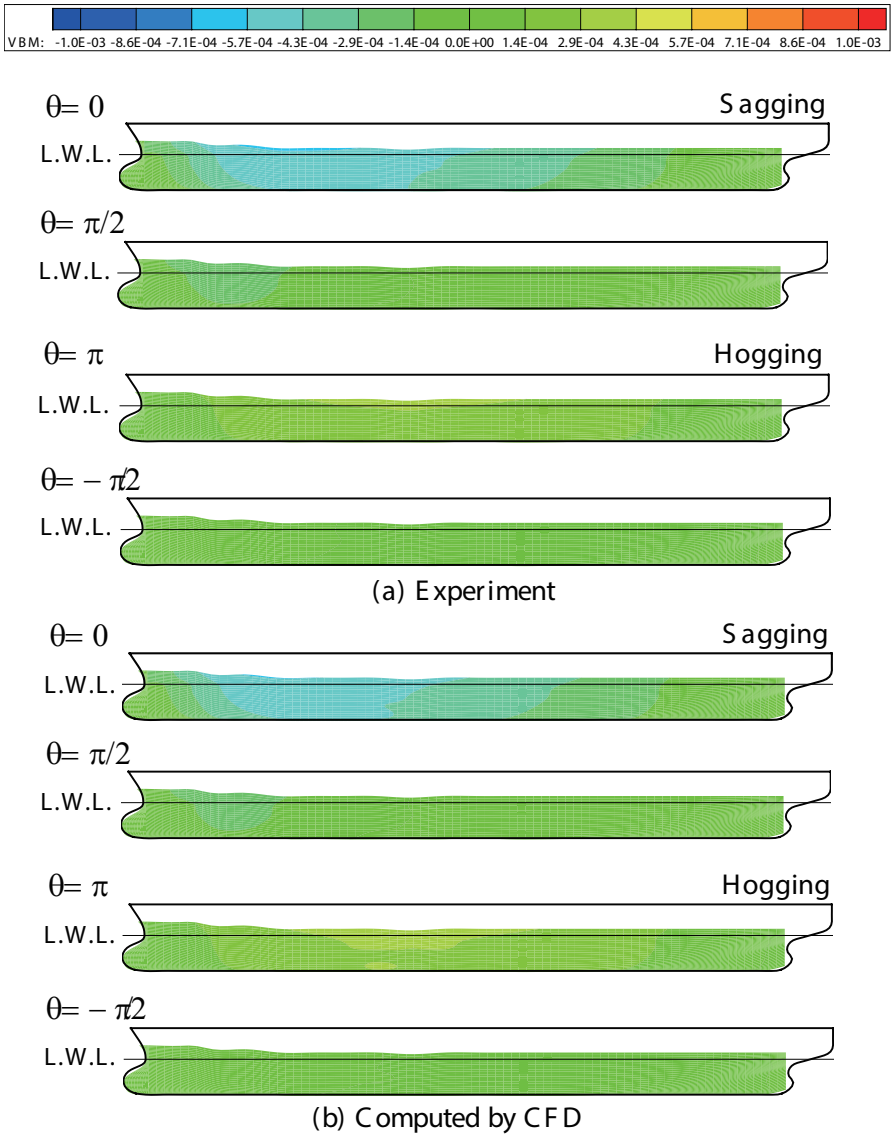

FIGURE C.10: VBM distribution at $\lambda/L = 2.00$ of head wave and $Fn = 0.18$; (a) Experiment, (b) Computation by CFD

Bibliographies

[1] M. Kashiwagi, H. Iwashita, S. Miura, and M. Hinatsu. Study on added resistance with measured unsteady pressure distribution on ship-hull surface. *Proceedings of the 34th IWWWFB (Newcastle, Australia)*, pages 81–84, 2019.

[2] NUMECA. Theoretical manual fine/marine. *https://www.numeca.com/product/finemarine*.

[3] R.E.D. Bishop, W.G. Price, and Y. Wu. A general linear hydroelasticity theory of floating structures moving in a seaway. *Philosophical Transactions of the Royal Society of London, Series A, Mathematical and Physical Sciences*, 316:375–426, 1986.

[4] I. Senjanović, Š. Malenica, and S. Tomašević. Hydroelasticity of large container ships. *Marine Structures*, 22(2):287–314, 2009.

[5] K.H. Kim and Y. Kim. Numerical analysis of springing and whipping using fully-coupled fsi models. *Ocean Engineering*, 91(15):28–50, 2014.

[6] M. Kashiwagi, S. Kuga, and S. Chimoto. Time- and frequency-domain calculation methods for ship hydroelasticity with forward speed,. *Proc. of Hydroelasticity in Marine Technology (Split, Croatia)*, 91(15):477–492, 2015.

[7] S.E. Hidaris, W. Bai, D. Dessi, A. Ergin, X. Gu, O.A. Hermundstad, R. Huijsmans, K. Iijima, U.D. Nielsen, J. Parunov, N. Fonseca, A. Papanikolaou, K. Argyriadis, and A.Incecik. Loads for use in the design of ships and offshore structures. *Ocean Engineering*, 78(1):131–174, 2014.

[8] P. Temarel, W. Bai, A. Bruns, Q. Derbanne, D. Dessi, S. Dhavalikar, N. Fonseca, T. Fukasawa, X. Gu, A. Nestegård, A. Papanikolaou, J. Parunov, K.H. Song, and S. Wang. Loads for use in the design of ships and offshore structures. *Ocean Engineering*, 119(1):274–308, 2016.

[9] ITTC. The seakeeping committee final report and recommendations. *Proceedings of the 27th ITTC*, 2017.

[10] B.J. Guo, S. Steen, and G.B. Deng. Seakeeping prediction of kvlcc2 in head waves with rans. *Applied Ocean Research*, 35:56–57, 2012.

[11] K. Niklas and H. Pruszko. Full scale cfd seakeeping simulations for case study ship redesigned from v-shaped bulbous bow to x-bow hull form. *Applied Ocean Research*, 89:188–201, 2019.

[12] C. Judge, M. Mousaviraad, F. Stern, E. Lee, A. Fullerton, J. Geiser, C. Schleicher, C. Merrill, C. Weil, J. Morin, M. Jiang, and C. Ikeda. Experiments and cfd of a high-speed deep-v planing hull part ii: Slamming in waves. *Applied Ocean Research*, 97:102059, 2020.

[13] J. Wang, W. Zhao, and D. C. Wan. Development of naoe-foam-sjtu solver based on openfoam for marine hydrodynamics. *Journal of Hydrodynamics*, 31(1):1–20, 2019.

[14] W. Xu, G. Filip, and K. J. Maki. A method for the prediction of extreme ship responses using design-event theory and computational fluid dynamics. *Journal of Ship Research*, 64(1):48–60, 2019.

[15] N. Toki, K. Hatakenaka, and T. Takahashi. Experimental and theoretical approach to the estimation of non-linear vertical wave loads. *Journal of the Society of Naval Architects of Japan*, 154:141–150, 1983.

[16] T. Kuroiwa and H. Ohtsubo. Nonlinearity of sagging moment of fine ships. *Journal of the Society of Naval Architects of Japan*, 161:234–241, 1987.

[17] M. Ueno and I. Watanabe. On asymmetry of vertical bending moment on ships. *Journal of the Society of Naval Architects of Japan*, 162:175–182, 1987.

[18] I. Watanabe and M. Ueno. Effects of bow flare shape to the wave loads of a container ship. *Journal of the Society of Naval Architects of Japan*, 166:259–266, 1989.

[19] I. Watanabe and C. Guedes Soares. Comparative study on the time-domain analysis of non-linear ship motions and loads. *Marine Structures*, 12:153–170, 1999.

[20] M.K. Wu and O.A. Hermundstad. Time-domain simulation of wave-induced nonlinear motions and loads and its applications in ship design. *Marine Structures*, 15:561–597, 2002.

[21] Y. Kim, K.H. Kim, J.H. Kim, T. Kim, M.G. Seo, and Y. Kim. Time-domain analysis of nonlinear motion responses and structural loads on ships and offshore structures: development of wish programs. *International Journal of Naval Architecture and Ocean Engineering*, 3(1):37–52, 2011.

[22] S.E. Hirdaris, Y. Lee, G. Mortola, A. Incecik, O. Turan, S.Y. Hong, B.W. Kim, K.H. Kim, S. Bennett, S.H. Miao, and P. Temarel. The influence of nonlinearities on the symmetric hydrodynamic response of a 10,000 teu container ship. *Ocean Engineering*, 111:166–178, 2016.

[23] Y. Jin, S. Chai, J. Duffy, C. Chin, and N. Bose. Urans predictions of wave induced loads and motions on ships in regular head and oblique waves at zero forward speed. *Journal of Fluids and Structures*, 74:178–204, 2017.

[24] P.A. Lakshmynarayanana and P. Temarel. Application of a two-way partitioned method for predicting the wave-induced loads of a flexible containership. *Applied Ocean Research*, 96:102052, 2020.

[25] J. Oberhagemann, O. el Moctar, and T. E. Schellin. Fluid-structure coupling to assess whipping effects on global loads of a large containership. *Proceedings of 27th Symposium on Naval Hydrodynamics, Seoul, Korea*, (8), 2008.

[26] J. Oberhagemann, M. Holtmann, O. el Moctar, T. E. Schellin, and D. Kim. Stern slamming of a lng carrier, journal of offshore mechanics and arctic engineering. *Journal of Offshore Mechanics and Arctic Engineering*, 131(3):031103, 2009.

[27] H. Orihara. Comparison of cfd simulations with experimental data for a tanker model advancing in waves. *International Journal of Naval Architecture and Ocean Engineering*, 3(1):1–8, 2011.

[28] S. K. Hänninen, T. Mikkola, and J. Matusiak. Comparison of cfd simulations with experimental data for a tanker model advancing in waves. *Journal of Marine Science and Technology*, 19:103–115, 2014.

[29] M.K. Wu and T. Moan. Efficient calculation of wave-induced ship responses considering structural dynamic effects. *Applied Ocean Research*, 27:81–96, 2005.

[30] S.P. Singh and D. Sen. A comparative study on 3d wave load and pressure computations for different level of modelling of nonlinearities. *Marine Structures*, 20:1–24, 2007.

[31] I. Drummen, M.K. Wu, and T. Moan. Experimental and numerical study of containership responses in severe head seas, marine structures. *Marine Structures*, 22:172–193, 2009.

[32] N. Fonseca, R. Pascoal, C. Guedes Soares, G. Clauss, and C. Schmittner. Numerical and experimental analysis of extreme wave induced vertical bending moments on a fpso. *Applied Ocean Research*, 32:374–390, 2010.

[33] G.F. Clauss and M. Klein. Experimental investigation on the vertical bending moment in extreme sea states for different hulls. *Ocean Engineering*, 119:178–204, 2016.

[34] S. Rajendran, N. Fonseca, and C. Guedes Soares. Prediction of extreme motions and vertical bending moments on a cruise ship and comparison with experimental data. *Ocean Engineering*, 127:368–386, 2016.

[35] G. Vasquez, N. Fonseca, and C. Guedes Soares. Experimental and numerical vertical bending moment of a bulk carrier and a roll-on/roll-off ship in extreme waves. *Ocean Engineering*, 124:404–418, 2016.

[36] S. Mizokami, H. Yasukawa, T. Kuroiwa, H. Sueoka, S. Nishimura, and S. Miyazaki. Wave load on a container ship in rough seas. *Journal of the Society of Naval Architects of Japan*, 189:181–192, 2001.

[37] R. Miyake, T. Zhu, and H. Kagemoto. On the estimation of wave-induced loads acting on practical merchant ships by a rankine source method. *Journal of the Society of Naval Architects of Japan*, 190:107–119, 2001.

[38] M. Wakahara, A. Tanigami, S. Shingo, M. Nakajima, T. Fukasawa, and K. Kanai. Development of an affix-type multipoint pressure sensor by use of fbg - 2nd report: Multipoint pressure measurements on the surface of model ship in resistance test (in japanese). *Journal of the Japan Society of Naval Architects*, 7:9–14, 2008.

[39] H. Iwashita and M. Kashiwagi. An innovative efd for studying ship seakeeping. *Proceedings of the 33rd IWWWFB (Guidel-Plages, France)*, pages 85–88, 2018.

[40] H. Iwashita, M. Kashiwagi, Y. Ito, Y. Seki, J. Yoshida, and M. Wakahara. Measurement of unsteady pressure distributions of a ship advancing in waves (in japanese). *Conf Proc of the Japan Soci of Naval Archi and Ocean Eng*, 22:235–238, 2016.

[41] M. Kashiwagi, H. Iwashita, Y. Seki, S. Yoshida, Y. Ito, A. Katano, H. Ohnishi, and M. Wakahara. Measurement of unsteady pressure distributions of a ship advancing in waves (in japanese). *Conf Proc of the Japan Soci of Naval Archi and Ocean Eng*, 24:613–616, 2017.

[42] H. Ohnishi, H. Iwashita, M. Kashiwagi, T. Hara, Y. Ito, and M. Wakahara. An innovative efd for ship seakeeping. *Proc of Workshop on Environmental Technologies in Naval Archi and Ocean Eng, Hiroshima*, pages 97–101, 2017.

[43] H. Iwashita, M. Kashiwagi, Y. Ito, Y. Seki, J. Yoshida, and M. Wakahara. Calculation of ship seakeeping in low speed / low-frequency range by frequency-domain rankine panel methods (in japanese). *Conf Proc of the Japan Soci of Naval Archi and Ocean Eng*, 24:129–146, 2017.

[44] Y. Kim and J.H. Kim. Benchmark study on motions and loads of a 6750-teu containership. *Ocean Engineering*, 119:262–273, 2016.

[45] M. Kashiwagi E. Yasuda, H. Iwashita. Improvement of rankine panel method for seakeeping prediction of a ship in low frequency region. *Proceedings of the 35th International Conference on Ocean, Offshore and Arctic Engineering (Busan, Korea)*, pages OMAE2016–54163, 2016.

[46] Y. Seki, M. Kashiwagi, and H. Iwashita. Experimental study on added resistance and unsteady pressure distribution in following waves. *Proceedings of the 13th Practical Design of Ships and Other Floating Structures, Copenhagen*, ID-147, 2016.

[47] D. Nakos P.D. Sclavounos. Ship motion by a three dimensional rankine panel method. *Proceedings of the 18th Symposium on Naval Hydrodynamics, National Academy Press, Washington, DC*, pages 21–40, 1990.

[48] M. Kashiwagi, S. Mizokami, H. Yasukawa, and Y. Fukushima. Prediction of wave loads on actual ships by the enhanced unified theory. *Proceedings of the 23rd International Symposium on Naval Hydrodynamics, France*, pages 95–109, 2000.

[49] J.N. Newman. Distributions of sources and normal dipoles over a quadrilateral panel. *Journal of Enginering Mathematics*, 20:113–126, 1986.

[50] P. Queutey and M. Visonneau. An interface capturing method for free-surface hydrodynamic flows. *Comput. Fluids*, 36(9):1481–1510, 2007.

[51] J. Wackers, B. Koren, H. C. Raven, A. van der Ploeg, A. R. Starke, G. B. Deng, P. Queutey, M. Visonneau, T. Hino, and K. Ohashi. Free-surface viscous flow solution methods for ship hydrodynamics. *Archives of Computational Methods in Engineering*, 18:1–41, 2011.

[52] F.R.Menter. Two-equation eddy-viscosity turbulence models for engineering applications. *AIAA J.*, 32(8):1598–1605, 1994.

[53] F.R.Menter, M. Kuntz, and R. Langtry. Ten years of industrial experience with the sst turbulence model. *Turbul. Heat. Mass Transf.*, 4(4):625–632, 2003.

[54] ITTC. Practical guidelines for ship cfd applications. *ITTC - Recommended Procedures and Guidelines*, 2011.